MECHANICS OF ATHEROSCLEROSIS, HYPERTENSION INDUCED GROWTH, AND ARTERIAL REMODELING

A Dissertation

by

HEATHER NAOMI HAYENGA

Submitted to the Office of Graduate Studies of
Texas A&M University
in partial fulfillment of the requirements for the degree of

DOCTOR OF PHILOSOPHY

May 2011

Major Subject: Biomedical Engineering

Mechanics of Atherosclerosis, Hypertension Induced Growth, and Arterial Remodeling

MECHANICS OF ATHEROSCLEROSIS, HYPERTENSION INDUCED GROWTH, AND ARTERIAL REMODELING

A Dissertation

by

HEATHER NAOMI HAYENGA

Submitted to the Office of Graduate Studies of
Texas A&M University
in partial fulfillment of the requirements for the degree of

DOCTOR OF PHILOSOPHY

Approved by:

Chair of Committee,	James E. Moore, Jr.
Committee Members,	Fred J. Clubb
	Roland R. Kaunas
	Alvin T. Yeh
Head of Department,	Gerald L. Cote

May 2011

Major Subject: Biomedical Engineering

ABSTRACT

Mechanics of Atherosclerosis, Hypertension Induced Growth,
and Arterial Remodeling. (December 2010)
Heather Naomi Hayenga, B.S., University of California, Davis
Chair of Advisory Committee: Dr. James E. Moore, Jr.

In order to create informed predictive models that capture artery dependent responses during atherosclerosis progression and the long term response to hypertension, one needs to know the structural, biochemical and mechanical properties as a function of time in these diseased states. In the case of hypertension more is known about the mechanical changes; while, less is known about the structural changes over time. For atherosclerotic plaques, more is known about the structure and less about the mechanical properties. We established a congruent multi-scale model to predict the adapted salient arterial geometry, structure and biochemical response to an increase in pressure. Geometrical and structural responses to hypertension were then quantified in a hypertensive animal model. Eventually this type of model may be used to predict mechanical changes in complex disease such as atherosclerosis. Thus for future verification and implementation we experimentally tested atherosclerotic plaques and quantified composition, structure and mechanical properties.

Using the theoretical models we can now predict arterial changes in biochemical concentrations as well as salient features such as geometry, mass of elastin, smooth

muscle, and collagen, and circumferential stress, in response to hemodynamic loads. Using an aortic coarctation model of hypertension, we found structural arterial responses differ in the aorta, coronary and cerebral arteries. Effects of elevated pressure manifest first in the central arteries and later in distal muscular arteries. In the aorta, there is a loss and then increase of cytoskeleton actin fibers, production of fibrillar collagen and elastin, hyperplasia or hypertrophy with nuclear polypoid, and recruitment of hemopoeitic progenitor cells and monocytes. In the muscular coronary, we see similar changes albeit it appears actin fibers are recruited and collagen production is only increased slightly in order to maintain constant the overall ratio of ~55%. In the muscular cerebral artery, despite a temporary loss in actin fibers there is little structural change. Contrary to hypertensive arteries, characterizing regional stiffness in atherosclerotic plaques has not been done before. Therefore, experimental testing on atherosclerotic plaques of ApoE-/- mice was performed and revealed nearly homogenously lipidic plaques with a median axial compressive stiffness value of 1.5 kPa.

DEDICATION

To my patient and loving father, Calvin Godfrey Hayenga III

ACKNOWLEDGMENTS

The research presented here would not have been possible without the love, support, and guidance from others. Nothing but sincere gratitude goes to my true mentor, Dr. Jay Humphrey. His motivation, passion, intellect, understanding and faith is far beyond what I had imagined possible. I also acknowledge committee members, Dr. James Moore Jr., Dr. Fred Clubb, Dr. Roland Kaunas, and Dr. Alvin Yeh who have selflessly offered me guidance, resources, time and instruction. I convey my gratitude to collaborators, Dr. Jerome Trzeciakowski, Dr. Andreea Trache, Dr. Kevin Costa, Dr. Shayn Peirce and Bryan Thorne for their amazing expertise and willingness to share for the betterment of science.

I hold dear to my heart the colleagues with whom I have worked alongside for the past 5 years. First and foremost I thank my Italian friends, Luca Cardamone and Jacopo Ferruzzi. Although individually unique, it was always a pleasure being around them, whether discussing vascular mechanics, faith, running or traveling. Special thanks go to the undergraduates Brooke Hallmark and Cody Sanderson for their hard work and efficiency in sample preparation, imaging, and analysis; without them this work would have taken at least another year to complete. I appreciate the rest of my lab mates, Hallie Wagner, Melissa Collins, Marie Enevoldsen, Chiara Bellini, Ingrid Masson, John Eberth, Bethany Anderson, John Wilson, David Simon, Ryan Pedrigi, and Art Valentin, who have positively influenced my research and perspective on biomechanics. Above

all, my sweetest thoughts go to Clark Meyer, who has been an abundant source of knowledge, encouragement and help.

There are not enough words to thank my family, Peggy Gregory, Kim Hayenga, and Cal Hayenga, for being so proud of me and making me feel loved even when we are separated by 1,500 miles. I also acknowledge my honorary sister, Thaidra Gaufin, who has been a source of motivation and guidance throughout my life. They have brought much enjoyment to my life over these years. The bond we share is unique and strong. Without their unflinching support I would not have had this opportunity.

NOMENCLATURE

AFM	Atomic Force Microscopy
ApoE-/-	Apolipoprotein E Knockout
H&E	Hematoxylin and Eosin
HT	Hypertensive
LAD	Left Anterior Descending Coronary Artery
MCA	Middle Cerebral Artery
NT	Normotensive
P-Ao	Proximal Aorta
PSR	Picosirius Red
SMA	Smooth Muscle Actin
SMC	Smooth Muscle Cell
TRI	Masson's Trichrome
VVG	Verhoeff-Van Gieson
vWF	Von Willebrand Factor

TABLE OF CONTENTS

LIST OF FIGURES

FIGURE Page

FIGURE Page

FIGURE Page

LIST OF TABLES

CHAPTER I

INTRODUCTION

Arterial cells sense both their mechanical and chemical environments, and they respond in ways that are essential for developing, maintaining, or adapting many aspects of tissue structure and function [1-4]. In order to create informed predictive models that capture and eventually predict arterial responses during hypertension and the progression of diseases such as atherosclerosis, one must understand the underlying structure and mechanical properties, and how they may change as a function of time. This motivated, in part, the need to build a predictive model of arterial growth and remodeling in response to hypertension based on data in the literature. Developing predictive models of arterial growth and remodeling revealed a need for additional data, particularly on the time course of structural arterial remodeling. Motivated by this need, arteries from a porcine model of hypertension were examined histologically over a growth and remodeling time course of 8 weeks. Significant intimal thickening was observed in the aorta and coronary arteries, but not cerebral arteries. Motivated by an interest in the mechanical properties of intimal lesions, particularly atherosclerotic plaques, and provoked by a lack of direct characterization of regional plaque properties, plaques from the aorta of mice were tested mechanically and characterized histologically. The overall goal of this work, therefore, is to begin to fill the gaps in our understanding of the mechanobiology of hypertension, an important risk factor for many cardiovascular

---

This dissertation follows the style of Atherosclerosis.

diseases, and in the mechanics of atherosclerosis, an underlying cause of diverse organ damage.

Chapter II serves as an overview of biochemical and biomechanical vascular events involved in vascular remodeling due to hypertension and atherosclerosis - in particular, cell mechanics and resulting responses. The porcine coarctation and mouse apolipoprotein E knock out (ApoE -/-) animal models used herein are also described.

In Chapter III, we propose a new theoretical approach for incorporating cell level information within a tissue level model to predict mechanical and chemical responses by arteries. Chapter IV takes the model a step further to predict general mechanobiological responses in hypertension.

In Chapter V, we characterize pressure-induced structural changes over an 8 week period through quantification of arterial geometry and cellular composition in the proximal aorta, left anterior descending artery, and middle cerebral artery from a porcine aortic coarctation induced model of hypertension. These results are compared to our multiscale modeling based predictions of the salient changes of arteries in response to hypertension.

In Chapter VI, regional mechanical properties of advanced plaques from an ApoE-/- mouse model are characterized using atomic force microscopy (AFM). Understanding the mechanics of and factors involved in structural properties of lesions could lead to strategies to stabilize atherosclerotic plaques and to prevent plaque rupture through lesion-specific interventions.

Lastly, Chapter VII summarizes the major contributions of this work.

CHAPTER II

BACKGROUND AND SIGNIFICANCE: VASCULAR REMODELING

The main conduits for blood flow include arteries, arterioles, capillaries, venules, and veins. Although the primary function of an artery is to carry blood away from the heart, the microstructure of the arterial wall can vary significantly according to location within the arterial tree as well as with local hemodynamics, age, and disease. Nonetheless, arteries are roughly categorized as elastic or muscular. The elastic arteries tend to have more elastin, a larger diameter, and be located closer to the heart. Regardless of type, all arteries consist of 3 layers: an intima, media and adventitia [**Fig. 2.1**].

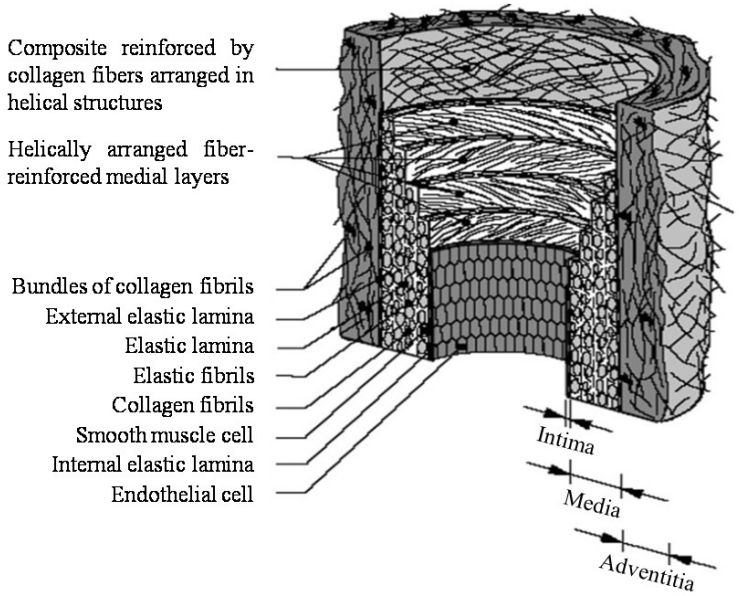

FIGURE 2.1. Schematic of an elastic artery showing the 3 layers, and detailing the major constituents and their general orientation in each layer [5].

The intima typically consists of a monolayer of endothelial cells residing on a thin basal lamina (about 80 nanometers). The endothelial cells are characteristically oriented in the direction of flow (axially). The basal lamina is a net-like mesh consisting primarily of collagen IV, laminin, fibronectin, and proteoglycans. Connected to the basal lamina is the internal elastic lamina (IEL). The IEL is a fenestrated sheet of elastin (pore size about 2 to 7 micrometers) that allows transmural passage of water, nutrients, and electrolytes.

The media is primarily comprised of collagen (types I, III, and V), elastin, smooth muscle cells, and a ground substance matrix. The distribution and amounts of these constituents vary depending on the type of artery and obviously, species. For example, elastic arteries such as the human aorta may have up to 70 concentric layers of smooth muscle (each about 5 to 15 micrometers thick) separated by fenestrated sheets of elastic lamina (each about 3 micrometers thick). Muscular arteries, in contrast, tend to have only an internal elastic lamina and an external elastic lamina; cerebral arteries are an exception for they only have an IEL. Previous studies suggest that the number of lamellar units (i.e. elastic lamina and adjacent SMC layer) in elastic arteries is proportional to the tensile forces within the wall [6-8]. Contraction of SMCs in the media endows the wall with a vascular tone, which affects both stiffness and caliber. The interconnected collagen and smooth muscle cells are often oriented at a slight helical pitch from the circumferential direction. Biomechanically, this preferred orientation allows the contraction of the smooth muscle cells to better regulate the diameter and flow, especially in small muscular arteries. The elastin allows the vessel to recoil

elastically after each pressure pulse, and the collagenous helix allows the vessel to resist loads in the longitudinal and circumferential directions.

The outermost layer, or adventitia, is comprised primarily of fibroblasts, vasa vasorum, admixed elastin, collagen type I, and nerve bundles. Unlike the media, these collagen fibers tend to be oriented in the axial direction and to be slightly undulated. The adventitia makes up about 50% of the wall in muscular arteries and about 10% of the wall in elastic arteries. Due to the diffusion limit of nutrients and oxygen, the vasa vasorum serves as a means to get these elements to the outer portion of larger arteries.

It is well accepted that an increase of internal pressure during hypertension leads to wall thickening [**Fig. 2.2 (A, B)**], which in turn restores the increased circumferential stress toward normal [9]; what remains a bit unclear is from where does the accumulated mass originate. The original hypothesis, which is still held by some today, was that medial hyperplasia of vascular smooth muscle constitutes the increase in wall thickness [10-12]. Since then, through transplant vasculopathy, several researchers have reported a host bone marrow cell origin of neointimal SMCs [13]. *In vitro* studies have also shown endothelial cells (ECs), when cultured with transforming growth factor beta (TGF-β), transdiffereniate into a SMC like phenotype expressing α-actin and lose the EC factor VIII antigen expression [14, 15]. Still others have found leukocytes present in the adventitia of hypertensive models [16]. These more recent findings have reformed our thinking of wall thickening due to hypertension. Yet there is much to be resolved regarding to what degree local and circulating cells contribute to neo-intimal as well as overall wall thickening over time as hypertension progresses.

On the other hand plaque development has been well classified. Genesis typically starts with a fatty streak of foam cells. Some fatty streaks continue to accumulate lipid, smooth muscles cells (SMC), connective tissue and extracellular matrix proteins, growing into raised lesions [**Fig. 2.2 (C, D)**].

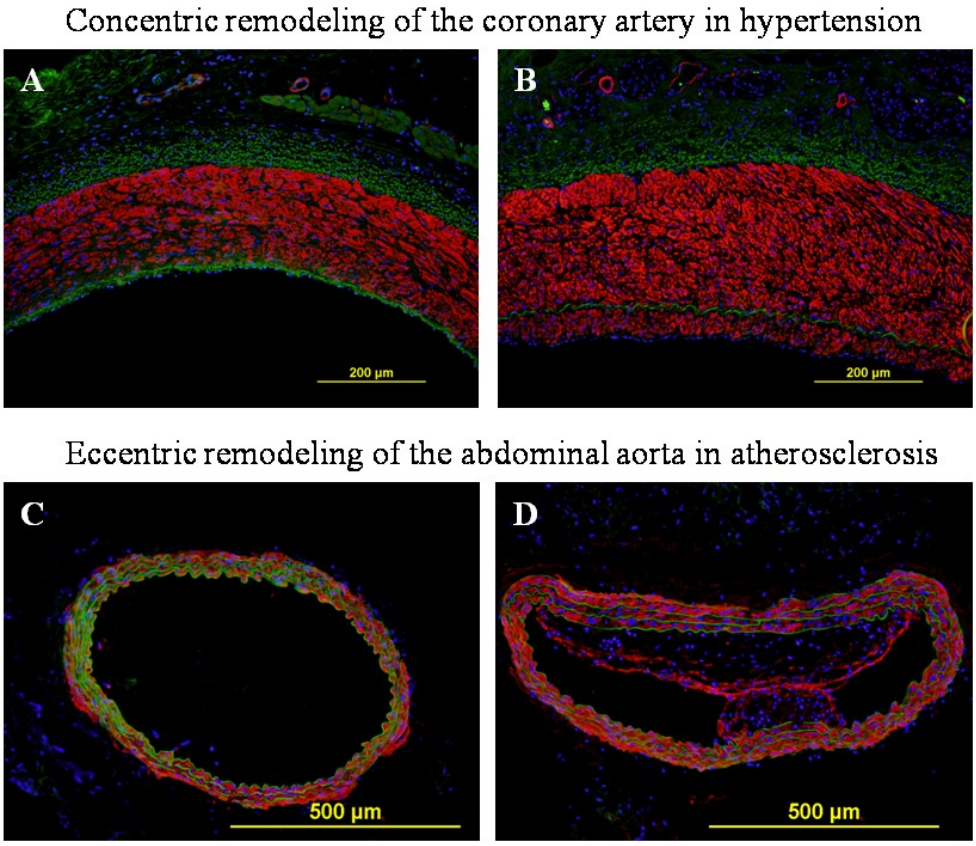

FIGURE 2.2. (**A, B**) Pig coronary and (**C, D**) mouse abdominal aorta undergo significant structural changes from (**A, C**) normal to (**B, D**) perturbed states in response to their mechanobiological environment. (**B**) In a coarction model of hypertension a neointima forms that is nearly uniform in radial thickness neointima forms. (**D**) In an ApoE-/- model of atherosclerosis eccentric atheromas form. Red indicates smooth mucle actin, blue indicates nuclei, and green indicates elastin.

Animal Models

Aortic Coarctation. An experimental method to stimulate hypertension is to place a balloon-expandable occluder around the thoracic aorta and inflate it until the mean arterial pressure is above 150 mmHg. In this model, 30 days after the target pressure is reached, the renin and aldosterone levels are not significantly different from the preocclusion levels [17]. This experimental model is similar to a congenital heart defect called "Coarctation of the Aorta" (CoA). CoA is most likely caused by eccentric hyperplasia during ductus arteriosus closure and affects roughly 1 out of every 10,000 people [18]. The aorta may be constricted locally or, more commonly, a long segment of the aorta is narrowed. If untreated, CoA has a poor prognosis with 25% mortality by age 20 years, 50% by age 35 years, 75% by age 46 years, and 90% by age 50 years [19, 20]. Studies show that patients with CoA have hypertension [20] along with a 5-fold increase in the likelihood of intracranial aneurysm [18], left ventricle hypertrophy [21], and aortic aneurysms. Deaths are primarily due to intracranial hemorrhage, coronary artery disease, congestive heart failure, or ruptured aortic aneurysms [22]. It has been established that aortic stenosis due to coarctation causes adverse reactions in the arterial system, but the exact mechanisms controlling spatial and temporal development of the stenosis are still unknown.

ApoE Knockout Mice. One of the most widely used animal models for studying atherosclerosis is the genetically engineered homozygous Apolipoprotein E-deficient (ApoE-/-) mouse (Jackson Laboratories, Maine, USA). These mice have a higher than normal concentration of LDL in their blood (~400 mg/dL vs 85 mg/dL). Therefore, more LDL is available to diffuse into and remain within the vessel wall, especially in areas of flow recirculation. In addition, more LDL increases blood viscosity, which contributes to a prolonged exposure of the endothelium to atherogenic particles [23]. Thus these mice accelerate the atherosclerotic process, with reported advanced eccentric lesions consisting of large necrotic cores, abundant fibrous tissue, lipid-laden foam cells, smooth muscle cells, calcification, and cholesterol clefts in the abdominal aorta at 30 weeks [24, 25]. Many studies have shown that the atherosclerotic lesions in ApoE-/- mice histologically and pathologically resemble all known stages of atherosclerosis found in humans [24-26]. Moreover, the aortic pulse wave velocity is higher in the ApoE-/- compared to the wild type, which is indicative of aortic stiffening, which has been observed in humans with atherosclerosis [27].

CHAPTER III

THEORETICAL FRAMEWORK

Overview

Initial observations of vascular diseases in the clinical setting are made primarily at the tissue level [28]. For example, using noninvasive medical imaging, clinicians can detect local changes in luminal diameter or wall thickness. The artery may be thickened due to hypertension, stenosed due to an atherosclerotic plaque, or dilated due to an aneurysm. Combining luminal diameter with information on local pressure (e.g., via tonometry or invasive transducers) can allow one to infer the degree of arterial stiffening due to hypertension or aging. Nevertheless, increased detail on the arterial behavior, based on information on geometry and applied loads, requires knowledge of the associated constitutive relations. These constitutive relations can be formulated to yield mechanically motivated (e.g., stress-strain) and/or biologically motivated (e.g., dose response) relationships. Toward this end, we submit that combining a tissue-level constrained mixture model (CMM) with a cell-level agent based model (ABM) represents one possible step toward the ultimate goal of multi-scale modeling of the vasculature wherein manifestations of disease at a clinical level can be understood in terms of underlying mechanisms at the cell biological level. Moreover, by ensuring congruency between these two otherwise disparate types of models, each motivated differently by and built upon different types of data, can help increase the robustness of our modeling. Herein, therefore, we review a particular CMM and ABM, the data upon

which they are based, and how one can increase confidence in their use in multi-scale modeling by comparing common metrics between two exclusive models.

Introduction

Continuum biomechanics is well suited for relating measurable blood pressures and flows to the stresses and strains within the arterial wall in a way that often correlates well with pathogenesis and disease progression, but it not well-suited for describing the underlying molecular and cellular level mechanobiological and biochemical responses. We thus suggest a new method to integrate a continuum based constrained mixture model (CMM) for the tissue level and an agent based model (ABM) for the cellular level, and we introduce a new paradigm for multi-scale modeling that can enable a new iterative level of model verification. Briefly, application of the continuum based mixture models to growth mechanics are typically founded on in vivo or in vitro data from intact vessels wherein information relating to individual cells or proteins is averaged over representative volumes, hence yielding lumped parameter type models; in contrast, application of algorithmic agent based models is typically founded on in vitro data from cell cultures or isolated cells wherein responses resulting from natural in vivo cell-cell or cell-matrix interactions are lost, hence yielding well defined results with less physiologic meaning. Although these models typically focus on different types of quantities and responses, they can and should have some areas of overlap. We suggest that such overlaps should be exploited – that is, by ensuring congruency between models formulated for different spatial and temporal scales, based on inherently different types of data, each model may in turn be expected to more faithfully reflect salient behaviors

of the actual biological system and together offer more reliable predictive capability. Herein, we illustrate predictions by both the CMM and ABM under homeostatic conditions. Keeping in mind the models were designed for future implementation under altered hemodynamics wherein congruency checks are commended. Therefore, in Chapter IV we illustrate the divergent response of both models under hypertensive conditions and introduce a novel congruency check in model verification.

Studies initiated in the 1970s and 1980s revealed that individual vascular cells are highly responsive to changes in their mechanical environment, thus giving rise to the field of vascular mechanobiology. For example, Leung et al. (1976)[29] showed that increased cyclic stretch (or stress) caused vascular smooth muscle cells to increase their production of collagen and proteoglycans. This finding is consistent with the increased deposition of extracellular matrix in the thickened aortic wall in hypertension, and in hindsight, consistent with current thinking that increased pulse pressure (i.e., associated cyclic stress or strain) correlates well with changes manifested by the arterial wall (see [30, 31]). Similar studies on endothelial cells revealed that they change their production of diverse molecules (e.g., vasoactive, mitogenic, proteolytic, inflammatory) in response to changes in wall shear stress (see [32, 33]). Again, changes differed in some cases between steady and pulsatile stimuli (see [34, 35]), thus suggesting the importance of the latter. See Humphrey (2008) [36] for a review of diverse data that collectively suggest the existence of a cell-mediated mechanical homeostasis across multiple length and time scales in the vasculature.

Whereas early “kinematic growth” models described consequences of arterial adaptations, Humphrey and Rajagopal (2003) [37] suggested that there was a need for a theoretical framework motivated by the mechanisms by which cells actually grow and remodel a tissue in response to altered mechanical loads. Toward that end, they introduced the concept of a constrained mixture wherein the equations of continuum biomechanics are augmented by three classes of constitutive relations that together account for the production and removal at different rates of individual structurally significant constituents, which in turn can have separate natural (stress-free) configurations and material properties. Implementations of this basic theory of growth and remodeling (G&R) have predicted salient characteristics of diverse arterial adaptations [38-42]. Nevertheless, all prior implementations of this approach employ “lumped parameter” models of production and removal.

Recalling the observations of Leung et al. (1976) [29], that increased cyclic stretch of vascular smooth muscle cells increases their production of collagen, Li et al. (1998) [43] extended this study to show that such production could be blocked via an antagonist to angiotensin II (ANG-II), an inhibitor of the angiotensin I convertor enzyme (ACE), or both, which in turn resulted in a decreased production of transforming growth factor (TGF-β1) that either directly or via connective tissue growth factor (CTGF) altered the production of collagen. In other words, complex mechano-chemo-biological responses at the molecular level govern cell-mediated adaptations at tissue levels. Increasingly sophisticated models should thus be able to include such biological complexity at multiple scales.

Agent based models enable one to study complex, coupled mechano-chemo-biological responses at the cell level. Such models have been used, for example, to simulate a variety of adaptive responses in the vasculature, including angiogenesis in response to exogenously applied growth factors [44], tumor angiogenesis [45], and vasculogenesis [46]. All of these models represent single cells as individual "agents" that can exhibit realistic biological behaviors, such as proliferation, migration, differentiation, and apoptosis, according to a set of rules that are derived directly from data. Space and time are treated discretely, and emergent tissue-level responses can arise from collective interactions of hundreds or thousands of agents with one another and with their environment. The power of an ABM thus lies in its ability to represent individual biological cells as well as heterogeneous cell-cell interactions and its ability to model biologically-relevant stochasticity.

In summary, CMMs and ABMs represent different, but complementary, approaches to modeling the complexity of cell-mediated, tissue-level adaptations. We establish herein these models in a way that capitalizes on their individual strengths and compensates for their individual weaknesses, which depend in part on the data sets upon which they are formulated. Because information at one scale can inform the other (and vice versa), our models were designed in such a way to eventually be able to refine model parameters by ensuring congruency between models while integrating multiscale phenomena.

Methods

Our overall goal is to pursue a natural progression of mathematical modeling of arterial adaptations from tissue to molecular levels: classical continuum biomechanical analyses are essential for relating global loads (blood pressure and flow) and local metrics such as stress and strain. Newly developed constrained mixture models employ lumped-parameter expressions of cell-mediated turnover of structural constituents to simulate growth and remodeling at a tissue level, agent based models address discrete cellular activity and production of diverse molecules, and finally molecular level models of both the mechanics (e.g., molecular dynamic models) and the reaction kinetics (e.g., intracellular signaling models) permit mechanistic considerations. Herein, we focus on linking the first three classes of models, that is, continuum, constrained and agent based models.

Continuum Biomechanics. The five basic postulates of continuum biomechanics are balances of mass, linear momentum, energy, and angular momentum plus the entropy inequality. Whereas the first three of these relations provide the requisite equations of motion, the last two provide restrictions on possible constitutive relations. Thus, in well-posed isothermal problems, one focuses primarily on balance of mass and linear momentum, that can be written, in the absence of body forces, as

$$\partial\rho/\partial t + \mathrm{div}(\rho\mathbf{v}) = 0, \;\; \mathrm{div}\mathbf{t} = \rho\mathbf{a} \tag{3.1}$$

where ρ is the current mass density, and $\mathbf{v}$ the velocity, $\mathbf{t}$ the Cauchy stress, and $\mathbf{a}$ the acceleration. Inertial loads are often negligible in arterial wall mechanics (Humphrey, 2002), hence one can treat deformations during the cardiac cycle as quasi-static (i.e., let

a = **0**). The governing equations are then closed mathematically via appropriate boundary conditions as well as a constitutive relation for the Cauchy stress, often written as

$$\mathbf{t} = -p\mathbf{I} + 2\mathbf{F}(\partial W/\partial \mathbf{C})\mathbf{F}^{\mathrm{T}} + \mathbf{t}^{act}, \tag{3.2}$$

where p is a Lagrange multiplier (which enforces isochoric motions during transient loading), **I** the identity tensor, **F** the deformation gradient tensor, W=W(**C**) the homogenized stored energy function, $\mathbf{C} = \mathbf{F}^{\mathrm{T}}\mathbf{F}$ the right Cauchy-Green tensor (which is properly invariant to rigid body motions), and $\boldsymbol{t}^{act}$ accounts for contributions due to smooth muscle contractility. Considerable research since the late 1960s has led to various forms of W to describe the complex, nonlinear, anisotropic behavior over finite strains that characterize arterial wall properties. These models are often phenomenological (e.g., the Fung-exponential), but nevertheless provide excellent approximations of the state of stress and thus considerable insight [47]. Two conspicuous shortcomings of classical biomechanical analyses, however, are the lack of attention to load bearing by individual constituents (e.g., elastin and fibrillar collagen) and the kinetics of G&R processes (e.g., cell and matrix turnover in evolving configurations).

Constrained Mixture Model. We will use a constrained mixture model that was originally written in MATLAB version 7.9.0.529 (R2009b) as a custom code by S. Baek and A. Valentin. CMMs build upon, but extend, classical continuum formulations. CMMs build upon, but extend, classical continuum formulations. Three primary differences involve the kinematics, the constitutive relation for the stress response, and

mass balance. Because classical modeling considers the arterial wall to be materially uniform, one only needs a single reference configuration, often taken as either unloaded or stress-free. In the case of a CMM, however, the wall is allowed to be materially-nonuniform, consisting locally of different families of constituents that can each possess unique material properties and reference configurations that may evolve. Humphrey and Rajagopal (2003) [37] suggested that one refer deformations of individual constituents to individual natural (stress-free) configurations while requiring all constituents to deform with the mixture (i.e. $\mathbf{x}^k = \mathbf{x}$ where $\mathbf{x}$ denotes current position). That is, constituents constituting the mixture are constrained to move together, hence the terminology CMM. Conceptually, the deformation gradient for each constituent k can then be thought of as $\mathbf{F}^k = \partial \mathbf{x}^k / \partial \mathbf{X}^k = \partial \mathbf{x} / \partial \mathbf{X}^k$ where $\mathbf{x}$ denotes current positions and $\mathbf{X}$ denotes reference positions. Assuming that cells tend to incorporate newly produced constituents within extant matrix at a preferred (target) pre-stretch or pre-stress, for which there is growing experimental support [48], Baek et al. (2006) [38] showed that the deformation gradient experienced by an individual constituent can be written as $\mathbf{F}^k_{n(\tau)}(s) = \mathbf{F}_o(s)\mathbf{F}_o^{-1}(\tau)\mathbf{G}^k(\tau)$ where s denotes the current G&R time and $\tau \in [0, s]$ denotes a past time at which the constituent was produced. Here, $\mathbf{F}_o$ denotes measurable deformations experienced by the vessel relative to a convenient original (reference) configuration and $\mathbf{G}^k$ denotes the preferred "deposition stretch," which can be prescribed. Finally, the subscript $n(\tau)$ reminds us that the deformation experienced by each constituent k is relative to its individual natural configuration defined at the time τ of production.

In addition, the stored energy function W in the CMM is assumed to be describable via a rule-of-mixtures approach, which conceptually can be thought of as $W^k = \sum \phi^k W^k$ where ϕ^k denotes a mass fraction for constituent k. Yet, to account for continual production and removal of different constituents within evolving stressed configurations, Baek et al. (2006) [38] proposed $W = \sum_{k=1}^{n} W^k$, where

$$W^k(s) = (\rho^k(0)/\rho(s))Q^k(s)\widehat{W}^k\left(\mathbf{C}^k_{n(0)}(s)\right) + \int_0^s (m^k(\tau)/\rho(s))q^k(s-\tau)\widehat{W}^k\left(\mathbf{C}^k_{n(\tau)}(s)\right)d\tau \tag{3.3}$$

where $\rho^k(0)$ are initial apparent mass densities (i.e., mass of constituent k per mixture volume) and $Q^k(s) \in [0,1]$ are evolving fractions of previously produced constituents that survive to current G&R time s, $\rho(s) = \sum \rho^k(s)$ is the overall mass density of the wall (essentially constant at 1050 kg/m^3 independent of turnover; Rodriguez et al., 1994), $\mathbf{C}^k_{n(\tau)}(s) = \left(\mathbf{F}^k_{n(\tau)}(s)\right)^T\left(\mathbf{F}^k_{n(\tau)}(s)\right)$ is the right Cauchy-Green tensor, and $m^k(\tau)$ and $q^k(s-\tau) \in [0,1]$ represent the production rate of mass density for that constituent and the evolving fraction of constituents produced at time τ that survive to time s, again with $\tau \in [0, s]$. Noting that $s = 0$ is the time at which G&R commences from a prior steady (homeostatic) state, the heredity integral contribution is similar to the concept of fading memory in nonlinear viscoelasticity; constituents contribute more to load bearing the more recently they were produced. Similarly,

$$\rho^k(s) = \rho^k(0)Q^k(s) + \int_0^s m^k(\tau)\, q^k(s-\tau)d\tau. \tag{3.4}$$

Examination of special cases reveals that these two evolution equations, for stored energy and mass density, yield desired results. For example, at $s = 0$, one recovers a standard rule-of-mixtures relation for the stored energy and the appropriate constituent mass density because $\phi^k(0) = \rho^k(0)/\rho(0)$ and $Q^k(0) = 1$; the same is true for continual turnover in unchanging configurations, which we call tissue maintenance [42].

Of central importance, however, are the three classes of constitutive relations required in this CMM: $\hat{W}^k(\mathbf{C}^k_{n(\tau)}(s))$, $m^k(\tau)$, and $q^k(s-\tau)$. The first class of relations describes elastic behaviors of individual constituents, which are reasonably well known (e.g., neoHookean-type behavior of elastin and exponential behavior of undulated fibrillar collagen); see Valentin et al. (2009) [42] for functional forms and parameter values. The second and third classes of relations model cell-mediated production and removal of individual constituents, which heretofore have been assumed to depend on differences in stress from their target (homeostatic) values, which is to say via lumped parameter models that reflect known empirical correlations. For example, one can consider

$$m^k(\tau) = m^k_{basal}\left(1 + K^k_\sigma \Delta\sigma - K^k_{\tau_w}\Delta\tau_w\right), \tag{3.5}$$

where the *K*s are non-dimensional gain-type parameters, $\Delta\sigma = (\sigma^k - \sigma_h)/\sigma_h$, with σ_h a homeostatic target value of intramural stress (often ~ 100 kPa), and similarly for the wall shear stress τ_w. This basic relationship is motivated by the aforementioned observations that altered intramural stress modulates the production of collagen by smooth muscle cells [29, 49] while shear stress regulated vasoactive molecules can hasten or slow such production [50, 51]. Clearly, the production rate equals its basal value as it should when

differences in stress from target values are zero. Note, too, that because of the use of normalized stress differences, it is easy to bind the associated gain parameters. For example, wall stress is expected to increase initially by 2- to 3-fold in hypertension (Humphrey, 2002) while the production rate is expected to similarly increase on the order of 3- to 5-fold [36]. Hence, reasonable values are K_σ^k & $K_{\tau_w}^k \in [0.1, 10]$, which were verified parametrically by Valentin and Humphrey (2009b) [52].

Similarly, we can let constituent removal be governed by an equation of the form

$$q^k(s-\tau) = e^{-\int_\tau^s K_q^k(1+K_d^k \Delta\sigma^2)d\tilde{\tau}}, \tag{3.6}$$

where the *K*'s are rate-type parameters having units of inverse time and $q^k(s-\tau) \in [0, 1]$. Note, that if the stress equals its homeostatic value, then one simply recovers a simple first order decay with a rate constant K_d^k, which equals inverse the half-life. It is also interesting to note that equation (3.4), both at s = 0 and for tissue maintenance, provides restrictions on inter-relationships between production and removal parameters, namely $\rho^k(0) = m_{basal}^k / K_q^k$, which provides another internal means of bounding parameter values. Finally, note that Valentin et al. (2009a) [53] show that basic hypotheses underlying the CMM (e.g., existence of deposition stretches and stress mediated turnover) are useful for capturing reported observations. In other words, because of the structural and biological motivation for many of the relations, there exist many natural bounds on parameter values that promise to facilitate future patient-specific modeling. As noted above, however, changes in intramural stress (or strain) do not control the production or removal of collagen directly; for example, they can change the production of or responsiveness to ANG-II, which in turn affects the growth factor

production that controls collagen production and/or change the production or activation of proteases. Similarly, altered wall shear stress modulates the expression of endothelin-1 (ET-1), which stimulates smooth muscle cell production by increasing growth factor production [54, 55]. Hence, although lumped parameter models representing empirically observed correlations are sufficient for tissue-level modeling, yielding emergent behaviors that reflect diverse experimental and clinical observations, there is an opportunity to model the underlying bio-chemo-mechanical mechanisms more directly.

Agent Based Model. The agent based model is primarily written in Net Logo version 4.1 (Wilensky, U. 1999. http://ccl.northwestern.edu/netlogo/) as a custom code formulated by B. Thorne and H. Hayenga. Two-dimensional ABMs can simulate the cross-section of an artery (at $s = 0$) comprised of a large number of total cells ('agents'), including fibroblasts (FBs), layers of smooth muscle cells (SMCs), and a monolayer of endothelial cells (ECs) representing the adventitial, medial, and intimal layers, respectively. Indeed, even invading monocytes/macrophages can be modeled individually. Each cell can only occupy a single pixel at any given time, however, and thus overlapping cells are not allowed. Each cell ('agent') is capable of exhibiting behaviors characteristic of the particular cell type as well as altered behaviors in specific types of disease, as, for example, hypertension. These behaviors are prescribed by individual rules, which in turn are derived directly from data collected from diverse cell cultures and hence are relevant to many aspects of vascular physiology and pathophysiology. **Table 3.1** lists illustrative cell behaviors and the rules that govern them. For example, SMCs may proliferate (double) or migrate (move from one pixel to

another). SMCs may express and secrete (produce) diverse proteins, including growth factors (PDGF and TGF-β1), extracellular matrix (collagen type-I), and proteases, including matrix metalloproteinase-1 (MMP-1) that can degrade collagen. Levels of production of these factors by an individual SMC are regulated in part by the mean circumferential stress that each cell experiences at a given time (see **Table 3.1**) or possibly substances produced by other cells in response to other loads. ECs are similarly capable of producing vasoactive molecules (e.g., ET-1 and NO), growth factors, MMPs, and adhesion molecules that regulate interactions between blood borne cells (e.g., monocytes and platelets) and the endothelium. Non-structurally significant molecules, such as PDGF, TGF-β, MMP-1, MMP-2, MMP-9, ET-1 and NO, can diffuse locally to adjacent patches at a fixed rate and cause both vasoactive responses by SMCs or alter their production of collagen. For example, the diffusion rate for PDGF is 1%; therefore, at each time step, 1/8 of 1% of the total amount of PDGF at any given patch will be shared with each of the 8 neighboring patches. Each patch reciprocates by receiving and sending protein to nearby patches. The diffusion rates were arbitrarily set at a low value. When more specific diffusion functions are defined they can be implemented into the ABM. Molecules that diffuse into the luminal space are set to zero on the assumption that blood flow will remove locally produced proteins.

At each time step ECM and soluble factors are both accumulated and dissipated; the rate and functions for these processes is detailed in **Table 3.1**. For example, MMP-1 degrades collagen to gelatin, MMP-2 and 9 then degrade gelatin to nothing. If any MMP-2 or 9 is left they then degrade elastin to gelatin. Currently the half-life of the MMPs is arbitrarily assumed to be every time step (6 hrs). However, this can be modified when a more accurate value is reported. In addition, ET-1 and NO are produced according to literature derived functions. However, these molecules are neither dissipated nor used in the current model. Implementing appropriate diffusion functions will aid in the usefulness of these vasoregulator molecules. SMC production is dependent on PDGF, whereas SMC removal is constrained to produce mass balance equilibrium in homeostatic conditions.

Upon production and/or diffusion, it is typically assumed that 100% of the soluble factors bind to their respective targets (e.g., receptors or binding pockets) and impact cell behavior or matrix levels. For example, if a threshold level of PDGF is reached at a particular pixel, the chance of SMC proliferation at that discrete location will increase. That is, at G&R time t = s, a random number generator chooses an integer

TABLE 3.1. Literature derived rules that dictate the production, removal of cells and the surrounding matrix in the ABM.

Behavior	ABM Rule	Citation
SMC proliferation chance	100 in $(m(PDGF)+b)$/cell/6hrs $m=-1.45\text{E}-09$, $b=8.0\text{E}04$ pg	[56], [57], [58]
SMC apoptosis chance	100 *in* 71020 /cell/6hrs Mass balance constraint	NA
SMC production of PDGF (stretch induced)	$m\sigma_\theta+b$ $m=4.79\text{E}-07$, $b=-4.17\text{E}-05$ pg	[59], [60]
SMC production of TGFβ (stretch induced)	$m\sigma_\theta+b$ $m=1.65\text{E}-06$, $b=-1.03\text{E}-04$ pg	[61], [62]
SMC production of MMP-1 (constant)	$MMP1(t)+ba$ t = time, b = baseline = 2.70 pg/cell/6hrs, a = percent active = 39.32 %	[63], [64]
SMC production of MMP-2 (stretch induced)	$A\left(M\left(\delta+\alpha\left(1-e^{-\kappa\sigma_\theta^n}\right)\right)\right)$ A = % active = 0.001 M = max rate = 1 pg/cell/6hrs δ = 0.03, α = 0.52, κ = 2.0E-06, n = 2.84	[65], [66]
SMC production of MMP-9 (stretch induced)	$A\left(M\left(\delta+\alpha\left(1-e^{-\kappa\tau_w^n}\right)\right)\right)$ A = % active = 0.003 M = max rate = 0.018 pg/cell/6hrs δ = 0.04, α = 0.44, κ = 4.0E-06, n = 2.88	[65], [67]
SMC production of Collagen (TGFβ dependent)	if TGFβ and PDGF-AB present, $m\text{TGF}\beta+b$ $m=114.9$, $b=8.99\text{E}-03$ pg otherwise, basal production = $8.99\text{E}-03$ pg	[68], [69], [70]
EC production of NO (flow induced)	$\widetilde{\tau_w}=0, NO=0$ $0<\widetilde{\tau_w}<1, NO=0.5$ $\widetilde{\tau_w}\geq 1, NO=m\widetilde{\tau_w}+b$ $\widetilde{\tau_w}=\tau_w^{mouse}-(\tau_{wh}^{mouse}-\tau_{wh}^{BAEC})$ $m=0.272$ pmol/s, $b=0.22$ pmol/s	[71]
EC production of PDGF (flow induced)	$M\left(\delta+\alpha 1-e^{-\kappa\tau_w^n}\right)$ M = max rate = 0.078 pg/cell/6hrs δ = 0.15, α = 0.84, κ = 0.42, n = 1.24	[72], [73]
EC production of ET-1 (flow induced)	$M\left(\delta+\alpha\left(1-e^{-\kappa\tau_w^n}\right)\right)$ M = max rate = 4.8E-03 pg/cell/6hrs δ = 0.60, α = 0.40, κ = 3.63, n = 1.68	[74], [75]
MMP-1 reduction of collagen to gelatin	150 pg collagen/pg MMP-1/6hrs	[76], [77]
MMP-2 reduction of gelatin	410 pg gelatin/pg MMP-2/1hr	[78], [79]
MMP-9 reduction of gelatin	135 pg gelatin/pg MMP-9/1hr	[78], [80]
MMP-2 reduction of elastin	For remaining MMP-2, 2.64 pg elastin/pg MMP-2/1hr	[78], [79], [80]
MMP-9 reduction of elastin	For remaining MMP-9, 0.87 pg elastin/pg MMP-9/1hr	[78], [79], [80]
MMP-1 removal	MMP-1/2/6hrs	NA
MMP-2 removal	MMP-2/2/6hrs	NA
MMP-9 removal	MMP-9/2/6hrs	NA

between 0 and $m(PDGF) + b$, where in homeostasis this value is 80,000. If the number is less than 100, then the cell proliferates; if the number is larger than 100, then the SMC remains as is for the current time step. This process repeats for each time step in the simulation. To achieve proper tissue maintenance (i.e. balance production and removal in homeostasis) this stochasticity is also applied to the rule dictating SMC apoptosis, except the range in values for the random number generator varies. That is, instead of choosing an integer between 0 and 80,000 (in homeostasis), the integer can be chosen between 0 and 71,020. MMP-1 degrades collagen I, and in the ABM the total amount of collagen at a given pixel is reduced proportional to the concentration of MMP-1 [81]. Whereas the rules in **Table 3.1** were derived from the literature, it is notable that in many cases the available data are as yet incomplete and in some cases they are conflicting.

ABM Rule Scoring. Fundamental to identifying appropriate ABM rule sets is a consistent strategy for data mining or experimental planning. Therefore, the quality of the papers underlying each rule was evaluated based on a systematic and semi-objective set of criteria. These criteria were based on 5 categories: (1) article agreement, (2) physiological methods, (3) distant metric to computational model, (4) source credibility, and (5) data type. That is the articles that each ABM rule is built from was rated on a scale of 1 to 10 according to categories 1 through 5. For example if the value in question, say the baseline value of TGFβ produced by vascular SMCs is 35 pg/mL/day [62], is roughly agreed upon by 7 or more other sources than category (1) would receive a score of 10. If 5 to 6 articles agree a score of 9 is given, if 3 to 4 articles a score of 7, 1

to 2 articles a score of 5 and if no articles agreed with this statement a score of 0 was given. Category (2) measured how close the experimental system was to in-vivo, and if calculations were made, whether or not they accounted for nonlinearities, anisotropy and heterogeneity. It is important to consider how close the species, organ, cell type or environmental condition is to that being simulated. Therefore, category (3) was scored according to how close these metrics (i.e. species, organ, cell type, and environmental condition) were to that we were simulating (i.e. mouse, artery, either EC or SMC, and in vivo); where a score of 10 was given if they matched, 5 if it was close, or 0 if they were not similar. Factors that give credence to an article may include the journal impact factor, number of times the article was cited or universal acceptance of experimental techniques. Thus category (4) was based on these credibility measurements; however scores from this category were not included in the overall score because these values can be misleading. For example if a statement is made incorrectly it may be cited by many others as being flawed. Lastly, category (5) considers how accurately the data were acquired. If the value in question was measured directly, quantitatively, and contained a lot of data points it would receive a score of 10. Please refer to the caption of **Table 3.2** for a more detailed breakdown of this scoring regime. Due to the continuing lack of data, if the average composite score amongst 2 researchers was above 50 the rule was considered in the ABM. If the score was below 50, a search for other articles to formulate a new but similar rule was conducted. If no alternative articles were found, than the values that make up the rule remained but the predicted outcomes as a result of

these rules were evaluated cautiously. In addition, these values were parameterized and allowed to vary within a bounded range (see Chapter IV).

ABM Parameter Sensitivity Analysis. In addition to scoring the confidence in the rules, a 1-D parameter sensitivity analysis was performed for all 37 parameters in the ABM. The sensitivity analysis will guide the suitable upper and lower bound for each parameter thereby allowing the model to be adjustable, but still predict the physiological behavior. Thus, an individual parameter was increased and then decreased by an order of magnitude while fixing all 36 other parameters at their prescribed value. Due to the inherent ABM stochasticity, the ABM model was run 100 times for each of these parameter sets. The predictions were then averaged and plotted ± the 95% confidence interval. If the confidence interval of the predicted results (using the initial parameter and the varied parameter) overlapped the predicted results (using the initial parameters) the model was considered to be insensitive to that parameter. However, if the confidence intervals did not overlap (i.e. the increase or decrease in parameters caused significant changes of the outputs), another, more detailed, sensitive analysis was performed. That is, the parameters were varied up and down by 1.5, 2, 5, and 10 times their original value. Again confidence intervals were calculated for the results. The maximum and minimum parameter change that resulted overlapping confidence intervals was deemed the upper and lower bound respectively, for the parameter. This sensitivity analysis allows us to know the range of which a single parameter can vary and still have the potential to give a physiological response under homeostatic conditions.

Model Verification and Integration

Once formulated, each model must be verified; that is, it must be shown to yield expected results. With modeling arterial G&R, which is inherently a dynamic process, a fundamental requirement is that the model is predicatively stable. For example, in the absence of perturbed hemodynamic loads, the model should predict unchanging geometry, properties, and function due to balanced turnover in a stable configuration over long periods (i.e., tissue maintenance) and it should be stable against reasonable transient perturbations.

Tissue Maintenance. Both the CMM and the ABM are numerically stable under both baseline conditions and in response to a transient perturbation in blood pressure. In particular, the CMM accounts for a production of new collagen fibers and smooth muscle, each deposited according to individual deposition stretches and aligned properly, that balances removal [53]. This outcome is appreciated by observing the arterial response to a modest increase in pressure that lasts but one time increment (6 hours in this case). Similarly, based on independently identified but otherwise interdependent rules, the ABM balances the production and removal of SMCs when the applied loads remain constant over extended periods. For example, although there is a 100 out of 80,000 chance of a SMC proliferating every 6 hours but a 100 out of 71,020 chance of SMC apoptosis every 6 hours, it is assumed that cell proliferation happens before apoptosis. Thus, over time, the greater chance of cell apoptosis balances out increases in mass due to proliferation.

For the illustrative example used herein – homeostatic production of collagen and smooth muscle in a representative mouse abdominal aorta subjected to constant flow but possible changes in pressure – we assumed baseline conditions whereby the overall (i.e., mixture) mass density is 1.05 g/cm^2 and mass fractions for collagen, elastin, and smooth muscle, respectively, are 0.44, 0.28, and 0.28 [82, 83]. The ABM simulates the cross-section of an 521.2-micron outer diameter mouse aorta (at G&R time $t = 0$), comprised of 472 total cells ("agents") including 319 smooth muscle cells and 153 endothelial cells representing the medial and intimal layers, respectively. Moreover, we set the vessel be axisymmetric and have an average thickness of 30.6-micrometers, which results from 2 to 4 layers of SMCs and 1 layer of endothelial cells [**Fig. 3.1**]. In order to simplify the ABM and reduce the total number of simulated cells, we excluded the adventitia, which is equivalent to assuming that the behaviors of the fibroblasts and extracellular matrix constituting this layer contribute minimally to the remodeling response relative to the behaviors of the smooth muscle cells and endothelial cells, which are the focus of this first-generation model. This constraint was applied primarily so that the ABM can match the structure of the CMM. However, fibroblasts have been reported to play a role in arterial remodeling due to vascular diseases [84]. Therefore, future generations of the ABM and CMM can include these cells as well as additional molecules. Each cell occupies a single pixel, represented as a 100 μm^2 area, at any given time, and there are no overlapping cells. Likewise, at G&R time $t = 0$, the CMM simulates nearly the same initial axisymmetric mouse abdominal aorta with a 528.2-micron outer diameter and wall thickness of 30.1 microns [85].

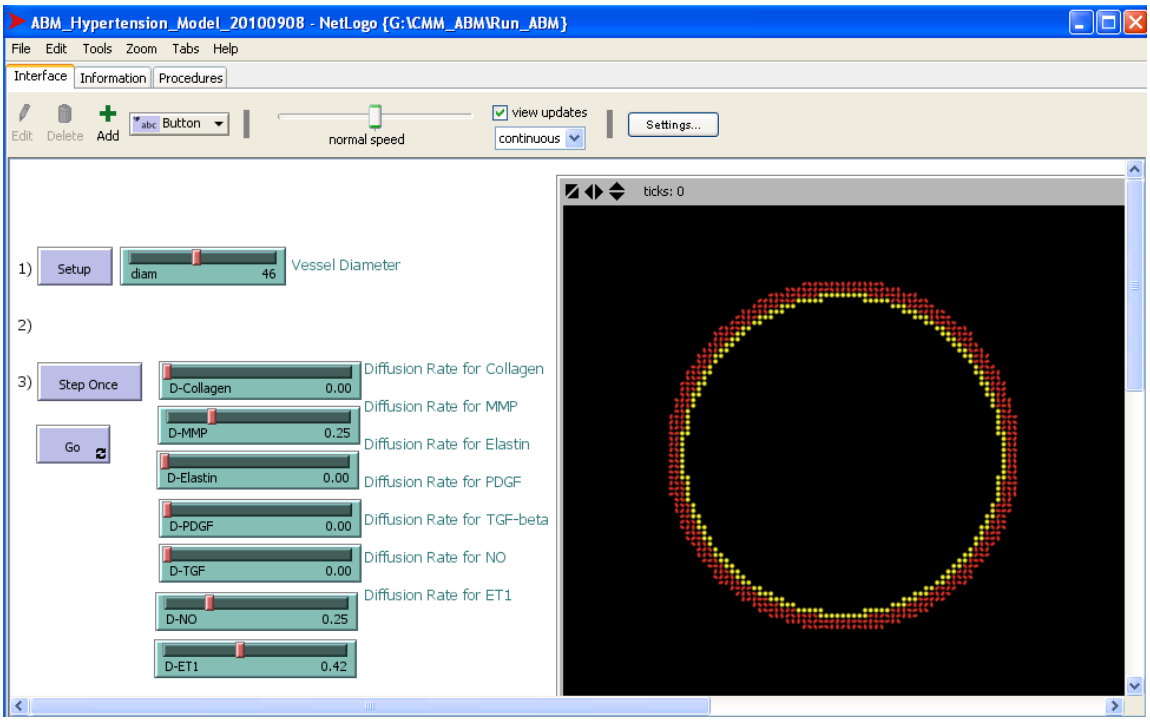

FIGURE 3.1. Screen shot of the ABM, displaying a 2-D representation of the model mouse abdominal aorta on the right and user controls as well as a display of progress on the left.

Each time step in the simulation represents six hours, and a total of one hundred days was simulated. The output of the ABM at each time step includes both a graphical depiction of each cell [**Fig. 3.1**] and a text file that lists, for each pixel, the following information: X-coordinate, Y-coordinate, total mass of collagen, muscle, elastin, newly deposited collagen and muscle since the last time step, concentration of MMP-1, PDGF, TGF-β, NO, and ET1, and the total number of SMCs. ABM simulations were run at least 5 times and the outputs were averaged; this was done primarily due to stochasity in the rules dictating SMC proliferation and apoptosis. Whereas the ABM uses an intra-

relational rule set to balance matrix production and removal in equilibrium, with wall thickness depending directly on accumulation/removal of cells while the inner radius remains constant, the CMM uses a Newton-Raphson method to determine the inner radius and wall thickness of the axisymmetric artery that satisfies mechanical equilibrium during cell and matrix turnover. Because the two models can share some outputs in common, this provides a unique opportunity to compare such predictions at an intermediate level of computation and iteratively refine associated parameters to increase congruency across scales.

Results

Table 3.2 illustrates one representative rule governing the ABM, production of PDGF by SMC as a function of stretch, and the degree of inaccuracy inherent to that rule based on a scoring by two researchers. Confidence in the literature was achieved if multiple papers agreed on the findings [**Table 3.2(*)**], the methods were physiological [**Table 3.2(**)**], the sample was close to that being modeled, and data collection and representation were deemed to be accurate [**Table 3.2(***)**]. In this example, researcher 1 found no supportive articles corresponding to the baseline production of PDGF by SMCs as found by Li et al., 1995 [59], whereas researcher 2 found 1 article. Similarly, researcher 1 found 4 articles [86-89] in agreement with stretch increasing SMCs production of PDGF [60], whereas researcher 2 found 1. Slight differences were seen in the other scoring categories as well, leading to different average confidence scores for each article. The composite score (found by averaging the scores for each article making up a single rule) was 52.55 for researcher 1 and 60.42 for researcher 2. Due to inherent

inaccuracy to experimental testing of biological tissues, rules that had a composite researcher rating >50% (including the example shown here) were considered acceptable and implemented in the ABM. Rules that had a composite score <50% were also implemented into the ABM as placeholders until more accurate literature becomes available. In particular, the rules governing production and degradation of MMP-2 or 9 [65-67] scored low in categories 3 and 5 resulting in an overall composite score of around 45. Whereas, the composite score for the rules governing the amount of gelatin that is degraded per hour by MMP-2 or 9 [78-80] were around 75. However, because the amount of MMP-2 or 9 produced and removed play such a crucial role in elastin degradation, the predicted values of elastin by the ABM should not be considered accurate until the pertaining rules are improved.

Parameter sensitivity analysis was performed on the parameters that make up the acceptable rules. **Figure 3.2** shows illustrative results for the parameter δ in the rule for ET-1 production in response to wall shear stress rule. Increasing or decreasing this parameter by an order of magnitude results in little overall change of predicted SMC number, collagen mass, hoop stress, PDGF mass, and TGFβ mass over time in homeostatic conditions. Because the 95% confidence intervals overlapped in this case, the rule was deemed to be relatively insensitive to this parameter and it was fixed at the literature determined baseline value. That is, the model appears to be insensitive amongst significant fluctuations in this parameter.

TABLE 3.2. Example of confidence scoring regime for an ABM rule dictating how much PDGF is produced by a SMC as a function of hoop stress. Rubric detailing point ratio is mentioned below the table for categories 1, 2 and 5. Scoring was based on 4 of the 5 categories. Category 4 was not included in the total confidence score. If the category had multiple subcategories, only the average was used (e.g. 3. and 5.) to calculate the average confidence. The average confidence values for all the literary references making up a rule were then averaged to give the composite score for any given researcher.

	Researcher 1 Scoring		**Researcher 2 Scoring**	
Rule	**SMC production of PDGF (stress dependent)**			
Relevant Papers	Li et al. (1995)	Ma et al. (1999)	Li et al. (1995)	Ma et al. (1999)
1. Article agreement*	0	7	5	5
2. Physiological methods**	6	4	6	6
3a. same species	0	0	0	0
3b. same organ	10	10	10	10
3c. same cell type	10	10	10	10
3d. same in vivo state	5	5	10	10
3. Distant metric total:	6.25	6.25	7.5	7.5
4a. journal Impact Factor	2.06	2.55	2.06	2.55
4b. citations	9	32	9	32
4c. experimental reliability	4	3	3	3
4. Source credibility total:	4	3	3	3
5a. numerical***	10	10	10	10
5b. measured directly***	7	7	5	5
5c. many data points***	2	4	2	2
5. Data type total:	6.33	7	5.67	5.67
Average Confidence:	4.65	5.86	6.04	6.04
Composite Score	52.55		60.42	

* The number of articles in agreement to score ratio is: 0:0; 1-2: 5; 3-4: 7; 5-6: 9; 7 and above: 10. If there are articles in disagreement subtract from the total articles in agreement.

** If the experiment was in-vivo, accounted for nonlinearity, anisotropy, and heterogeneity: 10; if ex-vivo, pre-conditioned, acute testing: 8; if ex-vivo, cultured, pre-conditioned: 6; if in-vitro, acute testing, environment like in-vivo: 4; if in-vitro, cultured: 2.

*** **5.a**. Numerical: 10, theoretical: 6, descriptive: 2. **5.b**. Measured directly: 10, measured indirectly: 7, extrapolated: 5, descriptive: 2. **5.c**. over 20 data points: 10, 16-20 data points: 8, 11-15 data points: 6, 6-10 data points: 4, 1-5 data points: 2.

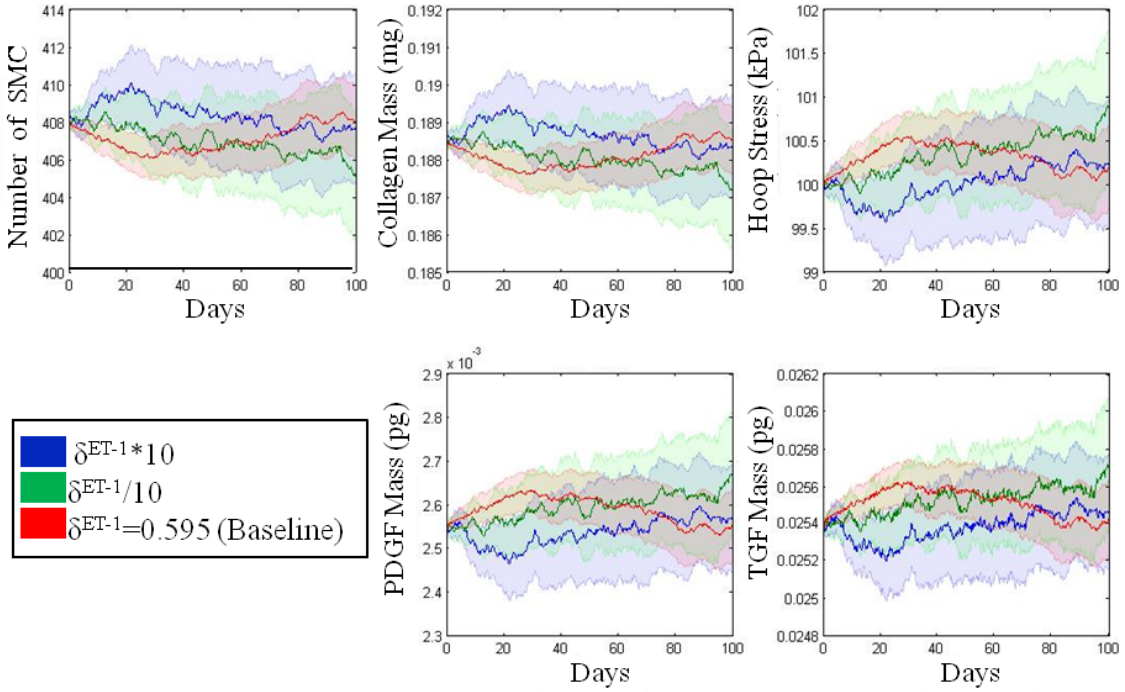

FIGURE 3.2. Parameter sensitivity analysis for the parameter δ in the rule for ET-1 production (see **Table 3.1**). This rule states that the production of ET-1 by ECs depends on wall shear stress in a sigmoid fashion. Each solid line represents the mean value based on 100 replications of the ABM. Blue indicates the response when the parameter was increased an order of magnitude, green when the parameter was decreased an order of magnitude, and red when the parameter remained at its original value. The pastel colors represent the 95% confidence intervals surrounding each result.

In cases where the confidence intervals did not overlap, an additional, more detailed, sensitivity analysis was performed by allowing the parameter of interest to vary by 1.5, 2, 5, and 10 times its original value. **Figure 3.3** shows an illustrative result for the sensitivity of the rule for SMC proliferation relative to its baseline value. In these cases, the sensitivity of the ABM to the particular parameter was noted and appropriate bounds were imposed to define allowable values (see Chapter IV).

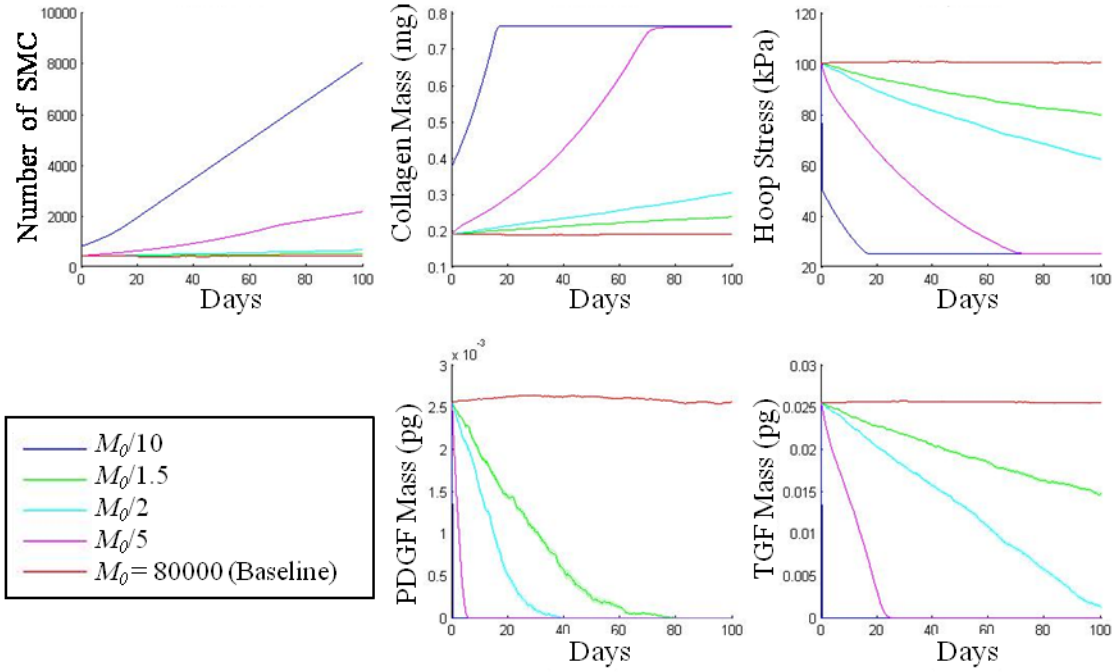

FIGURE 3.3. Parameter sensitivity results for the baseline SMC proliferation value (M_0). This parameter was multiplied or divided by 1.5, 2, 5, and 10 from its original value. Show here is only the case were it was divided.

Both the ABM and CMM acurately predict normal tissue maintance under stable physiological conditions. That is, both the ABM and CMM simulated constant arterial responses to constant mean pressure amongst two 10% increases arbitrarily assigned to persist for 6 hours (i.e., one computational increment in time) on both days 1 and 60 [**Fig. 3.4 (A)**]. The parameters used for these simulations were fixed at their initial values. The CMM predicted no net change in radius and mass when the pressure was constant. However, the transient increase in pressure resulted in a passive 0.7% increase

of inner radius [**Fig. 3.5 (A, CMM)**] and a 0.6% decrease in wall thickness [**Fig. 3.5 (A, CMM)**]. These modest changes caused a slight increase in collagen and smooth muscle fiber tension and decrease in wall shear stress [**Fig. 3.4 (C, CMM)**]. According to the mass production function [**equation 3.5**], changes from normalcy in fiber tension and wall shear stress caused an increased production of SMCs and collagen that manifested as a gradual increase up to 0.2% in SMC mass and 0.18% in collagen mass [**Fig. 3.5 (C, D, CMM)**]. Due to both the lack of elastin production past the perinatal period and its longterm stability (half-life ~ 35 years), it was neither produced nor removed within the CMM [**Fig. 3.5 (E)**]. As noted earlier, ABM did not predict elastin since the rules governing elastin production/removal are not well established. Under homeostatic pressure conditions with transient increases in pressure [**Fig. 3.4**], the chance of SMC proliferation and apoptosis were each nearly constant as was the hoop stress at 100 kPa, as predicted by the ABM. Therefore, production and removal of cells "agents" was balanced and there was effectively no change in matrix mass [**Fig. 3.5**].

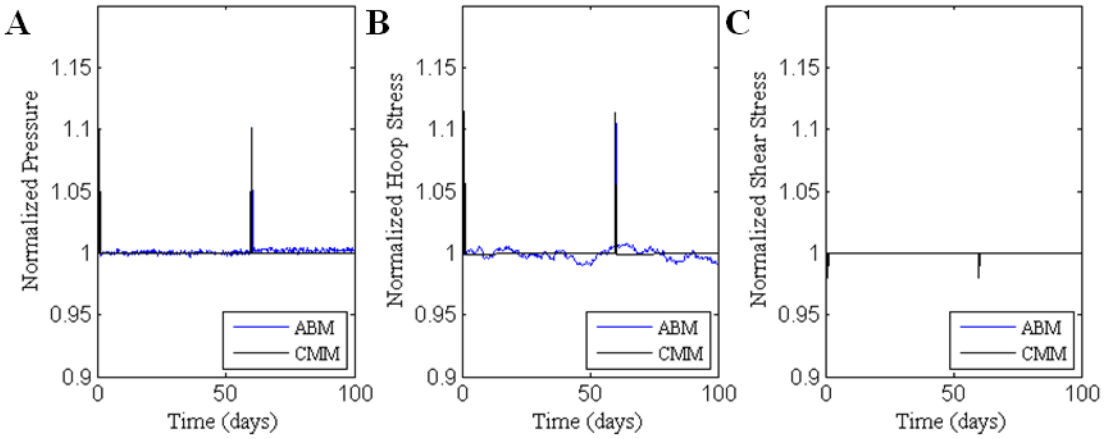

FIGURE 3.4. (**A**) A transient increase in pressure results in a transient increase in (**B**) hoop stress and decrease in (**C**) shear stress. The CMM predicts an acute increase in inner radius and associated decrease in shear stress that promote an acute thinning of the arterial wall, due to incompressibility. The stochastic nature of the ABM renders the inner radius and wall shear stress insensitive to small transient changes in pressure as expected.

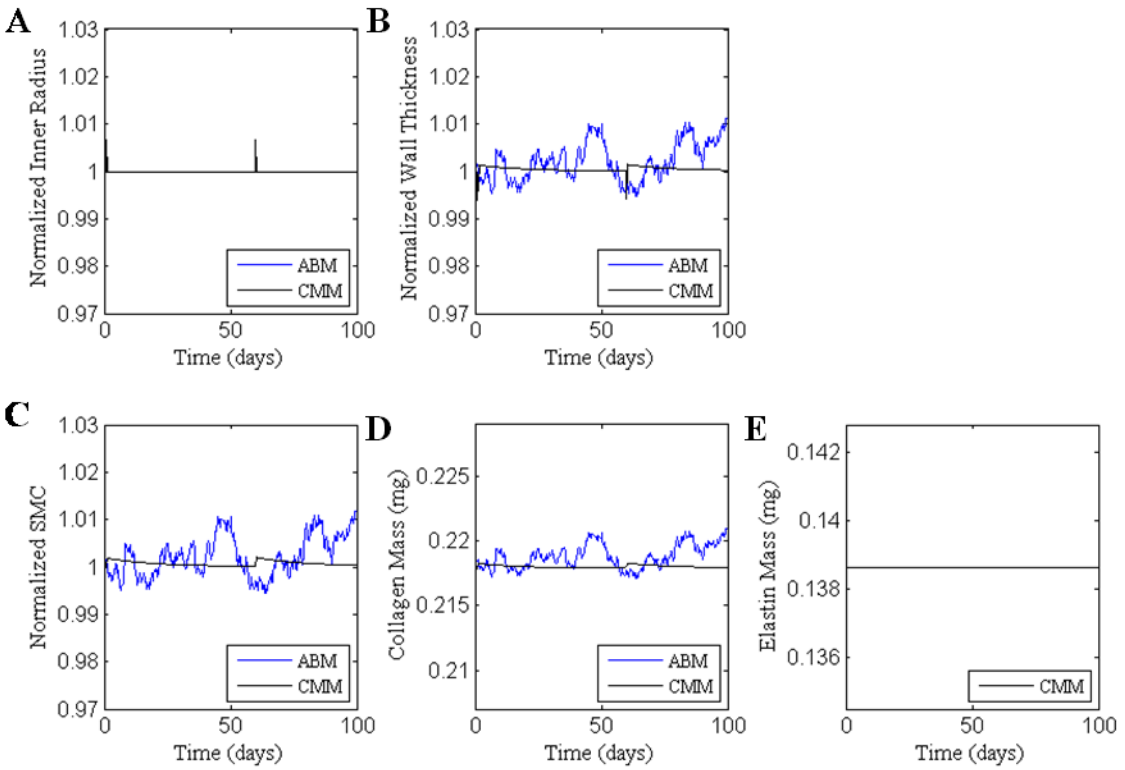

FIGURE 3.5. The artery recovers its basal geometry after a transient 10% increase in pressure over 1 time step (6 hours). Both models maintain appropriate basal levels of structurally significant constituents after the transient 10% increase in pressure.

Relatively speaking, it was found at the tissue level that the ABM was insensitive to modest changes in applied loads. At the molecular level, however, the ABM captured the dynamic synthesis response. That is, over the 6 hours of increased pressure, TGF-β increased ~26.3%, PDGF increased ~75.4%, MMP-2 increased ~14.4%, and MMP-9 increased ~5.1% over baseline. These values were promptly returned to the basal value after the pressure returned to normal. MMP-1 did not increase even transiently, meaning that collagen-1 degradation to gelatin was not increased above normality. The increase in

MMP-2 and MMP-9 was not significant enough to cause removal of gelatin mass even if it had been created [**Fig. 3.6 (F)**]

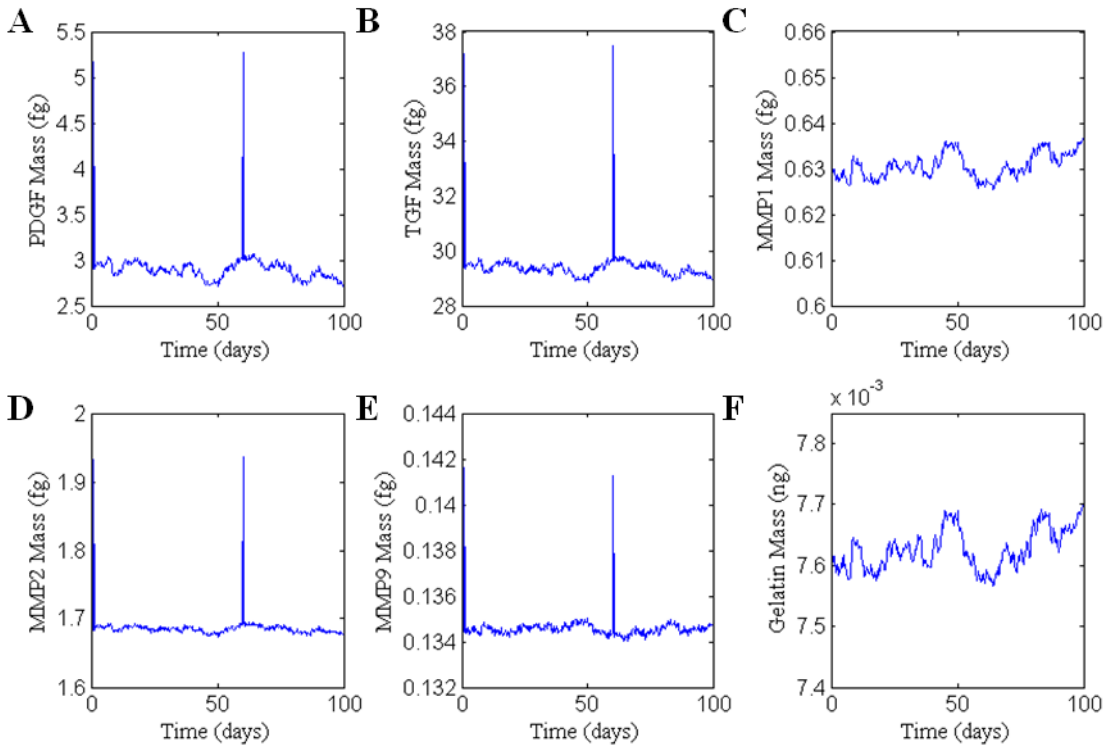

FIGURE 3.6. ABM predictions of the concentrations of PDGF, TGF- β, MMP-2, and MMP-9 show temporary increases in response to a 10 % increase in pressure over 6 hours. Collagen and smooth muscle amounts were not altered by these increases, however, as seen previously (see Fig. 3.3).

Discussion

We have presented a highly simplified representation of some of the key biochemical and biomechanical phenomena that drive arterial G&R in hypertension and that give rise to structural adaptations by the vascular wall. Our two-tiered model integrates inputs and outputs to and from both discrete (ABM) and continuum (CMM)

representations of the mechanobiology. In so doing, our multi-scale simulation links single-cell behaviors with tissue-level responses and enables us to verify predictions at both levels of scale by quantitative cross-comparison of key output metrics. This linking of phenomena across spatial scales promises to enable us to study how biochemical phenomena at lower scales influence mechanical phenomena at higher scales *and* how biomechanical phenomena at higher scales, in turn, impact biochemical phenomena at lower scales. By using congruent parameter values in the CMM and ABM, where possible, we are also able to answer the question: "To what extent can two very different modeling approaches arrive at the same predictions?"

Presented in this chapter is a systematic and semi-objective regime for determining suitable rules for agent based modeling. Conflicting or inconsistent data can make formulating rules difficult. Therefore this general approach can be applied to guide other ABMs. One of the limitations to our parameter sensitivity study is the fact that we only varied one parameter at a time while keeping all others fixed. This was done primarily due to the computationally expensive nature of the ABM. That is, each parameter takes a little over 8 hours (i.e. each simulation takes 5 minutes and there are 100 simulation replications) and there are 37 parameters. Therefore small changes in multiple parameters can potentially lead to predictions that diverge from physiological responses. However, the CMM has gone through a multivariable sensitivity analysis [52]. By comparing common predictions of the ABM and CMM through a genetic algorithm will allow the models to converge and predict a more physiological response.

This is achieved by knowing the CMM will only predict, within reason, physiological responses regardless of multivariable parameter combinations.

In conclusion, this work represents but another step toward the ultimate goal of developing models of the vasculature that are both descriptive and predictive, based on information gleaned from molecular, cellular, tissue, and organ levels. The present integration of the ABM and CMM represents one method of linking cellular and tissue levels, but there remains a need to link molecular mechanisms to cellular responses as well as a need to link tissue level manifestations to overall hemodynamics and transport. The former need may be facilitated by linking Intracellular Signaling Models (ISM), e.g. growth factors influence on gene regulation through the intracellular signaling pathways, to ABM [90]; whereas the latter may be facilitated by linking CMM with computational fluid dynamics (CFD) models that describe blood flow and transport in large portions of the vasculature [91]. Much remains to be accomplished, but rapid progress within each area promises future integration across scales.

CHAPTER IV

HYPERTENSION – MODELING

Overview

Hypertension results in significant changes in composition, geometry, structure, and mechanical properties of arteries. To capture the intricacies of such changes, there is a pressing need for inclusive models that can describe and predict both the mechanics and the biology. Continuum based biomechanical models are well suited for relating measurable blood pressures and flows to local metrics such as stress and strain, but not for describing cellular level mechanobiological and biochemical responses. Discrete stochastic agent based models are well suited to capture the biological complexity at a cellular level, but not tissue level mechanical changes. Thus, we coupled a constrained mixture model (CMM) with an agent based model (ABM) to predict better both salient mechanical changes and biochemical phenomena occurring during the progression of hypertension of a representative mouse abdominal aorta. A sustained increase in pressure of 30% is expected to increase the expression of both growth factors and proteases, and thus a proliferation of smooth muscle cells and deposition of collagen that results, in part, in an overall increase in wall thickness in a time-dependent manner while maintaining constant the inner radius. Early pressure-induced adaptations are expected to have little effect on elastin, however. Integrating literature based mechanisms originating at the cellular level with observed tissue level phenomenon allows for better prediction of response to hypertension.

Introduction

Hypertension remains a significant risk factor for many cardiovascular diseases, including heart failure, stroke, and end-stage renal failure. Hypertension causes, or is caused by, significant changes in the geometry, structure, mechanical properties, and function of arteries and arterioles. Because of the complexity of such changes, as well as their impact on the hemodynamics, there is a pressing need for increasingly inclusive computational models that can describe and predict both the mechanics and the biology. Indeed, it is increasingly realized that multi-scale models are essential for integrating information from the tissue/organ level, at which localized initiating diseases such as atherosclerosis present and are treated clinically, with information at the molecular/cell level, at which underlying mechanisms originate. In the previous chapter, we presented a new approach for integrating a tissue-level continuum mixture model (CMM) and a cell-level agent based model (ABM) that allows one to address better both the underlying mechanisms of arterial adaptation to altered hemodynamics and the associated macroscopic manifestation that is important clinically. To illustrate the potential utility of this multi-scale approach, we consider here the case of cell-mediated large artery adaptation to a sustained increase in blood pressure that is, to hypertension.

Pioneering work by H. Wolinsky, S. Glagov, and others in the 1960s and 1970s revealed the fundamental importance of continuum mechanics in arterial wall biology in general and hypertension in particular. Via comparative studies across species, Wolinsky and Glagov (1967) showed that increased aortic wall thickness correlates well with the increased caliber that is necessary to accommodate increased volumetric blood flows in

larger animals such that wall tension per lamellar unit is nearly constant at ~ 2 N/m [8]. That is, it became apparent that the normal aortic wall grows and remodels during development and maturation so as to maintain nearly constant the mean circumferential stress ($\sigma_\theta = Pa/h$, where P is pressure, a the luminal radius, and h the wall thickness; [92, 93]). Indeed, this general finding is consistent with an idea that emerged in hemodynamics during the same period, namely, that the aortic wall grows and remodels so as to maintain nearly constant the mean wall shear stress ($\tau_w = 4\mu Q/\pi a^3$, where μ is viscosity and Q the volumetric flow rate [92, 94]; the particular target value of which varies along the vascular tree and across species [95]. Among others, Wolinsky (1971) [49] suggested further that thickening of the aortic wall in response to hypertension is similarly consistent with the concept that mean circumferential stress is maintained nearly constant, a finding that has been confirmed by many others [96, 97]. During development, changes in wall tension associated with alterations in blood pressure closely correspond to differences in accumulation of transmural collagen and elastin in the ascending aorta and pulmonary trunk [7]. These and related findings emphasize the importance of stress analyses in continuum biomechanics, which is perhaps best illustrated by the seminal finding by Chuong and Fung (1986) [98]. They showed that residual stresses in arteries tend to homogenize the predicted transmural distributions of circumferential and axial stresses, which suggests that the arterial wall not only tries to maintain the mean stress at a preferred value, it also tries to maintain the transmural distribution at this mean [99]. Diverse studies suggest that axial wall stress plays a

similarly fundamental role in mechanical homeostasis and thereby affects adaptations by arteries in response to changes in mechanical loading or genetic defects [42].

The 1990s brought forth a logical extension of classical continuum biomechanical analyses to try to describe functional adaptations. Stress-mediated changes in arterial geometry and properties were modeled using classical balance relations and constitutive relations for stress augmented with extensions for the concept of kinematic growth introduced by Skalak (1981) [100]. Briefly, it was assumed that either gross geometry (radius or thickness) or associated deformations (stretch ratios) evolved whenever intramural or wall shear stresses differed from target values, with equilibrium enforced at each evolved configuration. For example, Rachev et al. (1996) [101] predicted macroscopic changes in arteries due to hypertension and Taber (1998) [102] predicted changes in aortic development. Similar studies based on kinematic growth continue to capture diverse consequences of arterial adaptations [103, 104]. Therefore, continuum models are capable of predicting the salient features of hypertension, but a need for integrative models to capture the molecular and cellular mechanisms applied to the tissue level has been expressed by many [39, 42, 53, 105].

A unique approach to predict cellular adaptation to perturbations is through Agent Based Modeling (ABM). Agent based modeling simulates the interaction of autonomous agents (e.g. individual cells) with each other and their environment based on a literature-derived set of rules to predict emergent patterns [106]. Classically, ABM has been used for ecological and sociological applications. Only recently has ABM been widely used for biomedical applications, as detailed in the review by [106]. As an

example, leukocyte adhesion and transmigration has been modeled from over 70 literature-based rules based upon adhesion molecule expression, soluble and surface-bound chemokines/cytokines and flow-mediated wall shear stress [107]. After knocking out selectins, the model predicts a change in flow velocity leading to less integrin activation resulting in decreased firm adhesion of monocytes [106]. This approach allows for better aggregate understanding of signal pathways and molecules crucial to the final outcome.

In order to create a comprehensive predictive bio-chemo-mechanical model of arterial growth and remodeling, one would need to consider the effects of hundreds of biochemically active molecules and their mechanical consequences on the arterial wall, and vice versa. If we restrict our consideration to the primary vasoactive, growth and regulatory, and proteolytic molecules, we consider NO (nitric oxide), ET-1 (endothelin-1), TGFb (tissue growth factor-beta1), PDGF (platelet derived growth factor), and MMP-1, -2 and -9 (matrix metalloproteinase-1, -2 and -9). In Chapter III we created a model that predicts soluble molecules as well as structurally significant insoluble constituents while allowing the artery to evolve dynamically over time. Herein we extend this model unification process through re-parameterization which allows for a more physiological prediction of clinical observations in the classical case of hypertension.

Methods

The constrained mixture model (CMM) was first introduced in 2003 by Humphrey and Rajagopal [37] which builds upon the modern theory of mixtures

proposed in 1957 by Truesdell and Noll. Since its introduction, the CMM has been refined and applied as a predictive model for normal and vascular disease conditions [38-42, 99, 108-111]. Details of the CMM use in these simulations can be found elsewhere (Chapter III; [42]); herein, we will reiterate the current growth and remodeling kinetics. The arterial wall consists of structurally significant constituents, *k*, (i.e. elastin, collagen and SMC) that are each described by specific strain-energy density relations relative to their individual natural configurations and mass fractions. The mass fractions depend on the rates of production,

$$m^k(s) = m^k_{basal}(1 + K^k_\sigma \Delta\sigma^k - K^k_{\tau_w}\Delta\tau_w), \tag{4.1}$$

and survival,

$$q^k(s,\tau) = \begin{cases} e^{-\int_\tau^s K^k_h d\tilde{\tau}} & \Delta\zeta(\tilde{\tau}) \le 0 \\ e^{-\int_\tau^s \left(K^k_h + K^k_h \Delta\zeta(\tilde{\tau})\right) d\tilde{\tau}} & \Delta\zeta(\tilde{\tau}) > 0 \end{cases}, \tag{4.2}$$

of that constituent. The basal mass density, m^k_{basal}, is the amount of constituent mass per unit area produced at each time step in normalcy; defined by calculating the constituent mass density fraction in normalcy divided by the mean age expectancy (according to the half-life) of that particular constituent. The gain-type parameters, K^k_σ and $K^k_{\tau_w}$ are unit-less scalars that weigh the specific constituent's dependency on either the difference in current intramural stress from homeostatic (~100 kPa), $\Delta\sigma^k = \frac{(\sigma^k - \sigma_h)}{\sigma_h}$, or similarly the difference in wall shear stress from its homeostatic value, $\Delta\tau_w$. Although, a decrease in $\Delta\tau_w$ results in an increase in mass production, and vice versa. For example, it has been shown that a decrease in WSS causes acute ET-1 induced arterial constriction in attempt to restore the WSS target value [33, 74, 112]. Increases in ET-1 have been shown to, in

turn, cause increased production of collagen [50, 113, 114] and SMC [50, 115]. Intramural stress expected to increase 2 to 3 times in hypertension (Humphrey, 2002) while production rate, $m^k(s)$, is expected to increase 3 to 5 times. Hence, in this simulation we allow the gain-type parameters to vary between a reasonable range of 0.1 to 10 [52].

The first order kinetic removal function (equation 4.2) is dependent on fiber tension, where $\Delta\zeta(\tilde{\tau})$ symbolizes the difference between current tension at time s, and homeostatic tensions deposited at time τ for k, either collagen or SMC. Elastin is assumed to neither be added nor removed since it is deposited during development and has a long half-life of 35 years [83, 116-118]. The rate-type parameter K_h^k accounts for constituent removal and is ~1/80 day^{-1} [92, 119]. Qualitatively, excess tension on a fiber leads to greater turnover due to increased MMP production and activity and therefore less constituent surviving from the time it was deposited, τ, to the current time, s [120-123]. It is important to note in a homeostatic state, where $\Delta\zeta(\tilde{\tau}) = 0$ and $m^k(s) = m^k_{basal}$ one can recover a constant apparent mass density, defined per unit area, $M^k(s) \cong M^k(0) \cong m^k_{basal}\int_{-\mathrm{A}^{\mathrm{k}}_{\mathrm{max}}}^{0} e^{-\int_\tau^s K_h^k d\tilde{\tau}} d\tau$ [42], where $\mathrm{A}^{\mathrm{k}}_{\mathrm{max}}$ represents the maximum age of the constituent. Therefore the CMM is good at predicting the salient features of hypertension. However, details of the intermediate molecules and their effect on cellular responses ultimately lead to these salient features are not accounted for in the current CMM.

Consequently we have previously designed an ABM to account for cellular production of the primary intermediate vasoactive, growth, regulatory, and proteolytic

molecules that exist under normal conditions (Chapter III). Briefly, a virtual artery in the 2D space domain is formed based off initial geometry and phenotype specifications. The artery consists of a single layer of endothelial cells and approximately 3 layers of SMCs. Each patch consists of a cell (or agent), matrix and biochemical factors and occupys an explicit 10 μm x 10 μm space. Each patch shares the physical space with the cell as well as other constituents (i.e. collagen and elastin). The total mass of SMCs at each time point, i, can be calculated as:

$$SMC_i^{mass} = V_i * \rho - C_i^{mass} - E^{mass} \tag{4.3}$$

where, SMC_i^{mass} is the current SMC mass of the vessel, V_i is the current vessel volume or total number of patches multiplied by the fixed volume per patch (1.0E-9 cm^3/patch), ρ is the mixture density (1.05 g/cm^3), C_i^{mass} is the current collagen mass of the vessel, and E^{mass} is the constant elastin mass of the mixture. Note that there is only one SMC per patch, but the mass and size of the SMC in the patch can evolve according to the mass of the other constituents occupying the patch. The average wall thickness of the vessel is calculated as,

$$h_i = r_a - r_l = \sqrt{A_i/\pi + r_l^2} - r_l \tag{4.4}$$

where, r_l is the constant luminal radius (230 μm) and A_i is the current vessel area or number of patches multiplied by the area for each patch (1.0E-6 cm^2/patch).

The behavior of each agent is determined by a selected set of 17 rules governed by 37 parameters. After a parameter sensitivity analysis, only 16 parameters caused the predicted amounts of SMC, collagen, PDGF, TGFb to diverge outside of the 95 %

confidence interval (Chapter III). Hence these parameters were rationally bound according to the sensitivity study.

A strategy common in multi-scale biomechanical modeling is to let the lower scale models sequentially inform the higher scale models, which ultimately should lead to tissue- or organ-level behaviors of clinical importance. The tacit assumption in such a strategy is that the lower scale models, or associated data, are more reliable. Although it is true that experiments at lower scales are often better controlled (e.g., cell responses in vitro under well defined conditions versus responses of the same type of cell in vivo wherein many conditions are neither controlled nor known), the physiologic relevance of findings at the lower scale is often questionable. One must consider, therefore, all factors that contribute to overall model reliability. We suggest that although an advantage of multi-scale modeling is that one can integrate disparate models that exploit different types of data and predict different types of behaviors, there should be some areas of overlap when crossing each scale that enable congruency across scales to be evaluated and possibly improved. For example, because the ABM is based on cell-level data whereas the CMM is based on tissue-level data, one would not expect the two models initially to predict the same values of common outputs, as, for example, the production of particular molecules by the ABM (e.g., collagen) and the accumulation of mass associated such molecules by the CMM. We illustrate how differences in outputs that overlap (i.e. collagen and SMC mass) can actually allow iterative parameter refinements across scales, which should lead to increased congruency between models. Indeed,

because all data and models at each scale each possess inherent errors, enforcing congruency may lead to increased biological and physiological relevance.

Previously, we have shown that the CMM and ABM paradigm can run in parallel to accurately predict clinically relevant arterial responses in homeostasis (Chapter III). This model was modified to include iterative internal congruency checks that allow a converged response to common metrics. That is, an objective function,

$$e = 2\sum_j^N \left(\overline{(C_{NT}^{ABM} - C_{NT}^{CMM})/(C_{NT}^{ABM} + C_{NT}^{CMM}) + (M_{NT}^{ABM} - M_{NT}^{CMM})/(M_{NT}^{ABM} + M_{NT}^{CMM})}\right)_j/N + 2\sum_j^S \left(\overline{|C_{HT}^{ABM} - C_{HT}^{CMM}|/C_{HT}^{ABM} + C_{HT}^{CMM} + (M_{HT}^{ABM} - M_{HT}^{CMM})/(M_{HT}^{ABM} + M_{HT}^{CMM})}\right)_j/S \quad (4.5)$$

was used as the fitness function in a Genetic Algorithm (GA) heuristic to find optimal parameters that result in minimum error between the common metrics (i.e. collagen and SMC) of the CMM and ABM. Where C denotes mass of collagen either for the ABM or CMM present at each 6 hour time step *j*. Likewise M denotes the mass of smooth muscle predicted by either the ABM or by the CMM. The percent difference of these common metrics were calculated and averaged for both the normotensive (*NT*) and hypertensive (*HT*) simulation. A hypertensive simulation consists of a 30 % sustained pressure increase at day 2. The homeostatic simulation was over 224 time steps or 56 days (*N*) whereas the hypertensive simulation was over 2000 time steps or 500 days (*S*). The GA randomly generates 40 parameter sets (i.e. the population size) within the allowable values for each parameter. Each parameter set is run through the CMM and ABM and

the percent difference for each time step in one simulation were summed and divided by the total number of time steps to give the total fitness value (or error) for any given set of parameters. The next generation stochastically selects 40 new parameter sets based on the best fitness values from the previous generation. The process continues until 30 generations have been completed. After error minimization, the best fit parameters were implemented into the CMM and ABM and their simulated results were plotted in the figure on page 59.

Based on results from parameter sensitivity studies conducted for the ABM (Chapter III) and CMM [42] parameters were either fixed or bound. **Table 4.1** details the values for the fixed parameters. For the ABM, parameters making up the rules governing ECs production of PDGF and ET-1 based on shear rates were fixed. The rules governing gelatinases MMP-2 and MMP-9 removal of cleaved collagen and elastin were also fixed. For the CMM the homeostatic deposition prestretch, or the stretch at which new constituent material is laid down at are fixed. Collagen and muscle have greater deposition stretch because they turn over in a matter of days whereas elastin is produced almost entirely in the neonatal period. That is the change in length per unit of the original length of the fiber is less for collagen and muscle than elastin; since original length for elastin is when the artery is a lot smaller. The elastic parameters are used in the neo-Hookean strain energy equation used to model elastin and in the Fung exponential strain energy equations used to model collagen and passive smooth muscle. The muscle activation parameters define the circumferential stretch at which the active response of muscle is maximum and minimum; as well as and the constrictor to dilator

ratio and scaling parameter that effects the magnitude of the smooth muscle response to stretch. Lastly, the mass fractions for collagen, elastin and muscle in the abdominal aorta were initially set at 0.44, 0.28 and 0.28 respectively; and allowed to vary at t > 0. These constitutes are removed according to a first order kinetic equation that is a function of rate-type parameters of mass removal.

For the ABM parameters bounds were chosen because the parameters were less known or the values resulted in imbalanced production and removal in homeostatsis (see Chapter III, methods and results) [**Table 4.2**].

TABLE 4.1. Fixed parameter values used in the ABM and CMM to simulate a mouse abdominal aorta. These values were inferred from the literature and deemed either to be reliable or to be reasonable based on parameter sensitivity studies.

Fixed Parameters
ABM
Growth Factors
$\delta^{PDGF} = 0.15, \alpha^{PDGF} = 0.84, \kappa^{PDGF} = 0.42, n^{PDGF} = 1.24$
$M^{PDGF} = 0.078\ pg/cell/6hr$
Vasoactive Factors
$\delta^{ET-1} = 0.60, \alpha^{ET-1} = 0.40, \kappa^{ET-1} = 3.63, n^{ET-1} = 1.68$
$M^{ET-1} = 0.01\ pg/cell/6hr$
Removal Factors
$\delta^{MMP-2} = 0.03, \alpha^{MMP-2} = 0.52, \kappa^{MMP-2} = 2.0E-06, n^{MMP-2} = 2.84$
$M^{MMP-2} = 1\ pg/cell/6hr, D^{MMP-2} = 99, A^{MMP-2} = 0.001$
$\delta^{MMP-9} = 0.04, \alpha^{MMP-9} = 0.44, \kappa^{MMP-9} = 4.0E-06, n^{MMP-9} = 2.88$
$M^{MMP-9} = 0.002\ pg/cell/6hr, D^{MMP-9} = 87, A^{MMP-9} = 0.003, D^{MMP-1} = 80.6$
CMM
Prestretches and Elastic Parameters
$G_h^e = 1.4,\ G_h^c = 1.08,\ G_h^m = 1.3$
$c^e = 58.8\ kPa,\ c_1^c = 560.4\ kPa,\ c_1^m = 12.7\ kPa,\ c_2^c = 22,\ c_2^m = 3.5$
Muscle Activation Parameters
$T_M = 150\ kPa, \lambda_M = 1.6, \lambda_0 = 0.83$
$C_B = 0.68, C_S = 0.68C_B, K^{act} = 1/20day^{-1}$
Initial Mass Fractions and Half-lives
$\phi^c(0) = 0.44, \phi^e(0) = 0.28, \phi^m(0) = 0.28$
$K_h^m = 1/80day^{-1}, K_h^c = 1/80day^{-1}$

TABLE 4.2. Parameter values and bounds used in the CMM (top 4 rows) and ABM (bottom 12 rows). See equations 4.1 to 4.2 and **Table 3.1** for the associated equations or rules.

Parameter	Initial Value	Lower Bound	Upper Bound	After Genetic Algorithm
$K_{\sigma_\theta}^{c}$	1	0.1	10	0.15
$K_{\sigma_\theta}^{m}$	10	0.1	10	0.44
$K_{\tau_w}^{c}$	1	0.1	10	6.16
$K_{\tau_w}^{m}$	10	0.1	10	8.18
$MMP\text{-}1_0$	2.69E-04	2.69E-05	2.69E-03	2.50E-03
$MMP\text{-}1_{\%A}$	0.39	0.039	3.93	0.28
C_0	0.009	0.0009	0.09	0.078
C_{TGF}	114.94	11.49	1149.42	865.90
M_p	-1.45E+09	-1.45E+10	-9.69E+08	-1.48E+09
M_0	80000	53333.33	120000	6.34E+04
M_{a1}	71020	7102	106530	1.00E+04
M_{a2}	100	66.66	1000	309.99
$PDGF_{\sigma_\theta}$	4.79E-07	3.19E-07	7.19E-07	5.37E-07
$PDGF_0$	4.17E-05	4.17E-06	6.25E-05	3.50E-05
$TGF\beta_{\sigma_\theta}$	1.65E-06	1.65E-07	1.65E+05	9.99E-06
$TGF\beta_0$	1.03E-04	1.03E-05	1.03E-03	9.94E-04

Results

Hypertension, defined herein as a sustained increase in blood pressure of 125.3 mmHg (i.e. 30% of the in vivo MAP of mice) was simulated using the ABM and CMM. In response to hypertension, specifically the increased hoop stress calculated based on the law of laplace, causes increased SMC production of PDGF. Proliferation of SMCs is proportionally related to the increases in PDGF above baseline. Therefore the arterial wall thickens as a result of increased SMC mass. **Figure 4.1** illustrates a mouse

abdominal aorta in normotensive conditions [**Fig. 4.1 (A)**] as well as after 500 days of elevated blood pressure [**Fig. 4.1 (B)**]. The endothelial layer is shown in yellow and the media in red. The inner radius and number of ECs is fixed. However this illustration shows the outward wall thickening.

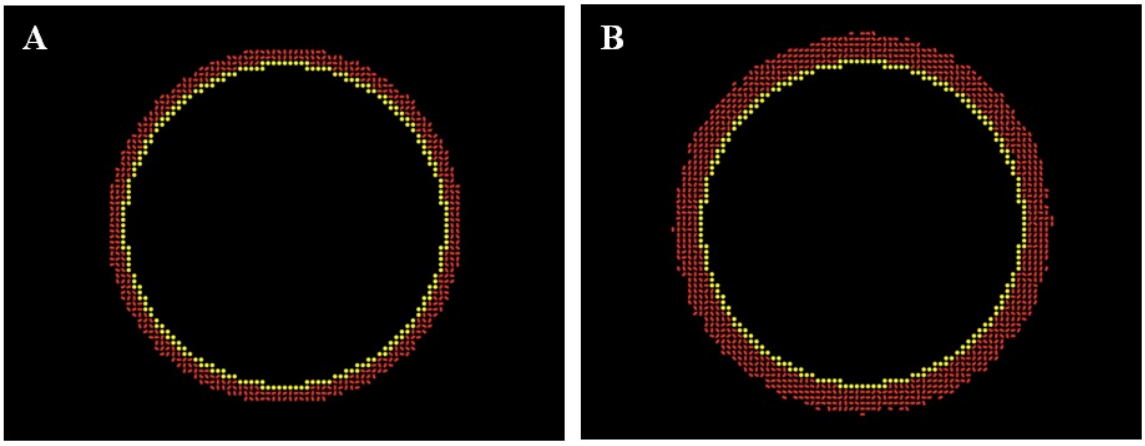

FIGURE 4.1. Graphical display of an ABM simulation of a mouse abdominal aorta (**A**) before and (**B**) after hypertension (defined herein as a sustained 30% increase in mean pressure).

Figures 4.2 - 4.4 illustrate the predicted arterial response by the ABM (shown in blue) and CMM (shown in black) to the sustained increase in pressure [**Fig. 4.2 (A)**] using the initial parameters as determined from the literature. For the CMM, the increase in pressure leads to passive increase in the internal radius [**Fig. 4.3 (A)**]. This causes increased wall stress, over the basal value, [**Fig. 4.2 (B)**] in addition to decrease shear stress [**Fig. 4.2 (C)**]. The stress is sensed by the constituent's results in mass accumulation [**Fig. 4.3 (D, C)**] and wall thickening [**Fig. 4.3 (B)**].

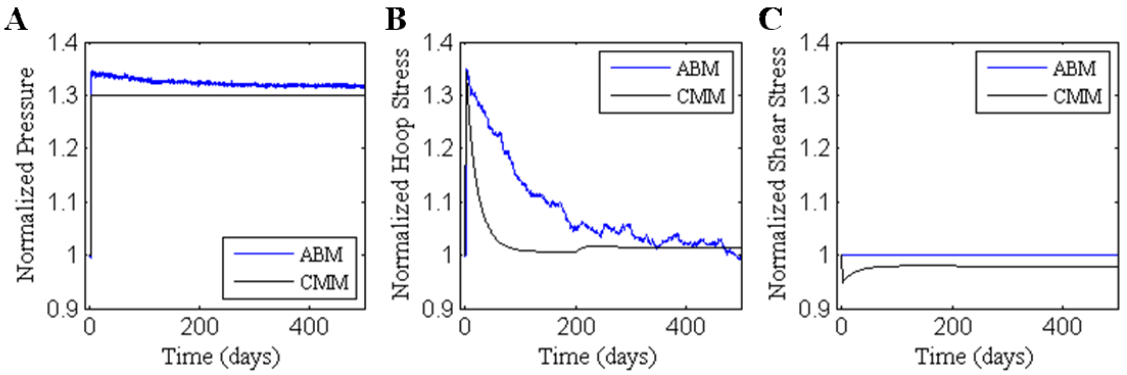

FIGURE 4.2. CMM and ABM predictions of (**A**) load and (**B, C**) stresses, normalized with respect to the homeostatic values, before parameter refinement via the genetic algorithm. Note that the pressure was prescribed in the CMM whereas the shear stress (actually inner radius) was prescribed in the ABM. The trends were similar for the evolution of hoop stress due, in part, to the initial effort of parameter selection (see **Table 4.2**).

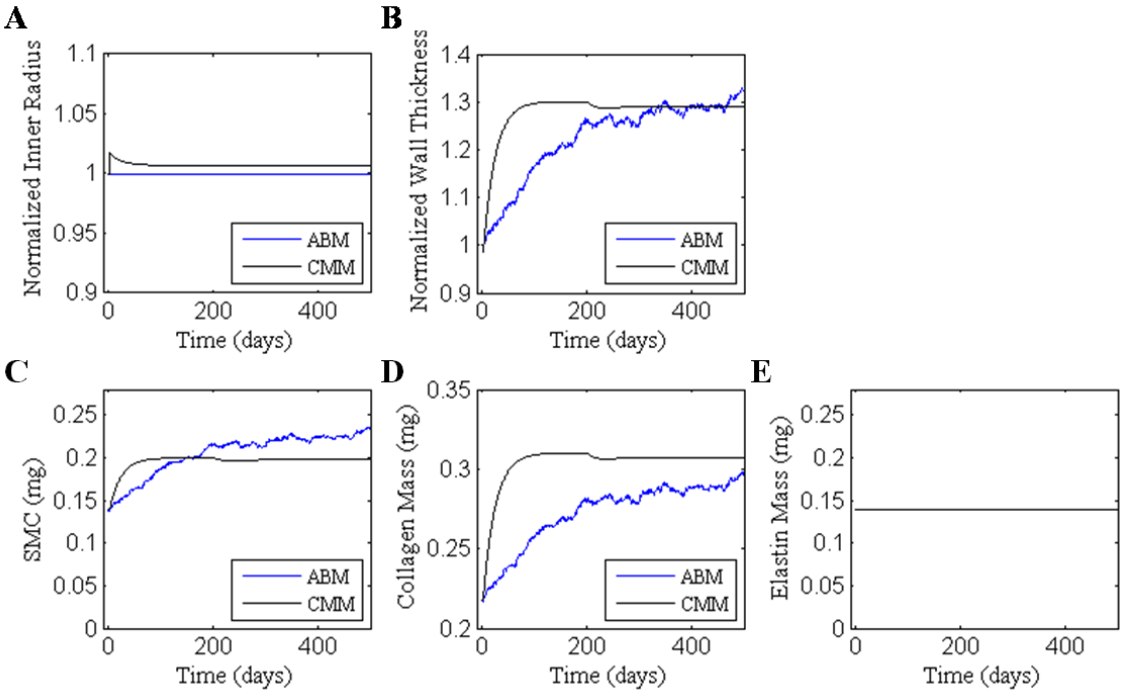

FIGURE 4.3. (**A**) Wall caliber, (**B**) thickness, and (**C-E**) constituent compositions for the case of a 30% increase in mean luminal pressure before parameter refinement. (**E**) Elastin is constant in the CMM and currently not predicted by the ABM.

The ABM behaves similarly to the CMM in that the increase in loads experienced by the cells leads to mass production and accumulation. In addition, the target thickness value of ~30% is reached for a 30 % increase in pressure. In the ABM the geometry is determined by number of cells, each containing a fixed size. Therefore, the increase in SMC number is going to have a direct correlation to the total thickness [**Fig. 4.3 (B, C)**]. Collagen, produced by the ABM, is contained within the same "patch" that a SMC occupies. In response to the increased stress smooth muscle cells produce TGF. When TGF is present, the rate of collagen production increases [**Fig. 4.3 (D), Fig.**

4.4 (B)]. The increase in collagen (as a function of TGF) is followed by collagen removal (as a function of MMP-1). Thus, when collagen amounts appear to plateau [**Fig. 4.3 (D)**] around day 220 so does the TGF and MMP-1 [**Fig. 4.4 (B, C)**]. Note that the concentrations of soluble factors are a product of the entire arterial volume at any given time step, hence the total mass of any particular constituent increases as the total mass of the arterial wall increases.

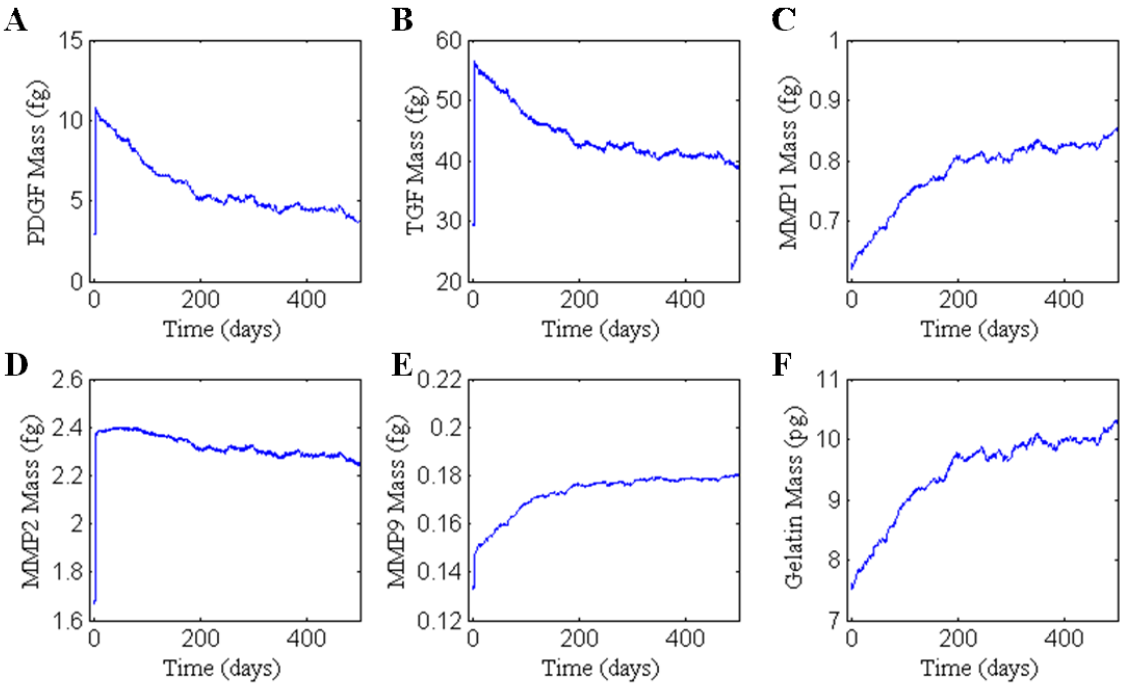

FIGURE 4.4. ABM predictions of changes in soluble constituents due to a 30% increase in mean pressure.

Reparameterization of the bounded parameters shown in **Table 4.2** was achieved using a genetic algorithm to minimize the percent difference, at each time step, of 2

common outputs, collagen and SMC mass. The mean percent difference between the common outputs was 5.1%. The parameter set chosen is documented in the right-most column of **Table 4.2**. The results after implementation of these parameters are shown in **Figure 4.5**. As seen before, a 30% step increase in pressure (fixed by the CMM, calculated by the ABM) [**Fig. 4.5 (A)**] immediately causes the hoop stress to increase 34% and wall shear to decrease due to passive distention and wall thinning of the artery [**Fig. 4.5 (B-E, CMM)**]. Now, both models predict the characteristic arterial observations due to hypertension (i.e. proportional wall thickening to the increase in pressure, elevated SMC and collagen mass, nearly constant inner radius and wall shear stress, and recovery of the target circumferential stress). Moreover, both the ABM and CMM were able to modify their parameters to allow for consistency across the common metrics SMC and collagen mass [**Fig. 4.5 (F, G)**] as desired. Remarkably the wall thickness, based off structurally significant constituents in the CMM and number of patches in the ABM, were also very similar [**Fig. 4.5 (E)**]. In addition, the ABM predicts a rapid increase in growth factors, metalloproteinase's, and gelatin mass. Note the sustained increase in mass corresponds to the sustained increase in wall thickness after the artery appears to have remodeling in a new basal state ~120 days.

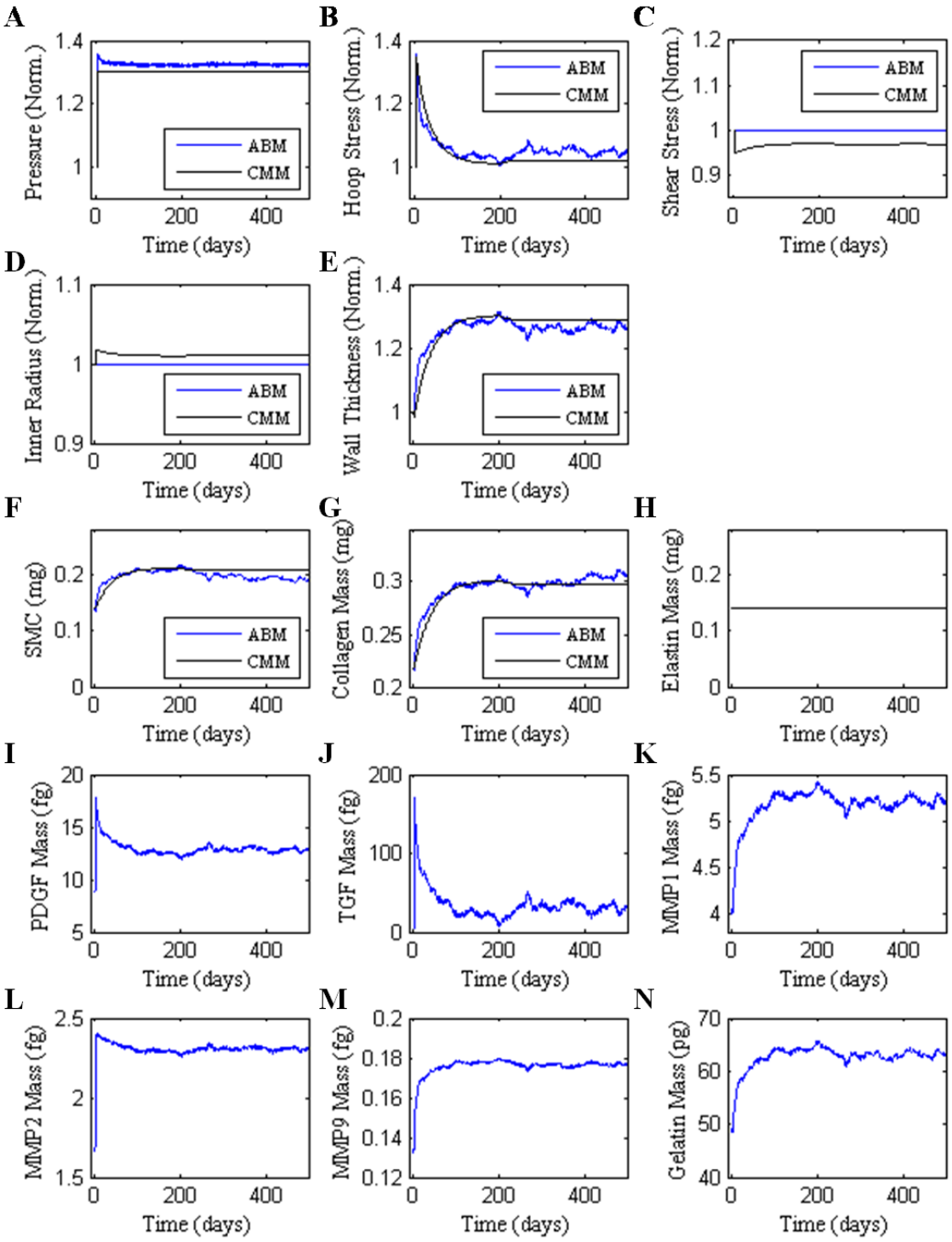

FIGURE 4.5. Illustrative results after implementation of the parameters (see **Table 4.2**) determined through error minimization using the genetic algorithm.

Discussion

Hypertension was chosen as a disease to model due to the relatively consistent geometrical and mechanical observations over time. These findings can be used to verify if the predictions after parameter refinement are correct. When building a theoretical model intended to be applied to predict changes of complex diseases, it is important to first establish model parameters that lead to great predictions in the known case.

Numerous reports indicate that, despite even modest alterations in arterial hemodynamics, significant structural and mechanical changes may occur in attempts to restore circumferential wall stress to its target value. In Goldblatt hypertensive Wistar rats, the circumferential stress did not return to normal until 126 days [97]. Likewise, Wolinsky shows in a series of Goldblatt hypertension studies in rats that wall stress is significantly greater than control at 70 days, but returns to normal by 140 days [124]. The ABM alone, governed primarily by experimental data from cell experiments, predicted a delayed remodeling response wherein hoop stress did not return to within 1% of its target value until day 350. In contrast, the CMM, which is governed primarily by data from tissue-level turnover rates plus stored energy functions for normal structurally significant constituents, predicted a faster remodeling response, returning hoop stress to within 1% of its target value by day 70. After reparameterization, both models recovered within 1% of the target hoop stress value by day 125 [**Fig. 4.5 (B)**], which is closer to that seen experimentally.

In this hypertension simulation, the aortic wall thickened while maintaining nearly constant the inner radius. This result is consistent with previous hypertensive

animal studies looking at the aorta of rats [49, 97, 125-128]. This thickening is likely due to a combination of an imbalanced relationship in both smooth muscle and matrix turnover, that is, increased SMC replication and synthesis leading to increased medial thickness without a counteracting increase in apoptosis or MMPs [129]. Using an aortic coarctation model in rats, Olivetti et al. (1980) [130] and Liu and Fung (1989) [131] observed a 39% increase in wall thickness of the proximal aorta after 8 days. Herein, if we model a similar 50% increase in pressure, the ABM and CMM predict a 2.8% and 8.3% increase, respectively, by day 8. These predictions are much lower than the experimental ones. However, more experimental data needs to be collected in order to deem these predictions inaccurate (see Chapter V).

Hypertension causes increased SMC content. Hu et al. (2008) [132] quantified relative SMC content in the aorta of a hypertensive mini-pig model and similarly found a gradual increase up to 13% by 56 days. The ABM predicts an 8.22% increase in relative SMC content (i.e. SMC mass/mixture mass) from baseline by 56 days; the CMM predicted a 9.25% increase [**Fig. 4.3 (C)**]. Using the parameters obtained from the genetic algorithm both models predict about a 13.6% increase in relative SMC from its baseline value (i.e. 28% of the mixture) [**Fig. 4.5 (F)**]. Therefore, reparameterizing the model brought the predictions closer to the experimental result.

Albeit for the basilar artery, Hu et al. (2007) [96] report a gradual increase in medial collagen from 24.2% (control) to 31.5% by 8 weeks of aortic coarctation induced hypertension in mini-pigs. The ABM and CMM predict an increase in collagen as well although the increase is much less than 30% by 8 weeks. At 8 weeks the relative

collagen mass is only about 3.7% above baseline [**Fig. 4.5 (G)**]. This may be due to differences in artery type/animal type or because Hu et al. (2007) [96] only measured collagen in the media. In contrast to our predictions that collagen increases and then plateaus, others have shown a rapid increase in collagen, peaking at 4 weeks, followed by a decline toward normal by 8 weeks in coarctation models of rabbit and pigs and a Goldblatt model in rats [49, 124]. Albeit not shown herein, depending on the parameters chosen, the CMM and ABM can also predict collagen mass that is not monotonic over time illustrating the versatility of this modeling approach.

Elastin synthesized in arteries during the perinatal period normally remains for much of the lifespan of the animal. Loss of elastin in normal aging results from structural fatigue and degradation [83, 117, 118]. In our simulations, we allowed a constant mechanical contribution of elastin, that is, no degradation or production. A constant mass of elastin does not imply a constant mass fraction, however. Increased accumulation of collagen and smooth muscle decrease the mass fraction of elastin, which has been reported to result from hypertension in pigs over just an 8 week period [132] and in rats from 10 to 20 weeks despite a later (at 70 weeks) return toward normal [49, 124].

To our knowledge, this work presents the first application of an agent based model of arterial wall remodeling in response to hypertension. Biochemical stimulation modulates growth rates, migration, protein expression, and phenotypic morphology of cells. Mechanical stimulation in turn effects the biochemical expression and vice versa. For example, exogenous TGF-β protein augmented wall thickening, likely due to

collagen deposition, in in vivo injured arterial wall models [133-135]. Likewise, a TGF-β antagonist suppressed intimal thickening and collagen deposition in other models [136, 137]. The multiscale model presented here captures these mechanobiological relationships. In addition, TGF- β1 and -3 have been shown to be upregulated by day 1 after sudden onset of hypertension created by a coarctation of the mid-thoracic aorta in rats [128]. Therefore, consistent with our model predictions, TGF-β concentration rapidly increases then drops towards normal by the fourth week following the initiation of hypertension [128].

Limitations associated with data found in the literature include the modest range of shear stress and/ or circumferential stress to which the cells are exposed. The standard physiological range is 0.7 to 1.5 Pa for wall shear stress (WSS) and 100 kPa for circumferential stress (σ_θ). Yet, the mean WSS depends on the animal and type, location, and size of the vessel of interest. For example, the mean WSS in the infrarenal aorta of mice is significantly greater than in humans (8.8 compared to 0.48 Pa, respectively). The average diameter along the aorta for the mouse and human is about 0.07 and 1.3 cm, respectively. Therefore, exposing cultured cells to a presumed standard physiological range of WSS may not be appropriate. In addition, testing and acquiring too few data points for a mechanical dose response curve is not a good representation of the complete response. As more literature finding become available, in particular with respect to half-lives and removal rates of soluble factors, the ABM can readily integrate these findings.

In conclusion, we presented in the last 2 chapters an ABM and CMM each with their own advantages and disadvantages. The ABM has an advantage in that it directly

accounts for literary findings describing cell behavior, and stochastic variability in the apoptosis and proliferation rates. An advantage of the CMM is that it accounts for the specific strain-energy density relationships of the structurally significant-constituents in the artery. In addition, the mass production and removal of these constituents is based on shear stress, Cauchy stress, constrictor/dilator concentration, half-life and tension. A disadvantage of the ABM is that it lacks a strong mechanical framework. Whereas a disadvantage of the CMM is it assumes axisymmetry and doesn't account for specific biological responses. Therefore, the natural model evolution would be to couple the ABM and CMM in order to create a multi-scale model. That is one could use the ABM to calculate biochemical molecules that would then be implemented into the mass production and removal functions in the CMM at each time step. The CMM in turn could calculate stress, loads and geometry that would be feed into the ABM. This cycle would continue until the desired time or stable condition is reached. In the future it is conceivable constitutive equations in the CMM, which depend on the ABM, can be implemented into finite element modeling to simulate a more accurate 3-dimensional artery.

CHAPTER V

HYPERTENSION – EXPERIMENTAL FINDINGS

Overview

Hypertension often manifests primarily as a thickened arterial media and, to a lesser degree, thickened intima and adventitia. Less is known, however, regarding the evolution of such changes in different arteries and the different underlying structural changes. Herein, we use a porcine coarctation model of hypertension in attempt to elucidate structural changes temporally and spatially in three different arterial beds. Firstly, we quantify the number of cells per wall area to determine whether the increase in mass is due primarily to hypertrophy or hyperplasia. Also, by determining the area fraction per wall of smooth muscle actin, the main protein component making up the contractile apparatus of cells, we will further help to characterize the overall vasoactive capacity. Through quantification of collagen fibers we can infer their contribution to overall wall stiffening. Finally, possible involvement of circulating systemic cells is addressed by identifying hematopoietic cells and macrophages, the latter of which may contribute to matrix turnover via the production of proteinases.

Introduction

Hypertension, defined as a persistent elevation of blood pressure, affects over 50 million Americans and is a significant risk factor for many diseases, including abdominal aortic aneurysms, aortic dissections, atherosclerosis, cerebral vasospasm, end stage renal failure, heart failure, intracranial aneurysms, stroke, and so forth. Hypertension is caused by and causes significant remodeling of arteries and arterioles,

which includes phenotypic changes of vascular cells and associated changes in extracellular matrix, often leading to an overall increased stiffness of the vessel. Indeed, mounting evidence suggests further that stiffening of central arteries (i.e., aorta and carotids) may be both an initiator and an early indicator of subsequent cardiovascular risk, particularly for low resistance organs such as the heart, brain, and kidneys [138-142]. The ratio of collagen to elastin normally increases with distance from the heart, but this ratio can be exaggerated in hypertension. Because mature fibrillar collagen is stiffer than elastin, primarily resisting arterial distension at high systolic blood pressures, an increase in collagen can also contribute to increased arterial stiffness [143-145]. The goal of this work, therefore, was to contrast progressive histological changes in the proximal aorta as well as coronary and cerebral arteries to elucidate possible differences in the type, extent, and time course of arterial remodeling in an established mechanically induced animal model of hypertension.

Methods

Animal Model. All animal protocols were approved by the Institutional Animal Care and Use Committee at Texas A&M University. Arterial specimens were excised from adult mini-pigs before or at prescribed time-points following the surgical creation of a supra-diaphragmatic aortic coarctation that induced hypertensive conditions in the vessels of interest (see [17]). Briefly, a balloon-inflatable silicone occluder (In vivo Metrics, Inc; reinforced by Soloman Scientific), prefilled with a 50% dextrose solution, was placed over a Gore-Tex patch that was wrapped around the supra-diaphragmatic aorta, between intercostal vessels, and secured with suture. The occluder was connected

via stiff tubing to a vascular access port placed subcutaneously in the neck, which allowed it to be inflated or deflated within the conscious animal based directly on desired changes in blood pressure that were measured via an indwelling transducer placed within either the internal thoracic artery or the right carotid artery. Arterial pressure and heart rate were recorded for 30 seconds every 2 hours throughout the study.

Beginning approximately 1 week after surgery, the aorta was coarcted gradually by adding small amounts of dextrose to the occluder over a 7 to 10 day period until the daily average mean arterial pressure (MAP) reached or exceeded 150 mmHg. Data were collected from 41 mature (7 to 16 month old) male mini-pigs (Sinclair Research Center, Inc, Columbia, Mo): 16 normotensive (NT) controls and 25 hypertensive (HT) animals [**Table 5.1**]. Specifically, arteries were harvested from true controls (n = 2), from surgery controls (n = 3) without an occluder, from NT animals at 2 (n = 2), 4 (n = 4), 6 (n = 3), and 8 (n = 2) weeks following a sham surgery wherein an occluder was implanted but not inflated, and from HT animals at 2 (n = 7), 4 (n = 7), 6 (n = 5), and 8 (n = 6) weeks after the animal reached its target mean arterial pressure (>150 mmHg). Notwithstanding increases in pressure over time during hypertension (**Table 5.1**), the overall averaged MAPs were 131 ± 6 mmHg in NT and 168 ± 17 mmHg in HT animals, which were significantly different (one-way ANOVA, $p < 0.001$); the overall averaged pulse pressures were 37 ± 6 mmHg in NT and 53 ± 10 mmHg in HT animals, which were also significantly different (one-way ANOVA, $p < 0.001$).

TABLE 5.1. Averaged number, mean arterial pressure, and pulse pressure of pigs at each time step after induced hypertension.

Condition	Number of Pigs	MAP Averaged over the last 2 wks (mmHg)	Pulse Pressure Averaged over the last 2 wks (mmHg)
NT	16	131 ± 6	37 ± 6
2 wk HT	7	152 ± 6	48 ± 6
4 wk HT	7	171 ± 11	56 ± 12
6 wk HT	5	171 ± 14	55 ± 5
8 wk HT	6	181 ± 20	55 ± 12

Note: NT denotes normotensive and HT denotes hypertensive. MAP is mean arterial pressure.

Histology and Immunohistochemistry. Immediately following exsanguination, segments of descending thoracic aorta 3+ cm proximal to the occluder (P-Ao) as well as segments of the left anterior descending (LAD) coronary artery and the middle cerebral artery (MCA) were dissected free of perivascular tissue and fixed at unloaded conditions by immersion in fresh 4% paraformaldehyde for one hour. Specimens were then embedded in paraffin, sectioned at 5 μm, photobleached, deparaffinized, rehydrated, and stained for either standard histology or immunohistochemistry. Prior to immunostaining, slides were further placed in a local greenhouse for 5 days to reduce auto-fluorescence of endogenous fluorophores, primarily from elastin and collagen (see [146, 147] for details). Sections were stained with Verhoeff-van Gieson (VVG) for elastin (Verhoeff) and collagen (van Gieson), and with antibodies against alpha smooth muscle actin (αSMA) for contractile cells, von Willebrand factor (vWF) for endothelial cells of the cerebral

arteries, MAC387 for leukocytes, and CD34 for hematopoietic progenitor stem cells. Antibodies and the determined optimal dilutions are detailed in **Table 5.2**.

TABLE 5.2. Primary, secondary, and tertiary antibodies and treatment specifications for immunostaining of porcine arteries.

Primary (clonality)	Vendor (code)	Concentration and Time	**Secondary**	Vendor (code)	Concentration and Time	**Tertiary**	Vendor (code)	Concentration and Time
aSMA (P)	Abcam (ab5694)	2 µg/ml; RT 60 min	Alexa 594	Invitrogen (A11012)	4 µg/ml; RT 60 min			
L1 protein (M: MAC387)	Abcam (ab22506)	20 µg/ml; 4 °C overnight	Alexa 488	Invitrogen (A11054)	10 µg/ml; RT 60 min	Alexa 488	Invitrogen (A11054)	10 µg/ml; RT 60 min
CD34 (M: MEC 14.7)	Abcam (ab8158)	2 µg/ml; 4 °C overnight	Alexa 594	Invitrogen (A21211)	4 µg/ml; RT 60 min	Alexa 594	Invitrogen (A11012)	4 µg/ml; RT 60 min
vWF (P)	Abcam (ab6994)	80 µg/ml; RT 60 min	Alexa 594	Invitrogen (A11012)	4 µg/ml; RT 60 min			

Note: P denotes polyclonal, M denotes monoclonal, Alexa denotes Alexa Fluor®

Indirect immunofluorescent staining was performed following the Abcam double immunofluorescence protocol with slight modifications [148]. Optimal antigen retrieval method was found to be heat-induced epitope retrieval (using a pressure cooker) for 3 minutes with sodium citrate retrieval buffer at pH 6 for all antibodies. Sections with intracellular target protein sites (i.e., αSMA, SM-MHC, vWF, and MAC387) were permeabilized with 0.25% Triton X-100 in PBS for 10 minutes. Subsequently, slides were incubated in 10% goat serum for 30 minutes to prevent non-specific binding of antibodies. Slides were incubated with the primary antibody, washed 3x for 5 minutes in PBS, and incubated with their fluorescent secondary antibodies (see **Table 5.2**). Slides

were then either incubated for 30 minutes with fluorescent tertiary antibodies for greater fluorescence, as in the case of the low-abundance target proteins MAC387 and CD34, or washed 3x for 5 minutes in PBS and counter-stained with premixed DAPI mounting medium (ProLong® Gold antifade reagent with DAPI, Invitrogen (P-36931)). After tertiary incubation for MAC387 and CD34, the sections were mounted with the premixed DAPI medium and cover-slipped for imaging. All experiments were preformed with a negative control (i.e., primary antibody substitution with PBS) to determine background fluorescence. A negative isotype control (rabbit IgG, Vector Laboratories (I-1000)) was also used to confirm specific staining.

Image Acquisition and Quantification. Arterial samples were imaged using an Olympus BX/51 fluorescence microscope coupled with an Olympus DP70 digital camera. This microscope is equipped with diascopic (transmitted) and episcopic (reflective) optical pathways to capture bright-field and dark-field images; it is also customized for circularly polarized illumination [9] to capture polarized light images. Köhler illumination was established and settings for microscopic illumination, exposure times, and color balance of the digital camera were maintained for each set of slides to enable subsequent comparisons. For dark-field images, settings were found by zeroing out the fluorescence of the same artery-type negative control (i.e. processed exactly the same except without the primary antibody) for each batch of staining.

For quantitative morphological analysis, an appropriate objective was used to acquire an image of the entire artery (i.e., dissection microscope for P-Ao, 20X for LAD, and 40X for MCA) and at least two representative color images of the arterial wall (i.e.,

4X for P-Ao, 4X for LAD, and 20X for MCA) per specimen. In some cases, images were acquired at a higher magnification for better visualization. Image files were saved in tagged-image file format (TIFF). GIMPshop 2.2.8 was used to overlay fluorescent images taken with different filters (i.e. Fitc, Tritc, PI).

A "detail analysis" method was used to determine, for each type of artery, the following: (1) inner and outer radius (using the circle and hydraulic diameter formulae), (2) mean wall thickness, (3) mean thickness of intima, media and adventitia, (4) area fraction of positive SMA stain in the wall, (5) area fraction of collagen in the wall, (6) area fraction of elastin in the wall, (7) nuclei count per wall area, (8) number of hematopoietic cells, (9) number of macrophages, and (10) endothelial cells in the cerebral arteries.

To quantify mean inner and outer radius as well as wall thickness for 3 different types of arteries in all 41 pigs we stained the arteries with either VVG or PSR and captured an image of the whole arterial ring. The outer diameter of the P-Ao was larger than 7 mm, therefore a dissection microscope was used to capture the whole artery. In addition, the peri-vascular tissue was removed from the P-Ao before staining. For the LAD and MCA arteries, we manually cropped the myocardium and connective tissue from the adventitia using ImageJ and GIMPshop. The luminal boarder was detected using magic wand in GIMPshop, and the lumen was filled black for better image recognition. An image analysis program was written in MATLAB 7.9.0 (R2009b) to calculate the luminal and wall area as well as the luminal and outer adventitial perimeter [**Fig. 5.1**].

The area of a circle and circumference as well as hydraulic diameter formulae were used to calculate radius and thickness for each vessel.

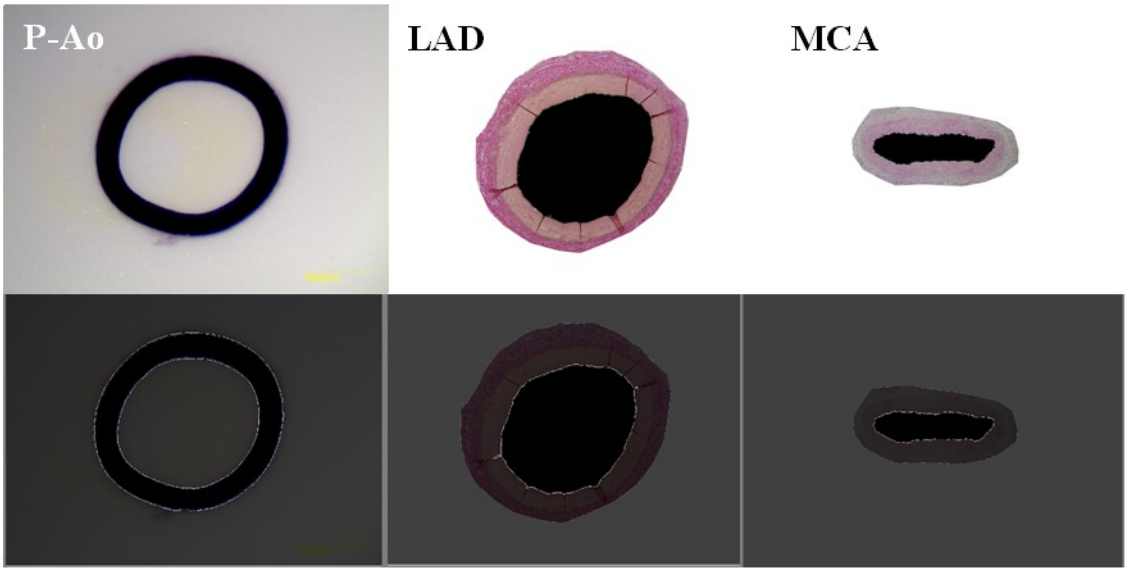

FIGURE 5.1. The first row shows original images of the proximal aorta (P-Ao), left anterior descending artery (LAD), and middle cerebral artery (MCA). The LAD and MCA were cropped of connective tissue. A custom computer algorithm was then used to identify the region of interest and delineate the inner and outer boundaries.

To verify the thickness calculations, another image was taken at greater magnification of just the arterial wall. The connective tissue was cropped from the adventitia in the cases of the LAD and MCA. To obtain layer thickness, the intima and/or media were cropped separately [**Fig. 5.2**]. The region of interest was found using a color threshold module and refined using a median filter (to remove small particles). The mean thickness was then calculated by dividing the total area (pixels^2) by the image width (pixels) and then using the scale bar to convert to metric units. That is, for an image with

dimensions m x n, where m is the width and n is the height, the mean thickness is defined as $\overline{thickness} = \sum_{i=1}^{m} n_i^{wall}/m$, where, n_i^{wall} is the thickness of the wall at each pixel (i) along the width. For the LAD and MCA, medial thickness was determined by subtracting the adventitia. Similarly, the intimal thickness was found by subtracting the media and adventitia from the total.

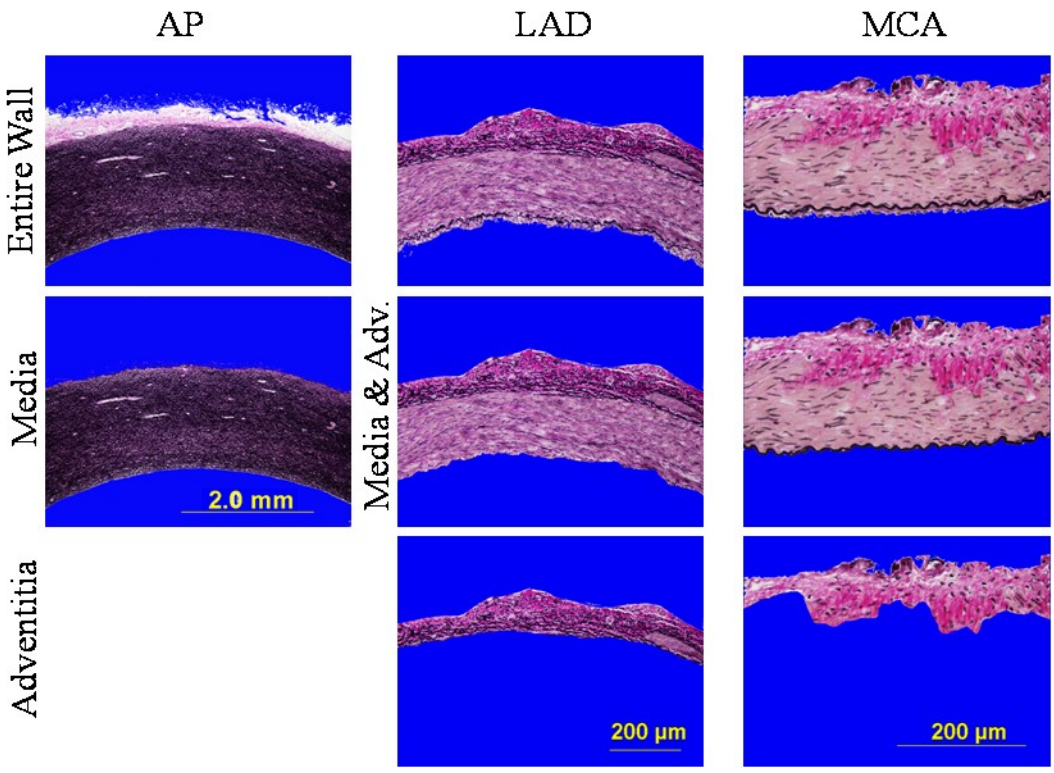

FIGURE 5.2. Mean wall thickness for each layer (i.e., intima, media and adventitia) was found based off the cropped images delineating the separation for each layer. This was done for all artery types (P-Ao, LAD, MCA) under all conditions (surgery controls, normotensive controls, 2 wk, 4 wk, 6 wk, and 8 wk hypertensive).

To get the area fraction of positive fluorescence we first cropped the lumen and connective tissue, then filled the wall with white for easy recognition. Then we

converted the image into a grayscale images for each channel (red, green, blue), with pixel values ranging from 0-255 depending on the intensity of a specific color [**Fig. 5.4**]. First we determined the proper threshold value $\in [0, 255]$ to convert the red, green or blue channel images into a binary image. To do this, we subtracted the total color-specific intensities in the arterial wall from the color-specific intensities in negative control images [**Fig. 5.3**]. The threshold cut-off was set to be the minimum value for the last bin in the resulting mode [**Fig. 5.3 (C)**]. This was done for each set of images as a batch process (divided based on the microscope objected used and the stain), thereby ensuring specific positive staining with minimal background or observer bias. The total pixels identified according to the stain were then divided by the total pixels making up the artery wall to give us the area fraction of positive stain in the wall section.

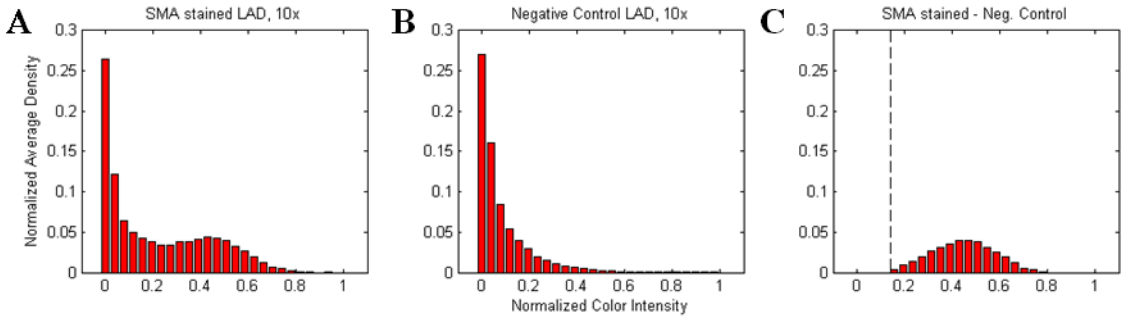

FIGURE 5.3. For each fluorescently stained set of images, the proper threshold was determined. This was done by using batch processing to get the normalized average density for all images taken by a certain objective, for a certain stain and a certain artery type (e.g. 10x objective, SMA stained, LAD arteries). The resulting bar plot (**A**) was then subtracted from a bar plot of the negative control images (**B**) to give a bar plot of the true stain intensity range (**C**). Therefore the threshold to convert an image to a binary image was determined (dashed line in (**C**)). The abscissa was normalized out of 255.

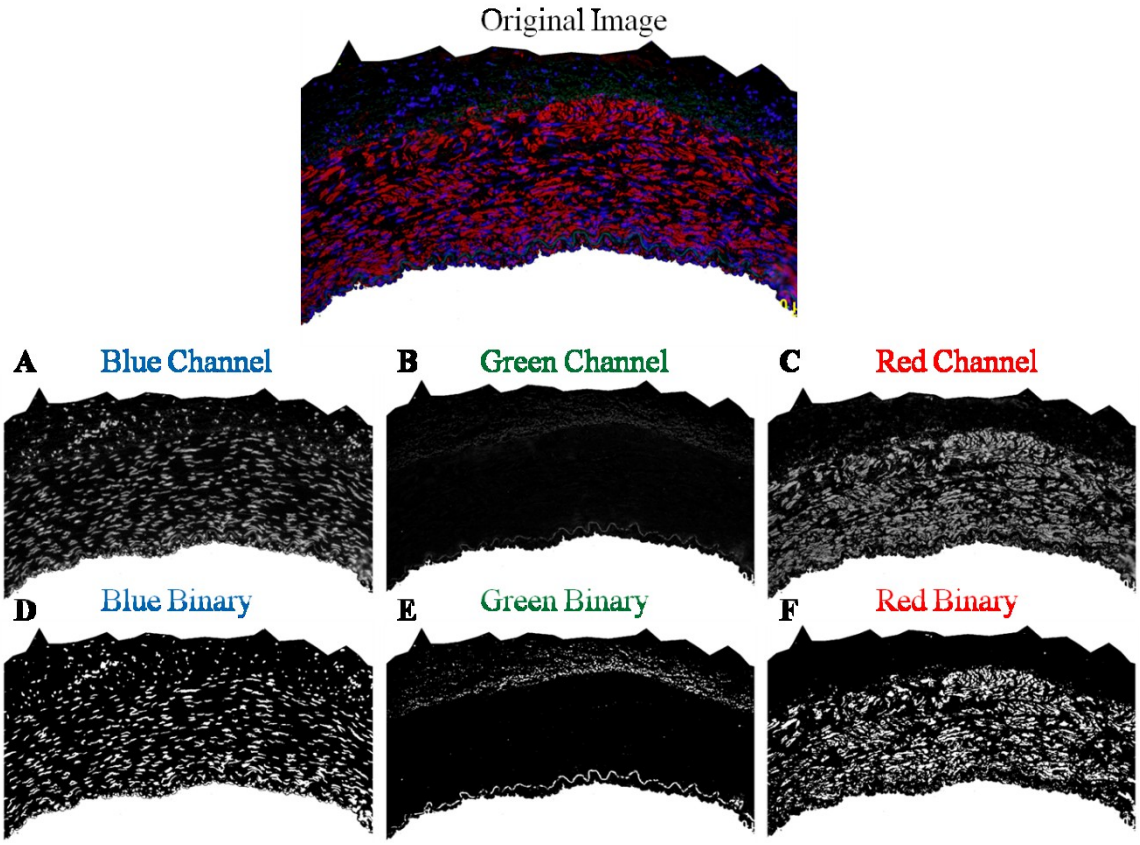

FIGURE 5.4. (**A, B, C**) After manual cropping, each image was converted to a grayscale image according to the desired color channel (i.e., blue for nuclei, green for elastin, or red for SMA). (**D, E, F**) A predetermined threshold value [see **Fig. 5.3**] was used to convert the gray scale image to a binary (i.e., black and white) image. Shown here is a 2 week hypertensive LAD.

Autofluorescence was not an accurate measure for elastin in all cases. This is due to the fact that we placed the samples in a greenhouse for 5 days to reduce the autofluorescence. In addition, for the large aortic samples we had to use a 4x objective and thus lost a lot of the autofluorescent signal. Therefore, a custom routine was created in MATLAB (R2009b) that would analyze the samples stained for elastin using VVG.

The VVG stain also stains nuclei in some cases [**Fig. 5.5**]. Therefore, the program was created to have an adaptable threshold designating the minimum size a blob has to be.

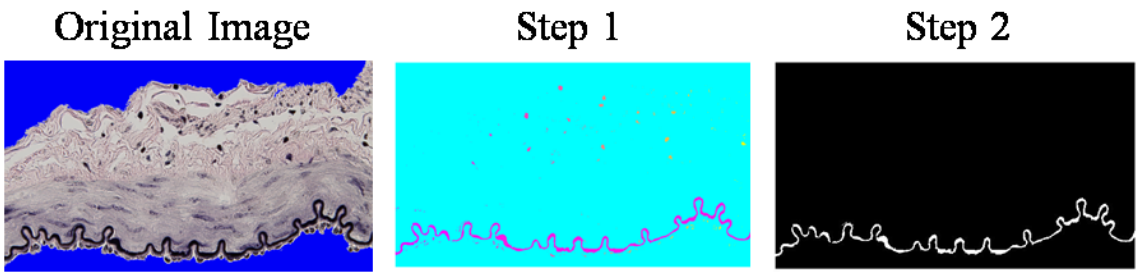

FIGURE 5.5. Algorithm created to determine the area fraction of elastin in the wall. First a threshold was used to determine the "black" elastin. Second a threshold was added to remove the black nuclei blobs. Then the ratio of elastin pixels to wall pixels (non-blue portion) was determined.

The area fraction of total fibrillar collagen in the arterial wall was quantified similarly from Picro-sirius red birefringent images. Briefly, a brightfield image was used to determine the region of interest and a darkfield image to determine the collagen (birefringence), with anything not black by a threshold level considered to be collagen. The collagen area (in pixels) was then divided by the total wall area (in pixels) to get the ratio of collagen in the wall.

Finally, the total number of cells was determined by a custom program for nuclei written in MATLAB, Version 7.9.0.259 (R2009b) [**Fig. 5.6 (A)**]. The centroid of each nucleus was identified according to minimum size, separation, and intensity [**Fig. 5.6 (B)**]. In addition, the inner and outer boundaries were found based on orientation and color threshold (since the extravascular areas were cropped to white). The number of

nuclei relative to wall position, with 0 being the luminal boundary and 1 being the adventitial boundary, was then plotted [**Fig. 5.6 (C)**]. The smaller number of hematopoietic and macrophages were manually counted and scored.

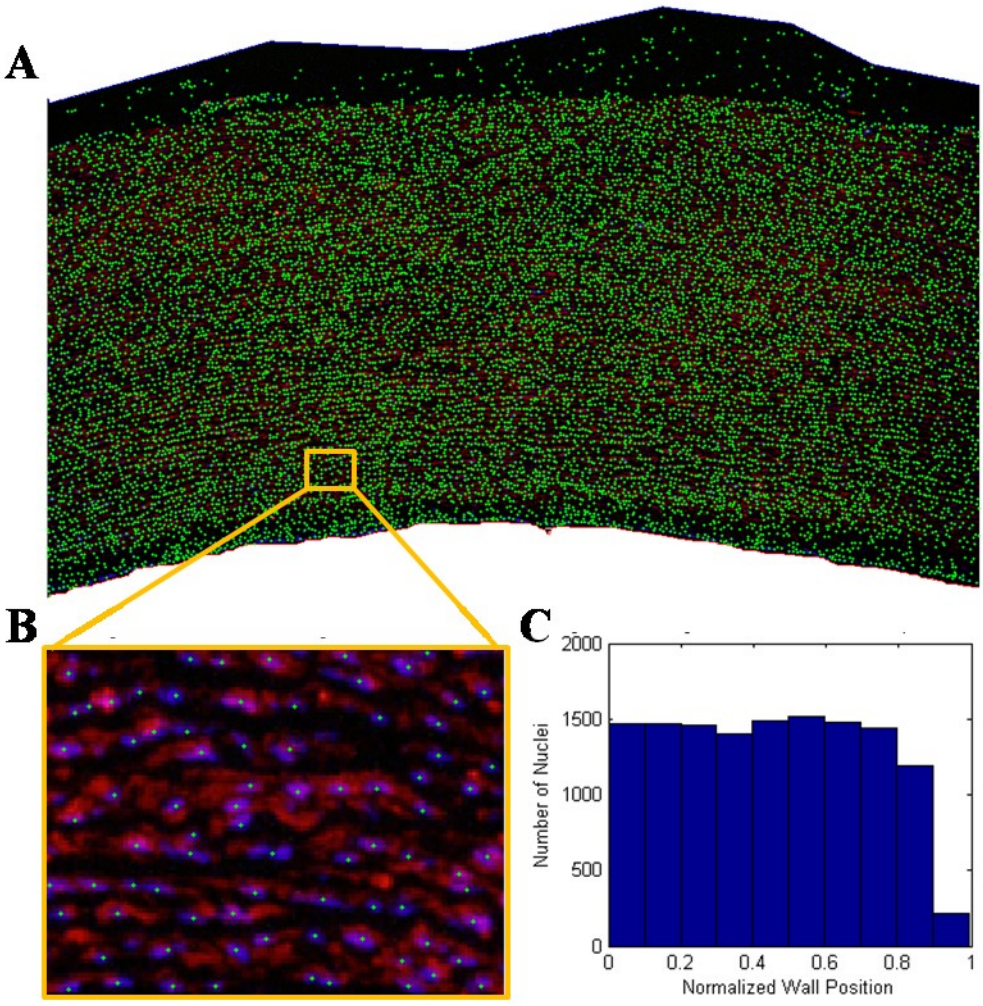

FIGURE 5.6. (A) Each arterial wall section was cropped of extravascular areas (white), the inner and outer boarders were determined, and the centroid of nuclei was identified (green astric). (**B**) Zoomed in section of the wall shows good nuclei detection. (**C**) The number of nuclei as a function of wall position (where 0 is the lumen and 1 is the outer adventitia boarder) was determined for each image.

Results

Sustained mean arterial pressure above 150 mmHg led to significant alterations in the arterial geometry of the P-Ao, LAD and MCA. The inner radius of the P-Ao and MCA arteries did not significantly increase or decrease after 2, 4, 6, or 8 weeks of hypertension [**Fig. 5.7 (A, C)**]. However, the LAD increased in caliber 50%, 51%, 17% and 61% at weeks 2, 4, 6 and 8, respectively, compared to the normotensive controls. In addition, significant wall thickening was observed in the LAD and P-Ao after increased mean pressure for 2, 4, 6, and weeks [**Fig. 5.8**]. The mean aortic wall thickness, as calculated based on the measured area of the entire ring, significantly increased by 56% compared to the normotensive controls after only 2 weeks. The wall was 64% thicker after 8 weeks. Due to the size of the P-Ao (over 12 mm in outer diameter) a dissection microscope was used to capture the entire cross-section. Because details may have been lost in doing so, at least 2 images of the aortic wall were taken at higher magnification. The mean wall thickness, as measured from the wall segment at higher resolution, still shows a significant increase at week 2 (40%) from baseline, and 61% by week 8. The increase in thickness was even more drastic in the LAD. The measured mean wall thickness increased 220% fold by the second week. The LAD continued to increase in mass as observed in the week 4 results (250%). However, at week 6, the wall thickness decreased to 80% increase over the normal value, but increased again by week 8 to 242% over normal. The same trend, but slightly less drastic, was also observed using the thickness value calculated from the images viewing the entire artery. Moreover, the inner radius of the LAD followed this pattern [**Fig. 5.7 (B)**]. The MCA did not

significantly increase or decrease in wall thickness at any time during hypertension [**Fig. 5.8 (C)**].

Mean thickness distributions for each layer (i.e. adventitia, media, and intima) were quantified for each artery type and condition. Thickening of the P-Ao was attributable almost entirely to the media and intimal layers [**Fig. 5.9 (A)**]. In contrast, the LAD thickened most in the adventitial layer, exhibiting a 3-fold increase in thickness after only 2 weeks [**Fig. 5.9 (B)**]. By 4 weeks, the medial and intimal layers had increased in thickness 2.2- and 2.5-fold respectively; the adventitial layer was still 2.5-fold thicker than the normotensive controls [**Fig. 5.9 (B)**]. Although the overall wall thickness of MCAs did not change, the distribution of mass shifted from the intima to the media while the adventitia remained nearly the same. **Figure 5.9** (**C**) shows that the intima went from 30-micrometers to 5-micrometers after 8 weeks. Conversely, the media increased from a thickness of 53-micrometers to 86-micrometers after 8 weeks.

Despite significant changes in wall thickness in the P-Ao and LAD, cell density (i.e. cells per square micrometer) remained fairly constant. **Figure 5.10** illustrates the cell density for each artery type over the 8 week hypertensive period. Note, however, the

density of cells in the wall is different depending on the artery type. For example, the starting densities were 0.000127, 0.00378, and 0.005497 cells/μm^2 for the P-Ao, LAD and MCA respectively. Note this order is inversely parallel to the amount of elastin in these arteries. An unknown but statistically significant 15% decrease in cell density is observed at week 6 in the MCA, which is recovered by week 8.

The number of nuclei as a function of radial position from the lumen to the outer adventitial border was quantified. Strikingly the P-Ao and LAD maintained similar trends throughout the G&R time course [**Fig. 5.11 (A, B)**]. Although the MCA changed the least, in regards to geometry, cell phenotypic changes, and matrix production/removal, the proportion of nuclei with respect to position and time shifts the most [**Fig. 5.11 (C)**]. Similar to all artery types, the density was highest in arterial tissue within 10% of the lumen. In the P-Ao the cell count maintained fairly constant until the outer fourth of the vessel (presumably the adventitia) [**Fig. 5.11 (A)**]. For the LAD and MCA, the cell count tends to gradually decrease antegrade from the lumen [**Fig. 5.11 (B, C**].

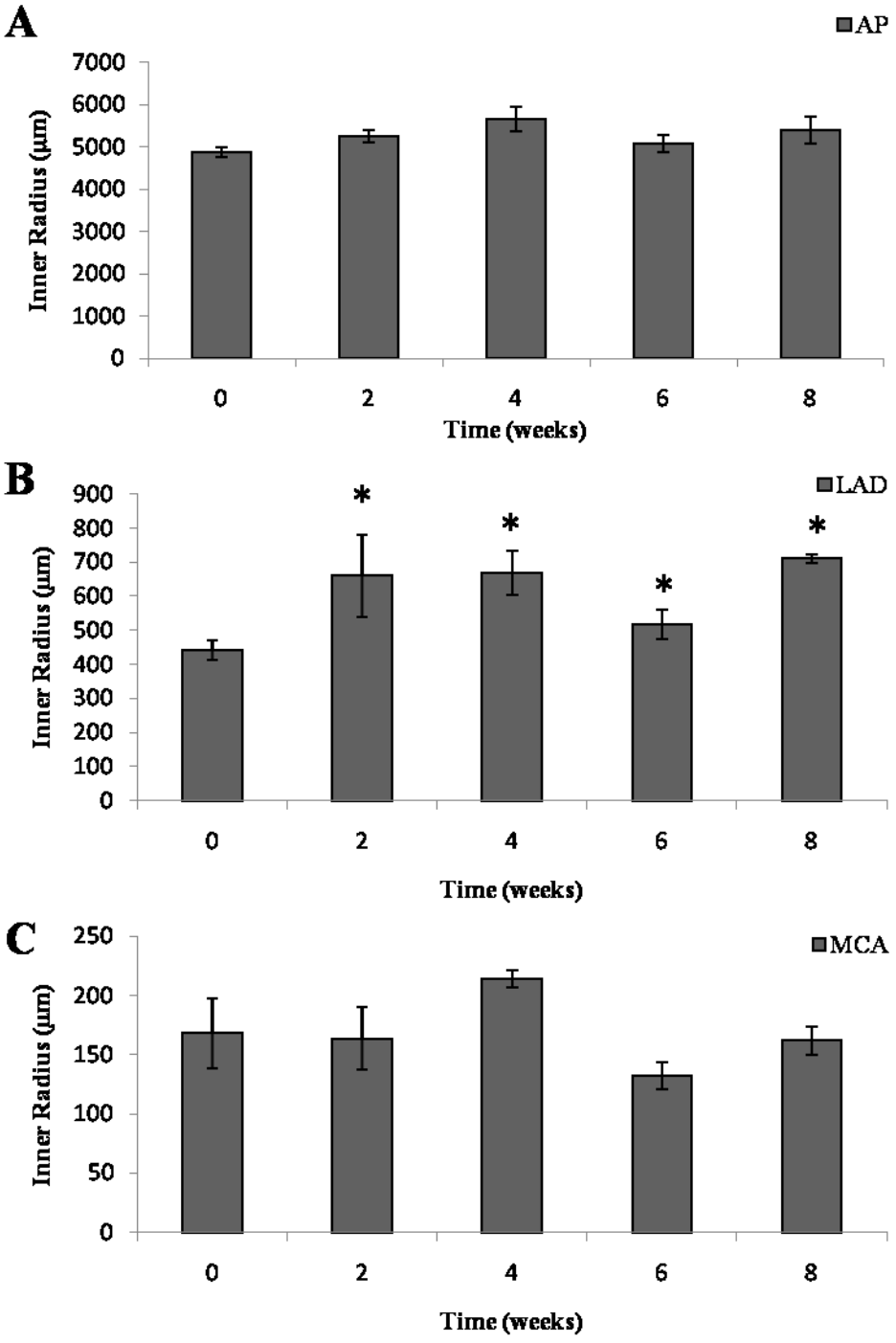

FIGURE 5.7. Inner radius of control (week 0) and hypertensive arteries (weeks 2, 4, 6, and 8) Mean ± SEM. The inner radius was calculated using the circle formula based on the wall area calculated from images showing the entire artery. * $p < 0.05$, unequal two sample t-test

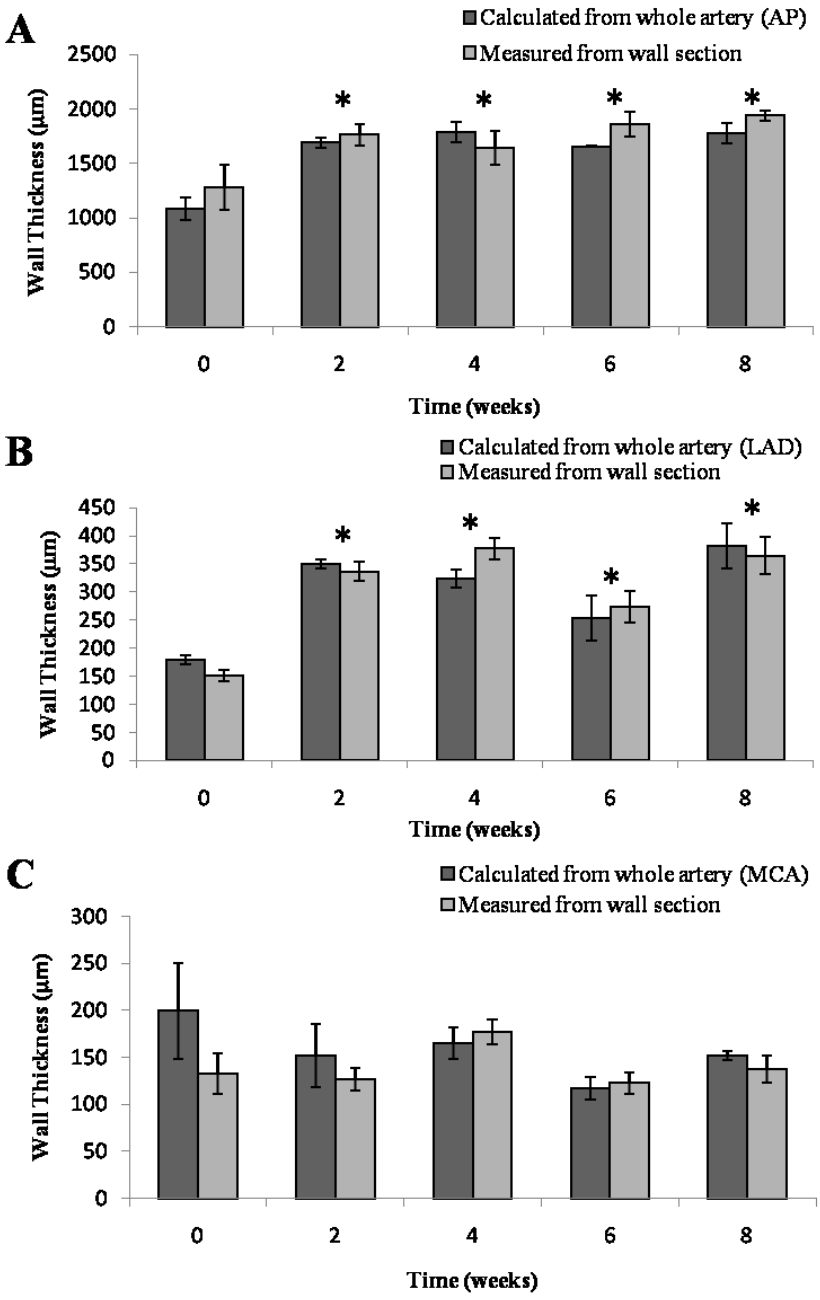

FIGURE 5.8. Mean wall thickness from the P-Ao [**A**], LAD [**B**], and MCA [**C**] after sustained hypertensive conditions for 0, 2, 4, 6, and 8 weeks Mean ± SEM. Wall thickness was calculated using, $h = \sqrt{A_{v+l}/\pi} - \sqrt{A_l/\pi}$, where A = area, v = vessel and l = lumen, from whole arterial rings as well as measured from higher resolution images of a section of the wall. [**A, B**] The P-Ao and LAD significantly increased in wall thickness compared to the control. [**C**] The MCA did not show any statistically significant change in thickness over the 8 weeks. * $p < 0.05$, unequal two sample t-test

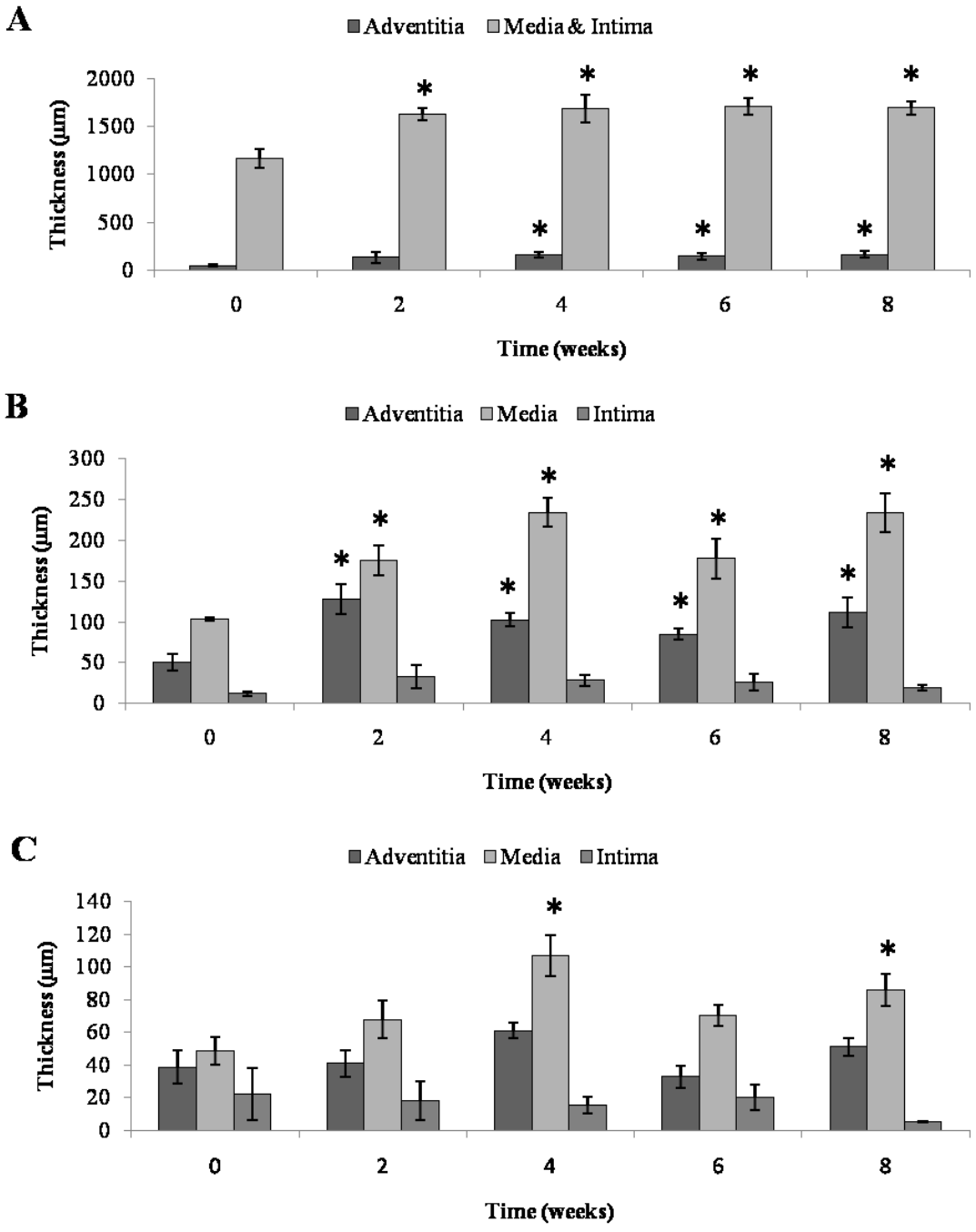

FIGURE 5.9. Mean thickness distribution of the adventitia, media and intima in the (**A**) P-Ao, (**B**) LAD and (**C**) MCA Mean ± SEM. (**A**) The P-Ao significantly thickens in the adventitia, media and intima. (**B**) The LAD significantly thickens in both the media and adventitia after 2 weeks. (**C**) The distribution of mass is shifted to the media in the MCA, although only significantly at week 4 and 6. * $p < 0.05$, unequal two sample t-test

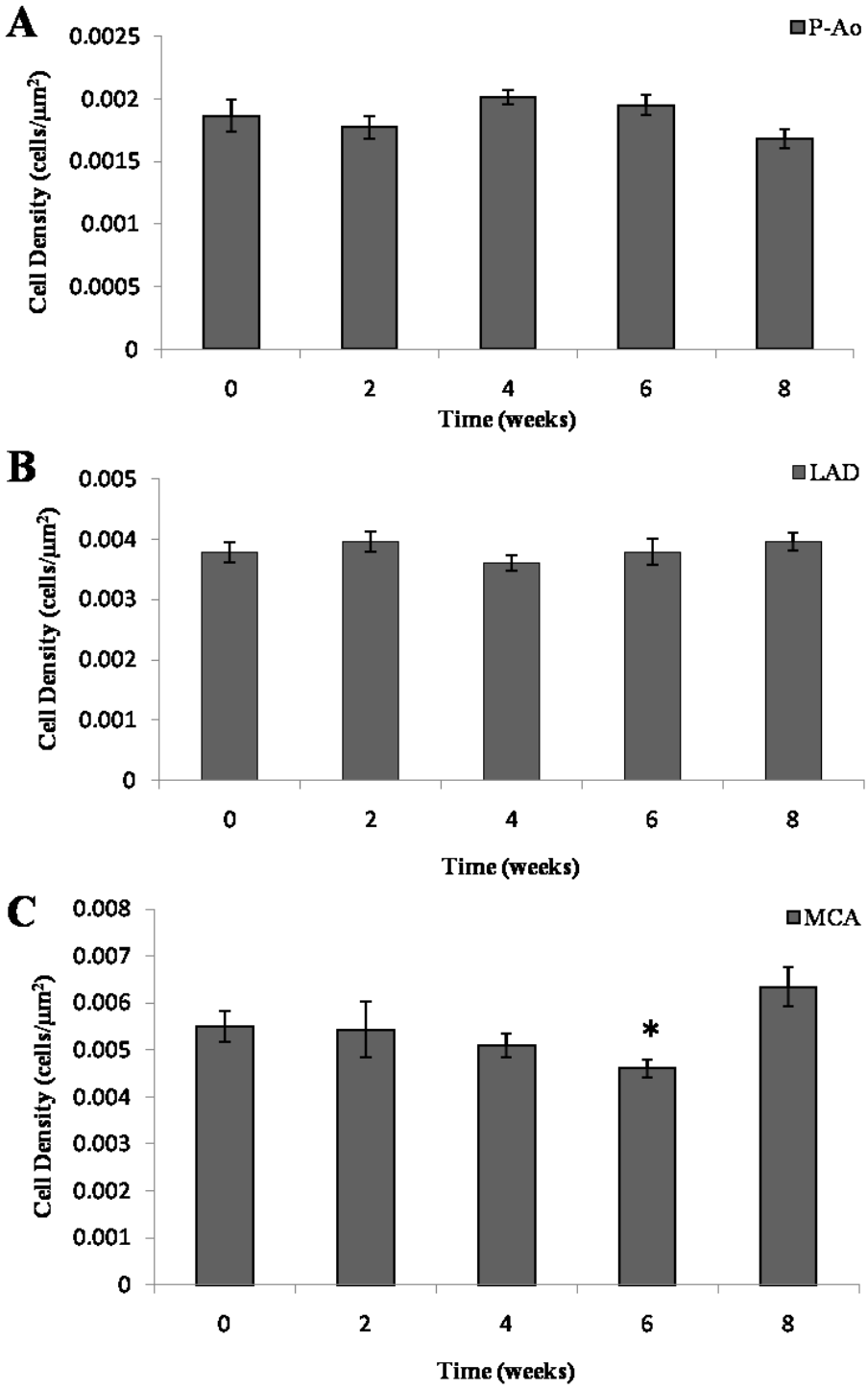

FIGURE 5.10. (**A, B, C**) Cell density of the wall of the P-Ao, LAD and MCA as a function of time Mean ± SEM. (**C**) The cell density decreases slightly, but significantly in the MCA at week 6, and is recovered by week 8. * $p < 0.05$, unequal two sample t-test

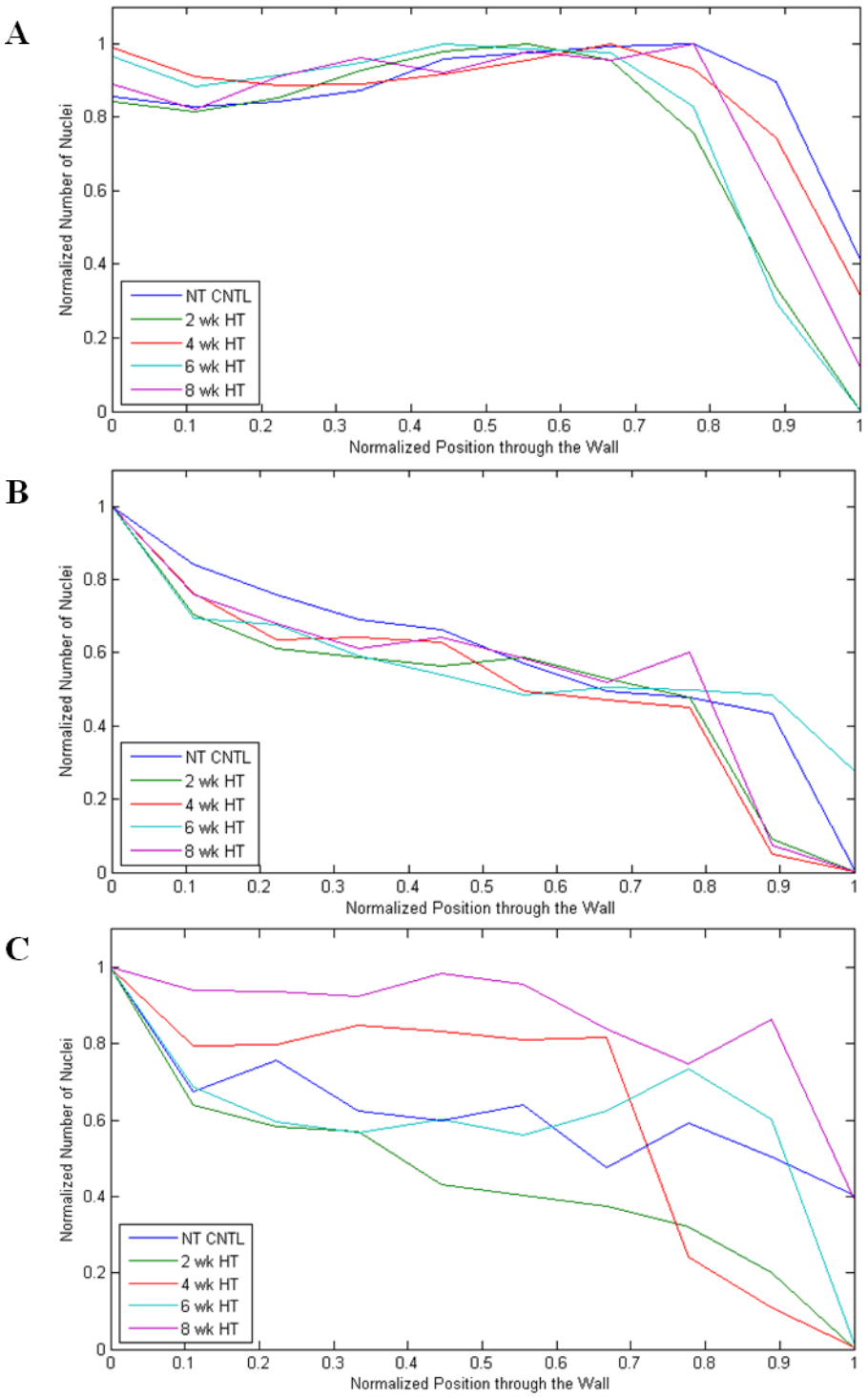

FIGURE 5.11. Normalized number of nuclei as a function through the arterial wall for each artery type ((**A**) P-Ao, (**B**) LAD, (**C**) MCA) at each experimental time point (NT control, and 2, 4, 6 and 8 week HT).

PSR birefringent staining was used to identify and quantify fibrillar collagen content in the arterial wall. The basal value of collagen in the P-Ao constitutes about 9.5% of the arterial wall [**Fig. 5.12 (A)**]. At 2 weeks of hypertension, collagen was not significantly different. However, at 4 weeks collagen significantly increased in the P-Ao by 2.9-fold. Although, slightly decreased at 6 weeks, at 8 weeks collagen in the P-Ao was 3.3-fold higher than the basal value. Unlike the P-Ao, collagen did not significantly increase or decrease over the 8 week period in the LAD or MCA [**Fig. 5.12 (B, C)**].

Smooth muscle actin (SMA) is typically used as a marker of smooth muscle cells, particularly those exhibiting a contractile or vasoactive phenotype. Two weeks after hypertension was induced in the pigs, the percent of SMA decreased significantly by 31% in the P-Ao [**Fig. 5.13 (A)**], after which overall cell contractility slowly increased; by week 8 there was 6% more SMA than in the normotensive arteries (albeit not statistically significant). This pattern was also seen in the MCA [**Fig. 5.13 (C)**], except that SMA decreased initially by 20% and did not start increasing again until week 6. At 2 weeks, the LAD exhibited the opposite effect [**Fig. 5.13 (B)**]: there was an increase overall wall contractility. From 4 to 8 weeks the percent of SMA in the LAD leveled off at 41%.

Under healthy conditions, arterial elastin is thought to be minimally produced or removed past the neonatal period [83, 116-118]. Herein, the environmental conditions are altered for up to 8 weeks and the relative content of arterial elastin does not stay the same in all arteries. The P-Ao, a naturally elastic artery, shows a gradual yet insignificant increase in elastin after the second week. At week 8 the elastin percent in

the wall is significantly higher than the control by 43% [**Fig. 5.14 (A)**]. Elastin did not significantly change in the LAD except at week 4. At week 4, elastin content in the LAD wall was 67.9% greater than the control; elastin was increased primarily in the media in concentric layers. In a normal healthy LAD elastin is typically not present in the medial layer. In the MCA elastin did not significantly increase or decrease. In both the LAD and MCA the IEL became straighter.

In addition to matrix alteration and phenotypic changes, circulating blood cells also play a role in arterial remodeling due to elevated blood pressure. Progenitor cells are present in native arteries [149-151]. Throughout the G&R time course, the amount of CD34 stain in the arterial walls of P-Ao did not change significantly from that of the control [**Fig. 5.15 (A, B)**]. However, the percent of CD34 in the MCA significantly increased 2.5 fold by week 4 and remained elevated [**Fig. 5.15 (C)**]. Unlike the progenitor cells, accentually zero macrophages were present in the control arteries. Macrophages were not observed in any of the MCA arteries after the onset of hypertension as well. However, in the P-Ao and LAD, a significant increase in MAC387 was observed at week 2 [**Fig. 5.16 (A, B)**]. In both artery types the relative macrophage content decreased by 4 week. Unique to the LAD, macrophage content was statistically elevated by week 8 [**Fig. 5.16 (C)**].

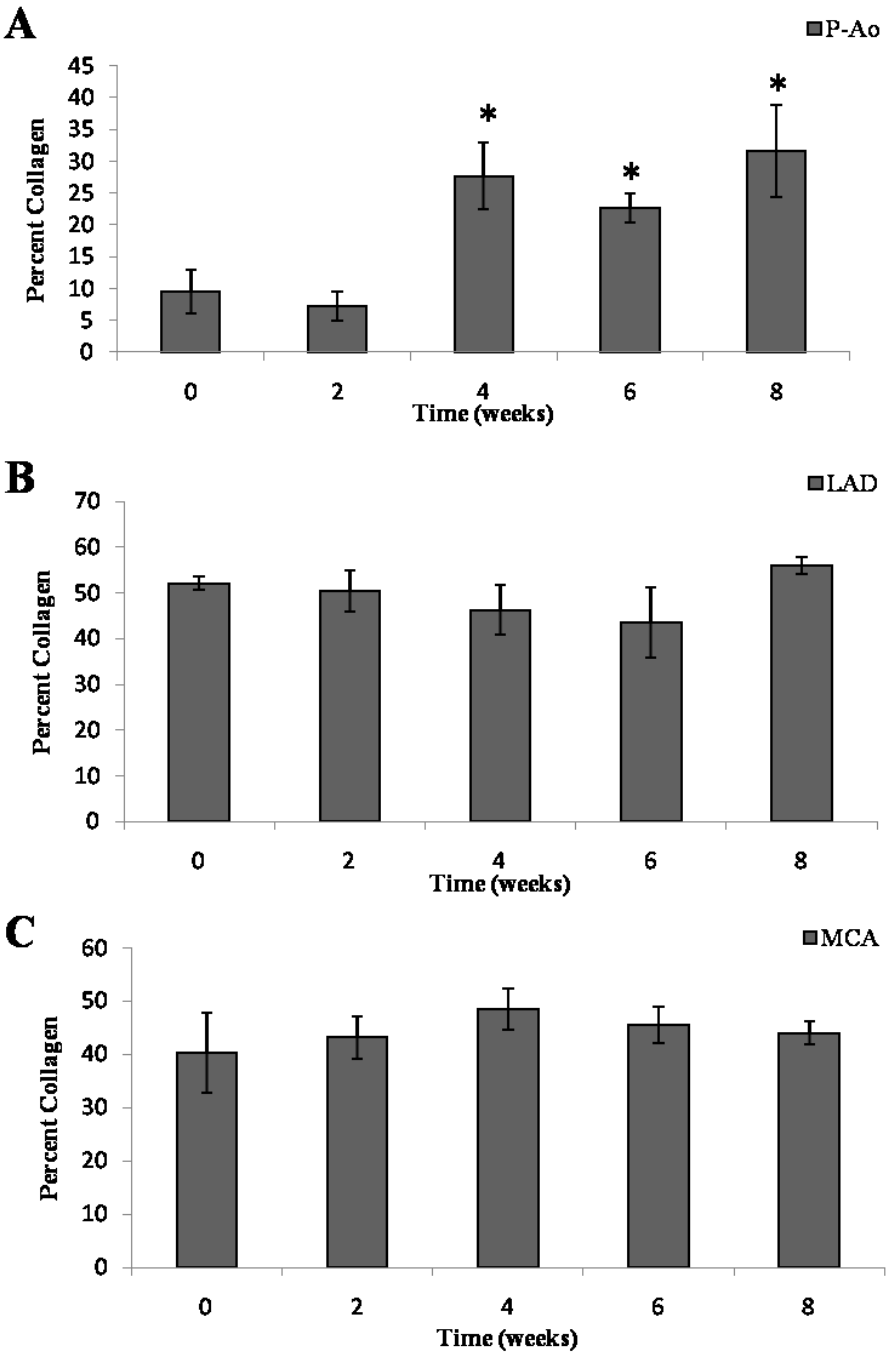

FIGURE 5.12. (**A, B, C**) Percentage of collagen (mean ± SEM) in the AP, LAD and MCA Mean ± SEM. Time 0 represents the surgery control. (**B, C**) Collagen was significantly increased in the LAD and MCA at weeks 2 and 4 (* $p < 0.05$, unequal two sample ttest). (**B**) Although not significant at week 6, collagen was significantly increased in the LAD at week 8 (* $p < 0.05$, unequal two sample t-test).

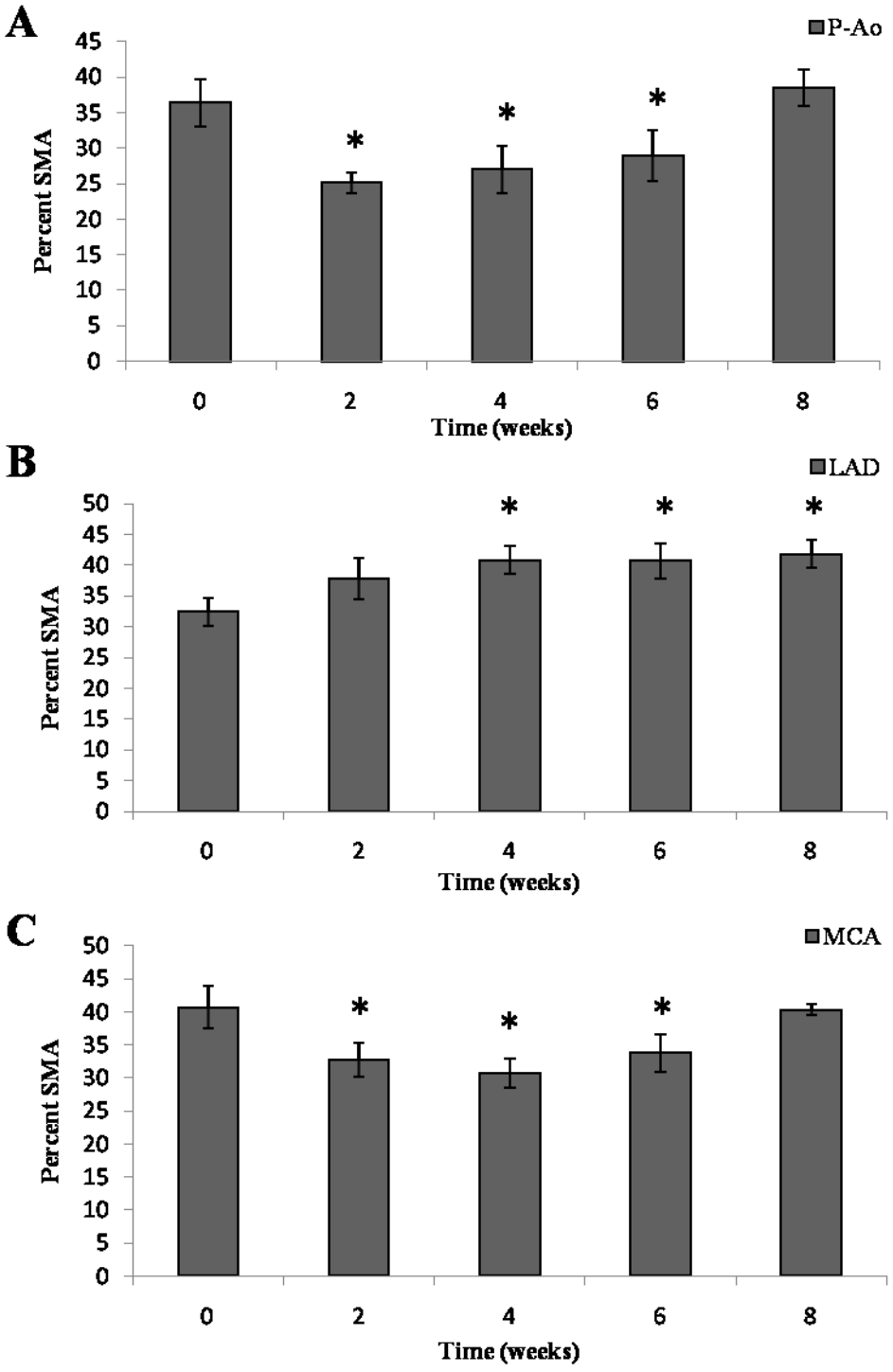

FIGURE 5.13. Percent of positively stained SMA in the P-Ao, LAD and MCA wall over time Mean ± SEM. * $p < 0.05$, unequal two sample t-test

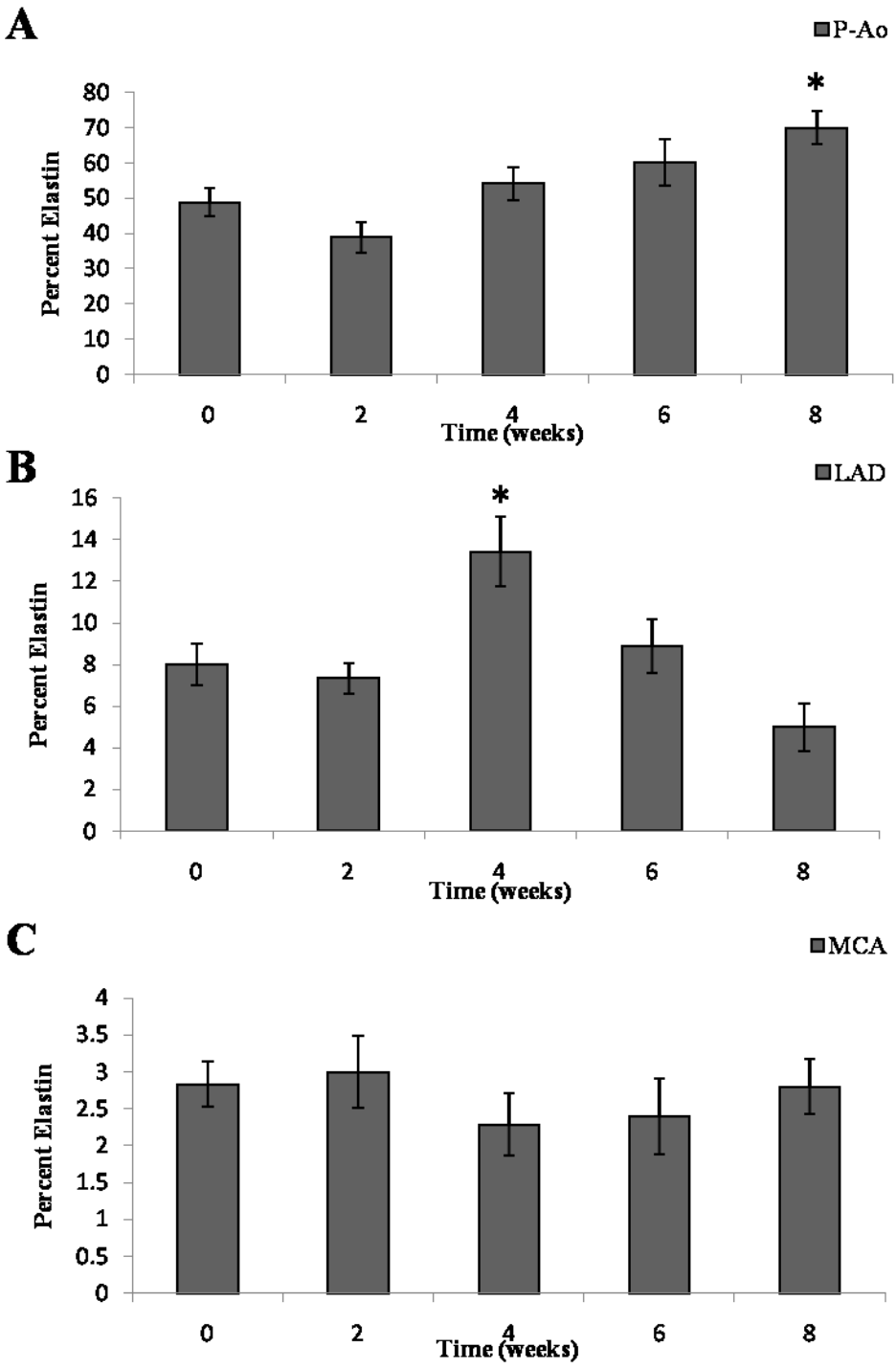

FIGURE 5.14. Percent of elastin (VVG stain) in the wall of P-Ao, LAD and MCA Mean ± SEM. Week 8 in the P-Ao and week 4 in the LAD are significantly higher than the normotensive control. * $p < 0.05$, unequal two sample t-test

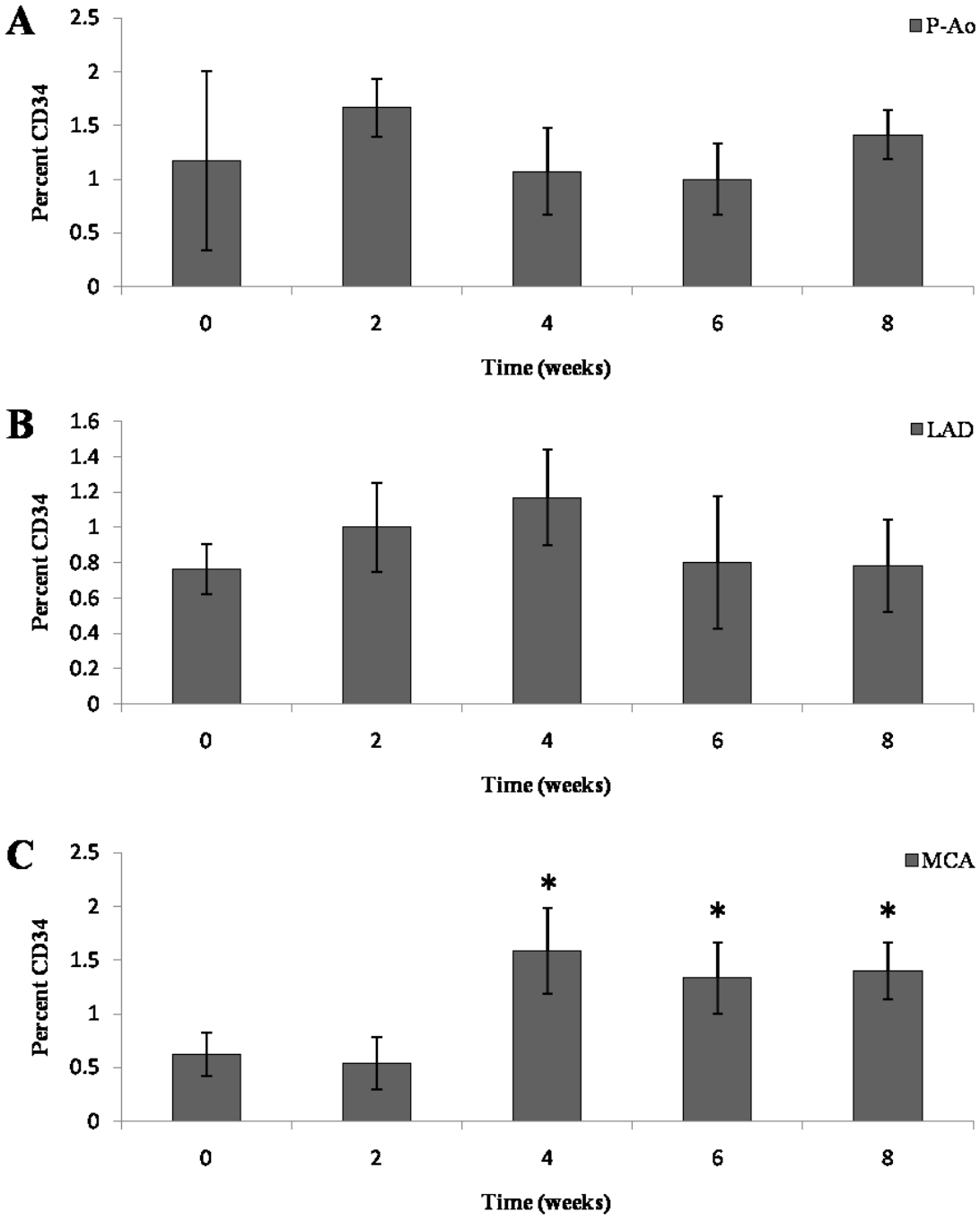

FIGURE 5.15. Percent of positive CD34 within the arterial wall of the (**A**) P-Ao, (**B**) LAD, and (**C**) MCA at each experimental time point. The average hematopeoitic progenitor cell ratio is below 2% for all arteries. (**C**) The MCA shows a slight but statistically significant increase in positive stain ratio from 4 to 8 weeks. * $p < 0.05$, unequal two sample t-test

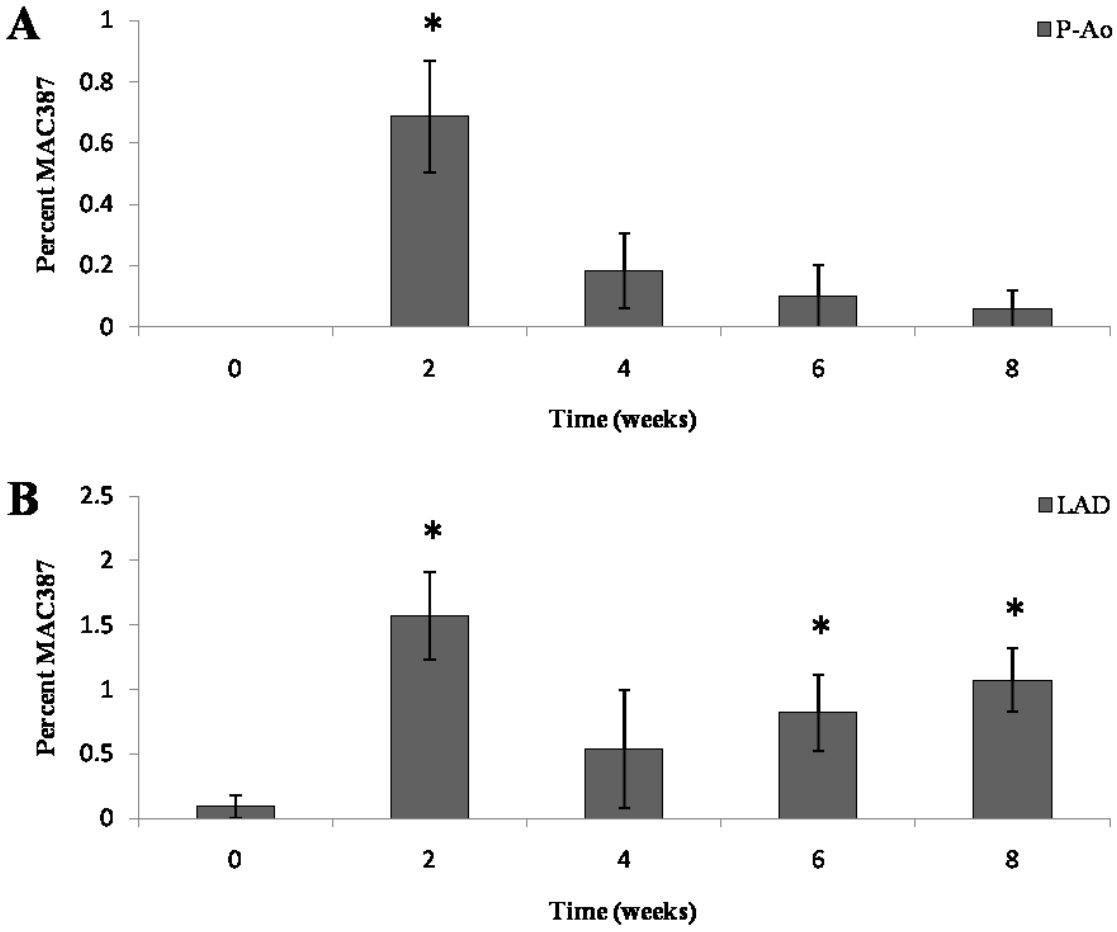

FIGURE 5.16. Percent of positive MAC387 within the arterial wall of the (**A**) P-Ao, and (**B**) LAD at each experimental time point. There were no detectable macrophages in the MCA. The average macrophage content is below 2% for all arteries. (**A, B**) At week 2 both arteries statistically have express more macrophages then the control. (**B**) The LAD also significantly elevated macrophage content at weeks 6 and 8. * $p < 0.05$, unequal two sample t-test

The cumulative arterial responses mentioned above can also be observed geographically using representative images. For example, **Figure 5.17** illustrates nearly concentric increase in wall thickness, and the distribution of SMA (red), elastin (green), and nuclei (blue) in a normotensive, 2 week hypertensive, and 8 week hypertensive P-Ao. It was observed in most P-Ao that initially the neointima consists of non-contractile cells (SMA-negative). These intimal cells then take on a contractile apparatus. Similarly, **Figure 5.18** illustrates SMA stained LAD and MCA over the hypertensive period studied herein. Although these few images cannot capture all of the observed structural responses of all 41 animals, as seen in **Figures 5.8 - 5.16**, one can observe the thickening (of the adventitia, media, and intima), increase in SMA, general morphology, and relatively constant cell density in the LAD [**Fig. 5.18 (A-E)**]. In addition, one can see for the MCA moderately constant mean wall thickness and reduction of intimal space [**Fig. 5.18 (F-J)**]. Note that the intima was classified as material between the IEL and the lumen. Thus, increased undulation as observed in the normotensive arteries [**Fig. 5.18 (F)**] will result in greater intimal thickness.

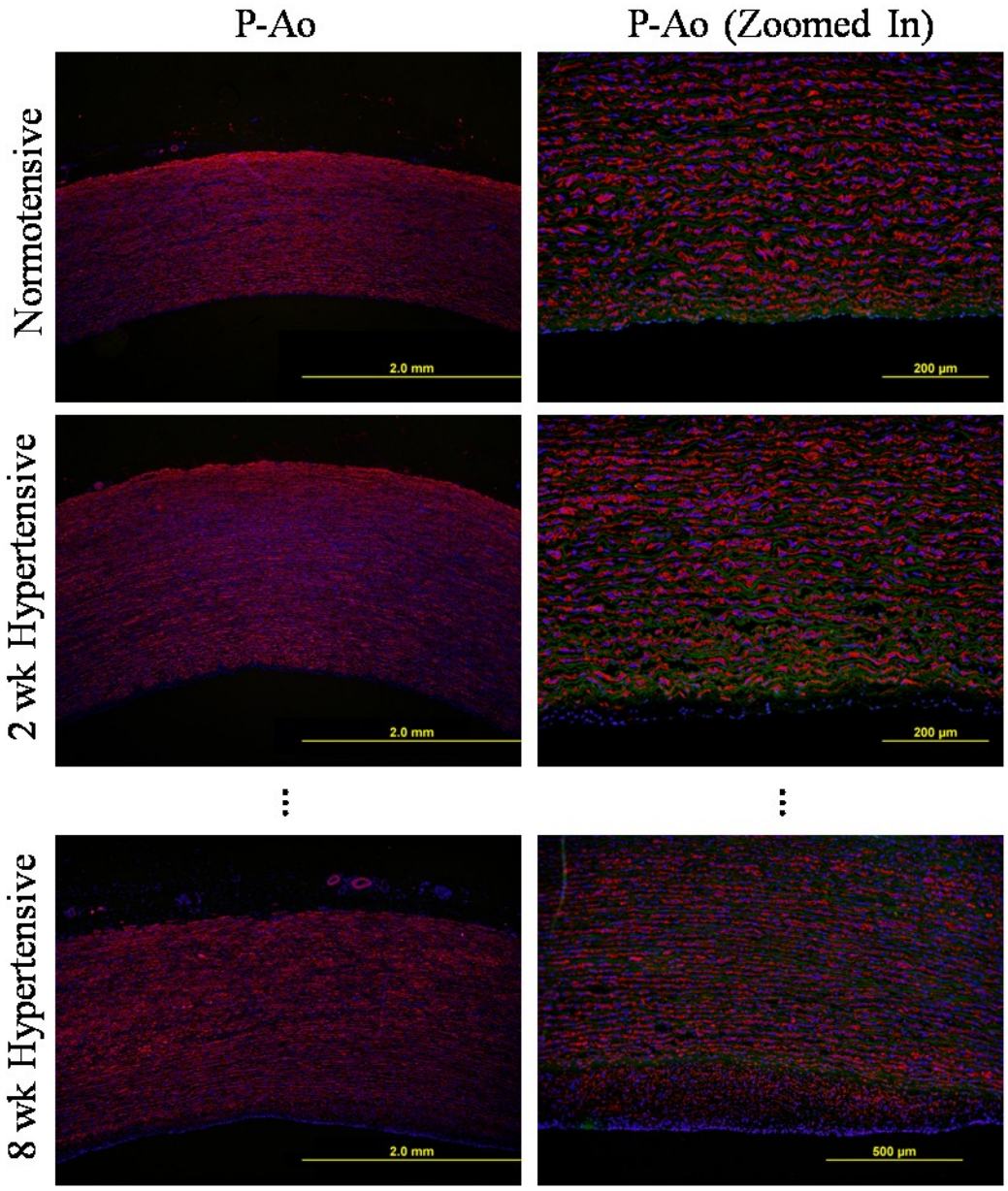

FIGURE 5.17. Smooth muscle actin stain (red) showing an increase in SMCs in the proximal aorta after 2 weeks of increased blood pressure. By 8 weeks the overall medial thickness does not change much, but the neointima increases in thickness. Blue indicates nuclei and green indicates elastin.

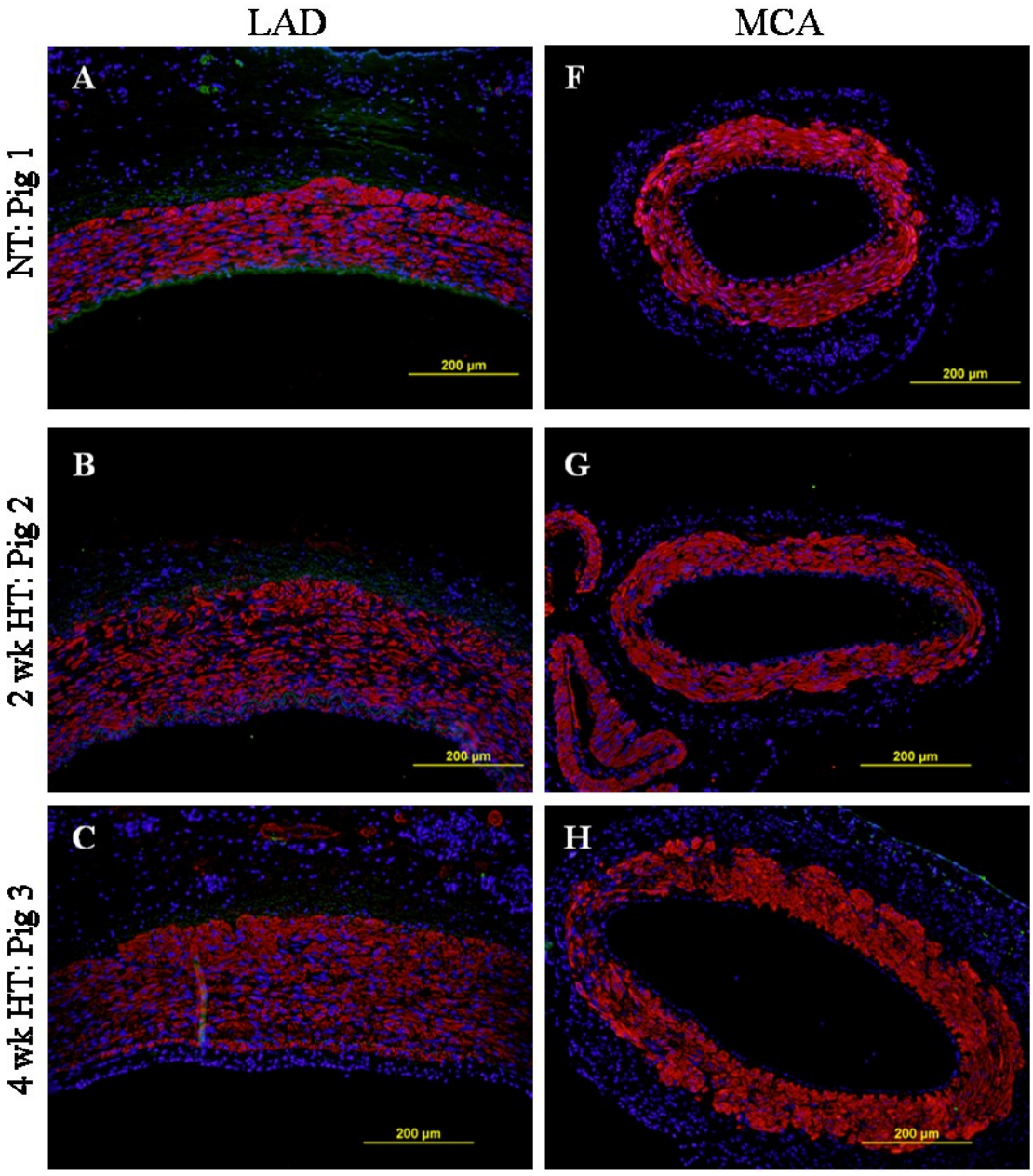

FIGURE 5.18. Representative images of the left anterior descending coronary arteries (LAD) and middle cerebral arteries (MCA) from the same pig after 0, 2, 4, 6 and 8 weeks after increasing the MAP above 150 mmHg.

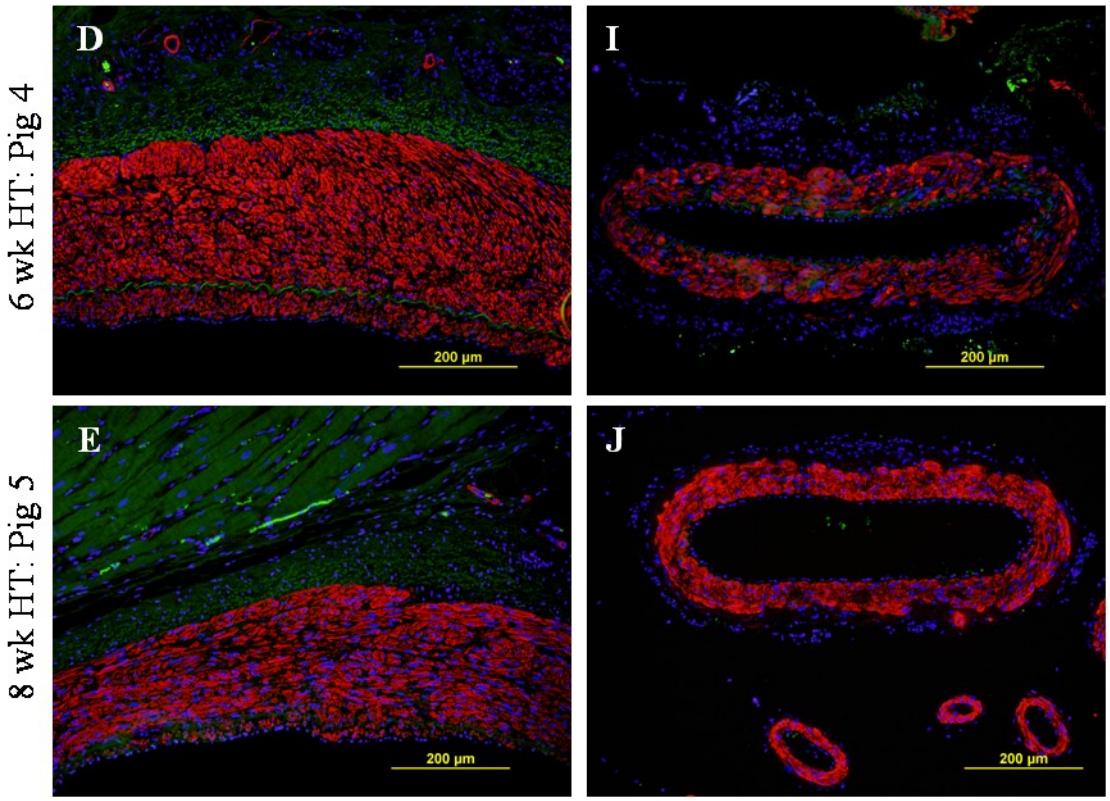

FIGURE 5.18 continued.

All arteries were stained with the hemopoietic progenitor cell (HPC) marker CD34. In addition to being a HPC marker, CD34 has been reported to be a vascular endothelial cell marker for small arteries [152]. Also, when these endothelial cells proliferate they down regulate the CD34 protein while maintaining the maintaining the CD34 mRNA [152]. HPC were observed in the adventitia and media of normotesive P-Ao, and, to a greater extent, in hypertensive P-Ao at 2 weeks. By week 6 HPC were also noticed in the intima of hypertensive P-Ao. CD34+ cells were detected in the endothelium and a few throughout the media and adventitia in the LAD and MCA of

normotensive and surgery control arteries [**Fig. 5.19 (A, F)**]. Interestingly, at 2 weeks endothelial cells in the LAD and MCA were not all positive for CD34, suggesting a possible switch to a more proliferative phenotype. By week 4 the endothelium is CD34+ again. In addition, hematopeitic/endotelial cells are seen primarily in the intima and adventitia of LAD and in the intima and media of MCA. The overall density of hematopoeitc cells decreases in the LAD by week 6 and even more so by week 8. However, presence of hematopoetic cells in the intima, media and adventitia of the MCA remain after 6 and 8 weeks of elevated MAP.

Extravasation of progenitor cells into the neointimal space corresponds with a lack of SMA expression. For example, **Figure 5.20** illustrates two serial sections of an 8 week HT P-Ao, one stained for SMA and the other for CD34; neointimal cells were positive for CD34 but negative for SMA. Likewise, neointimal cells positive for CD34 and negative for SMA were also observed in the LAD. It is important to note, however, the majority of neointimal cells negative for SMA were not CD34 positive.

Arteries were also stained for a macrophage marker, MAC387. Macrophages were present in the adventitia and media of the P-Ao and LAD at 2 weeks [**Fig. 5.21**]. Macrophages were also observed, primarily in the adventitia and intima still, at weeks 4, 6 and 8 in these artery types. There were no macrophages seen in the MCA at any time point.

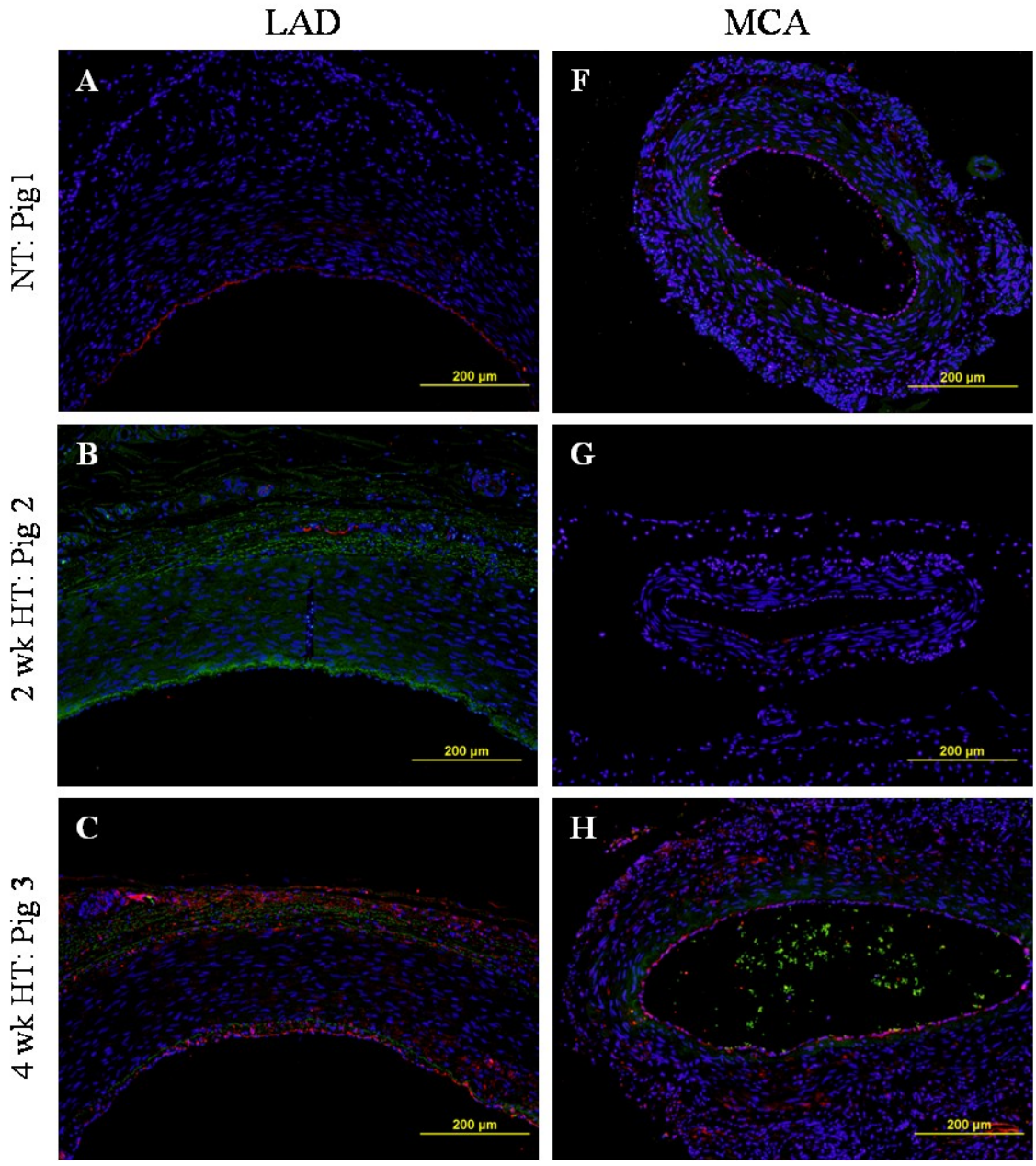

FIGURE 5.19. Representative images from the LAD and MCA stained red for hematopoietic progenitor cells (HPCs), blue for nuclei, and autofluorescent green for elastin and platelets.

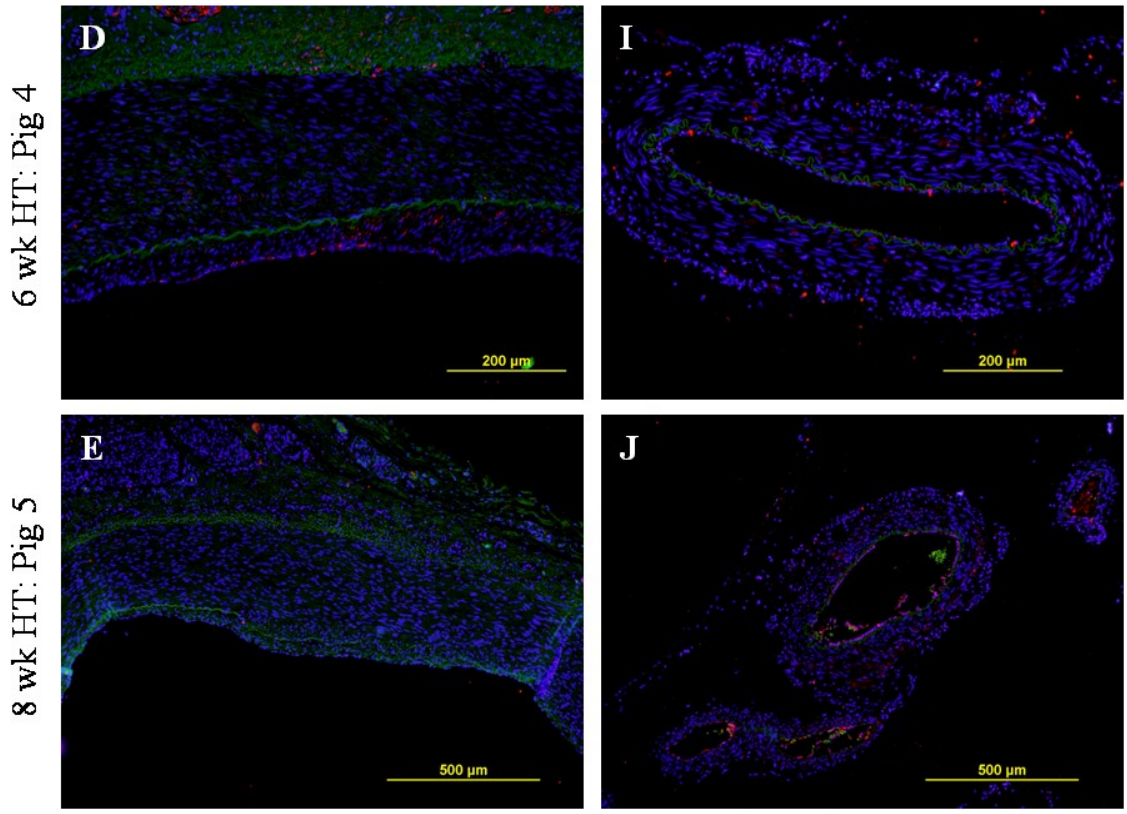

FIGURE 5.19 continued.

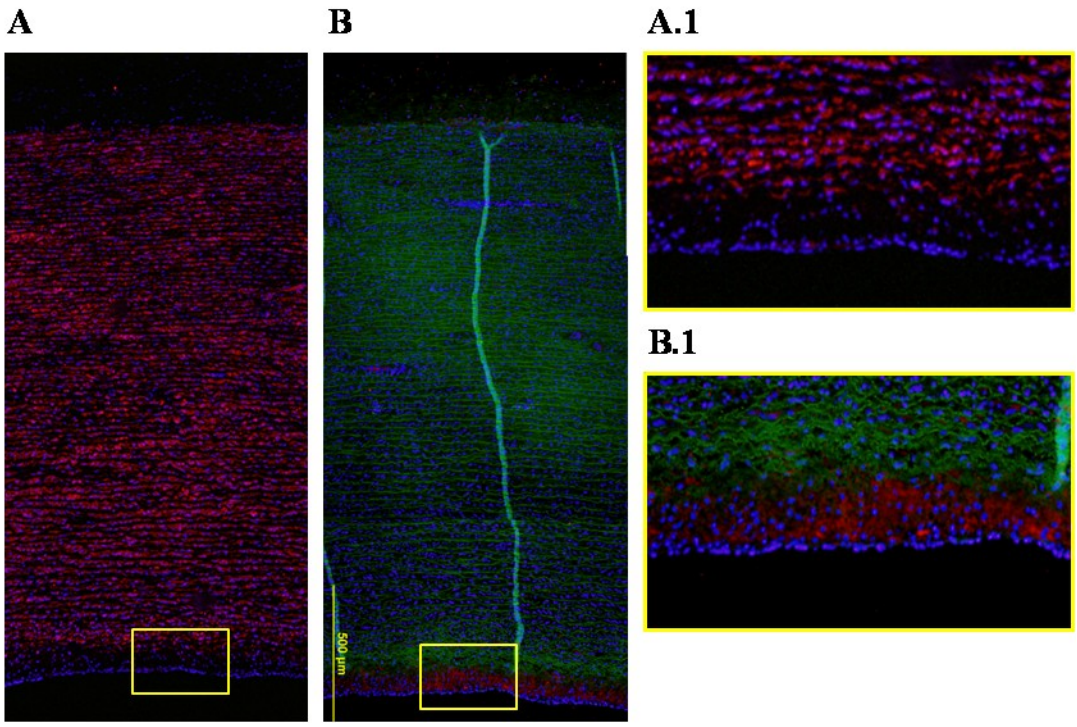

FIGURE 5.20. Serial sections of a 4 week HT P-Ao stained for (**A**) SMA or (**B**) CD34. Red indicates positive SMA staining in **A** and **A.1** and positive staining for CD34 in **B** and **B.1**. Magnified neointimal images of the yellow boxed region in **A** and **B** (i.e. **A.1** and **B.1** respectively) are shown on the right. Note, the vertical green line in **B** is due to a fold in the artery sample.

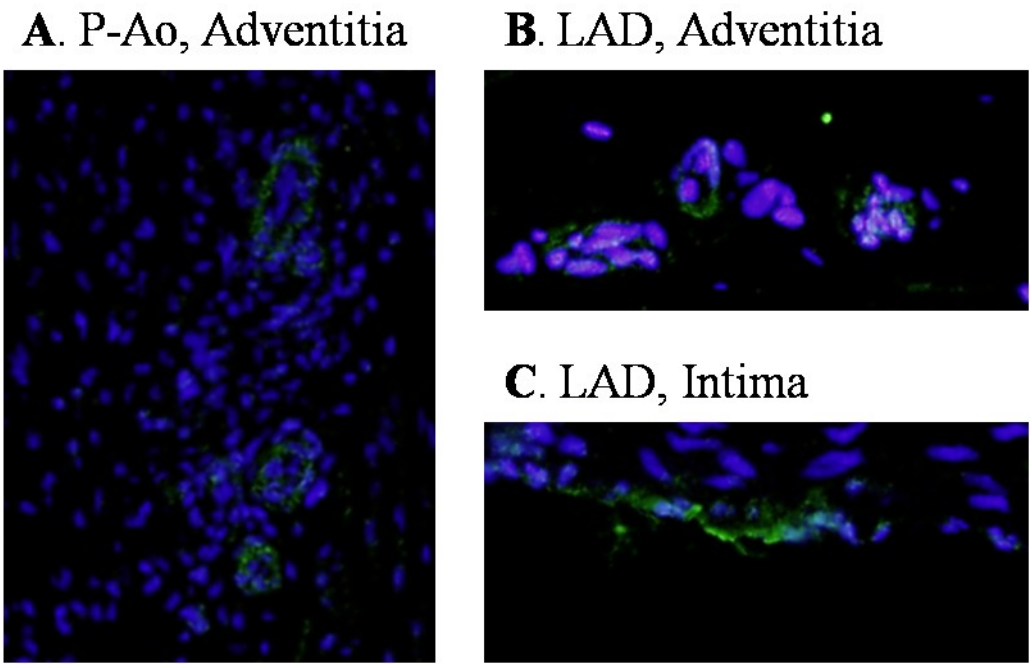

FIGURE 5.21. Several macrophages (green) were observed in the (**A**) A-Po and (**B, C**) LAD after 2 weeks of elevated blood pressure. Macrophages were located primarily to the adventitia and intima either artery type. Blue indicates nuclei.

Discussion

The results reported here are consistent with the well known observation that hypertension causes structural changes within the arterial wall, often primarily manifesting as a thickened media. Such findings were extended herein by documenting differential progressive changes in elastic (proximal thoracic aorta) and muscular (coronary and cerebral) arteries in the same animals during the progression of hypertension due to an aortic coarctation. In particular, we quantified changes in the extracellular matrix, specifically collagen and elastin, as well as cellular composition. We found that the degree and time course of arterial remodeling depends, in part, on the location of the vessel within the arterial tree. Compared to the elastic artery (P-Ao), the inner radii and thicknesses in the muscular arteries (LAD and MCA) fluctuated more, cell density over the entire wall was greater, and collagen ratios were constant despite the marked geometric alterations. Nonetheless, differences within the muscular arteries were observed. For example, the MCA initially lost overall contractility whereas the LAD showed an increase; this may be due to the increased proximity of the LAD to the myocardium. Moreover, the LAD significantly increased in wall thickness and inner radius whereas the MCA does not.

Many animal models support the clinically observed identification of hypertension as a risk factor for atherosclerosis (e.g.,[153, 154]). Among other factors, the role of increased macrophage activity within the wall may be central to both the hypertension-induced structural changes and the associated acceleration of atherosclerosis [84]. Angiotension II (ANG-II) induced hypertension in rats results in a

significant increase of macrophages in the adventitia of the aorta within 7 days [16, 155]. In spontaneously hypertensive rats, the presence of subendothelial macrophages was maximal in the carotid artery, less in the aorta, and nonexistent in the renal artery [156]. In our porcine coarctation model of hypertension, we observed several macrophages in the adventitial and neo-intimal spaces of the P-Ao and LAD starting at 2 weeks, but none in the MCA even after 8 weeks. Macrophages were conserved to the adventitia and neointimal spaces in both the P-Ao and LAD; only a few macrophages were observed in the media at week 8. These findings suggest that monocyte infiltration through both the lumen and vaso vasorum (or peri–adventitial tissue) may play a role in the progression of hypertensive induced remodeling of the arterial wall.

Circulating hematopoietic progenitor cells (HPCs) may localize to damaged arterial tissue through a chemotactic response. Moreover studies over the last decade show the adventitia in fully developed blood vessels contains residential HPCs [149-151]. These HPCs are capable of migrating into the media and intima. Herein we also document the presence of HPCs in the normal and hypertensive aortic wall. An increase in HPCs is seen in wall of the P-Ao by 2 weeks of hypertension, the LAD by 4 week of hypertension, and the MCA by 4 weeks of hypertension. Others have reported bone marrow derived HPCs in pulmonary blood vessels following hypoxia [157, 158] or monocrotaline induced pulmonary hypertension [159]. Colocalization of vWF+ with CD34+ markers suggests hematopoietic progenitor cells gave rise to these new endothelial cells [160, 161] or, and maybe more likely, since endothelial cells are CD34+ in normotensive controls, the CD34 marker is expressed in vascular endothelial

cells of small arteries [152]. An increased compressive radial stress, such as those experienced by the arteries during hypertension, has been shown to promote the expression of smooth muscle-like proteins (αSMA and SM-MHC) in bone marrow stromal cells [162]. Likewise, HPC in the adventitia and media of the P-Ao also co-express αSMA. However, we observed most HPCs in the intima, media, and adventitia of the LAD and MCA do not co-express αSMA. Therefore, some contractile cells in the wall of hypertensive P-Ao appear to arise from a hematopoietic origin.

Within the arterial wall there is a mixture of macrophages, HPC, fibroblasts, endothelial cells, etc., and three primary structurally significant constituents. These are constituents are elastin, fibrillar collagen, and SMCs. We show herein for the mini-pig in normal conditions the percent of collagen, elastin and SMC (indicated by αSMA) is 9.5, 48.9, and 36.4 for the P-Ao, 52.2, 8.6, and 32.4 for the LAD, 40.3, 2.8, and 40.7 for the MCA. One can assume that the rest of the mixture is due to proteoglycans, aqueous material and other cells. After 8 weeks of elevated blood pressure the fractions of these constituents are different; that is the percent of collagen, elastin, and SMC is 31.6, 70, 38.5 for the P-Ao, 56, 5, 41.8 for the LAD, and 44, 2.8, and 40.3 for the MCA. Note that the sum of the constituents of the 8 week P-Ao and LAD are over 100%; therefore, assuming no two constituents can occupy the same space we suggest this overestimate may be a product of using serial images samples when staining. That is, to determine collagen we used PSR, for elastin VVG, and for SMC we used SMA, thus requiring 3 separate samples with slightly different geometry and composition. In addition, in order to get better resolution we took at least 2 images of wall sections. However, this means

we may miss some of the spatial variation within each sample for any given stain. Nonetheless, knowing the mass fractions of each will be instrumental in mathematically modeling arterial behavior during G&R.

The results presented herein suggest that fibrillar collagen production in response to elevated blood pressure depends on the type of artery. The MCA and LAD had insignificant changes in the total amount of collagen whereas the relative amount of collagen increased significantly by week 4 and remained elevated in the P-Ao. In addition the cells in the P-Ao may slightly enlarge in preparation for collagen production; then after collagen has been laid down the arterial cells may proliferate. Although not statistically significant, cell density decreased by 5% from the normal value at week 2 and then increased by 8% from the normal value by week 4. Therefore, we suggest that cell hypertrophy occurs first and then hyperplasia or nuclear ploidy. Moreover, although statistically insignificant, in the LAD we see a slight increase of 5% in cell density at week 2. Afterward the LAD does not produce more collagen. This suggests, rather than hypertrophy in preparation for matrix production, hyperplasia or nuclear ploidy occurs first in the LAD. Yet current reports, as to whether hypertension is a result of hypertrophy [64, 130, 163, 164] or hyperplasia [165, 166], are conflicting. Herein, we show the overall nuclei density remains nearly constant, amid increases and decreases in thickness over the growth and remodeling, time course. This implies there is a preferred cell density that the artery seeks to maintain.

In addition to each artery type having a nearly constant cell density over the G&R period, the distribution of nuclei within the arterial wall displaced similar trends

over the G&R period. A greater nuclei density within the initial 10% of the arterial wall [**Fig. 5.11**] may be due to greater packing density in the intima. That is, the length of cells along the luminal surface is in the axial direction allowing for more cells to align in parallel. Adventitial cells are also primarily oriented in the axial direction, however, space filling matrix (e.g. collagen) also resides in the adventitia. However, the fact that the cell count remains elevated and nearly constant within the initial three quarters of the P-Ao wall, amongst space filling elastin, indicates that overlapping of the concentric SMC layers may also contribute to a greater cell count [**Fig. 5.11 (A)**]. Unlike the P-Ao and LAD, the distribution of nuclei as a function of position trend appears to change over time. This may be due to the relatively fewer number nuclei per MCA sample (on the order of hundreds rather than thousands for the P-Ao and LAD) and greater density (0.005497 versus 0.000127, 0.00378 cells/μm^2).

In response to a sustained increase in pressure, it appears that the arterial wall thickens gradually in attempt to restore the intramural stress to homeostatic values [36, 164]. Herein, the wall of the P-Ao and LAD thickened. For the P-Ao, this increase in mass also led to a decreased actin fibers followed by an increase in collagen. Whereas for the LAD, the increase in mass did not result in a decrease in total actin fibers; likewise an increase in collagen was not observed either. This suggests that these arteries responded to elevated blood pressure in two ways: first, by increasing wall thickness (possibly to restore hoop stress to normal, as thickness is inversely related to hoop stress), second, by laying down new material (e.g. collagen in attempt to the stiffness, thus resist the increase in load). Based on the responses for the two types of arteries

shown here, it seems that the muscular artery increases in thickness but does not lay down material perhaps due to the greater amounts of basal collagen to start with. The elastic artery also increases in thickness, then loses contractility, and produces structurally supportive matrix. This is consistent with the inverse correlation proposed by Stegemann & Nerem, 2003 [57, 167]; that is, increased cell contractility (SMA) often associates with decreased cell proliferation and vice versa. Knowing the geometry and cellular changes over time can aid in the development of improved computational G&R models as well as contribute to clinical and pharmaceutical applications.

In summary, we suggest that in aortic coarctation models of hypertension, effects of increased pressure manifest first in the central arteries and later in distal muscular arteries. It appears tissue maintenance via, a loss and then increase of cytoskeleton actin fibers, production of fibrillar collagen, production of elastin, hyperplasia or hypertrophy with nuclear ploypoid, and recruitment of hemopoeitic progenitor cells and monocytes occurs in the elastic aorta. In the muscular coronary, we see similar changes albeit it appears actin fibers are recruited and collagen production is only slightly increased in order to maintain constant the overall ratio ~55%. In the muscular cerebral artery, despite a temporary loss in contractility there is little structural change. Others have also observed functional changes occurred in coronary arterioles by 8 weeks following the initiation of hypertension [168].

CHAPTER VI

ATHEROSCEROSIS – EXPERIMENTAL FINDINGS

Overview

Regional material properties of tissues influence the intrinsic cellular responses and vice versa. Atomic Force Microscopy (AFM) was used to measure the pointwise modulus of elasticity of healthy aortas and plaques at the micron level. Slices of advanced plaque were obtained from a widely used animal model of atherosclerosis (ApoE-/- mice). Median asymptotic pointwise moduli were 18.7 kPa and 1.5 kPa for the unloaded healthy wall (n = 25) and plaque material (n = 18), respectively. When the normal wall was pressurized for testing, two mechanically distinct populations were identified by comparison to a normal cumulative distribution, with median asymptotic pointwise moduli of 9.8 and 76.7 kPa (n = 16). Most of the plaques behaved like a homogeneous linear elastic material and were identified to be lipid-laden through histology and immunofluoresecence. Understanding the mechanics and mechanobiological factors involved in lesion development and remodeling could lead to patient-specific strategies to treat better those lesions that are vulnerable to rupture.

Introduction

Apolipoprotein E deficient (ApoE-/-) mice do not express ApoE, an important ligand for receptor-mediated removal of lipoproteins from the plasma; lack of ApoE causes low density lipoproteins (LDLs) to accumulate within the arterial wall, which leads to atherosclerosis. Atherosclerotic plaques in ApoE-/- mice exhibit many

characteristics found in humans [169, 170], as, for example, compensatory enlargement, medial thinning, and elastolysis [26, 171, 172].

Atherosclerotic plaques are complex materials, consisting of aberrant accumulations of smooth muscle cells (SMCs), foam cells, collagen, calcium, and necrotic debris in advanced human lesions [173]. The distribution and material properties of these many constituents can be initiators or indicators of plaque vulnerability. For example, many studies suggest that plaques rupture more frequently within regions of mechanical stress concentrations, located along the border of soft lipid pools (e.g. [174, 175]) or near deposits of calcium [176]. Many such predictions are based on continuum models that attempt to account for differences in mechanical properties (stiffness) among lumped plaque types: for example, grouping plaques as primarily fibrous, lipid laden, or calcified [170, 177]. Yet, in vitro measurement of the stiffness of individual constituents within the plaque has not been accomplished using a direct method.

Many autopsy studies have provided important information on the morphology, composition, and pathology of plaques, which in turn led to a classification scheme advocated by the American Heart Association [178], with subsequent revisions proposed by others (e.g., [173, 179, 180]). Efforts are also intensifying to advance medical imaging to enable detection of plaque composition (i.e., to distinguish regions containing calcium, dense fibrous tissue, lipids, smooth muscle cells, and even increased metabolic activity) for purposes of diagnosis and designing interventions [181, 182]. In particular, the technique known as elastography is emerging as a potentially useful tool to estimate

mechanical strain and stiffness within plaques, though there remains a need for a better correlation between plaque composition and stiffness to enable the method to predict possible vulnerability [183, 184]. Indeed, this correlation of composition to stiffness must be known to infer the structural integrity of a plaque based on any method, which would represent a significant clinical advance.

In addition to the data collected on human lesions, ApoE-/- mice provide a unique opportunity to study the natural history of atherosclerotic disease progression and to identify underlying molecular mechanisms. Indeed, the ApoE-/- mouse has also been used for studying balloon angioplasty and intravascular stenting based on the similar procedural success rates and morphology with humans post-intervention [185]. Yet there has been little attention directed towards quantifying the mechanical properties of plaques in the ApoE-/- mouse, even though computational models can now predict stresses in these lesions [186]. Because the area of a typical ApoE-/- aortic plaque is only ~100 mm^2 by 56 weeks [186], one of the challenges in quantifying potential regional mechanical properties is the smallness of the associated plaques.

Therefore, in this chapter we address this need by combing Atomic Force Microscopy (AFM), histology, and standard immunofluorescence, to determine plaque stiffness in the axial direction, including regional variations within a plaque.

Methods

Animal Model. All animal protocols were approved by the Institutional Animal Care and Use Committee at Texas A&M University. ApoE-/- breeder mice were purchased from Jackson Laboratories and maintained by the Comparative Medicine

Program at Texas A&M University for up to 56 weeks. The colony was switched from a 9% fat chow diet to a western-type diet consisting of 21.2% fat and 0.2% cholesterol (Harlan Tekland, Madison, WI) after an initial period of 16 weeks. Heterozygous and wild-type mice from a fibrillin-1 deficient colony, with a C57/S129 background, were also used to study the mechanical properties of the normal aortic wall.

Sample Preparation. AFM force-indentation testing was performed on circumferential cross-sections of the normal aortic wall and atherosclerotic plaques (thickness of 0.5 mm, outer diameter of 0.5 to 1.5 mm). The suprarenal aorta (i.e., between the diaphragm and renal arteries) was harvested by blunt dissection from ApoE-/- mice at ages ranging from 42 to 56 weeks (*n = 13 animals, n = 18 plaques*), with at least one plaque detected visually in each animal [**Fig. 6.1(A)**]. Next, the aorta was embedded in a 2% agarose gel, just prior to solidification, and then sectioned into 0.5 mm thick segments using a vibratome (Vibratome Series 1000, The Vibratome Company, St. Louis, MO). Each tubular section was then affixed to a 60 mm diameter petri-dish with RP30 instant adhesive (Adhesive Systems, Inc, Frankfort, IL); 1.7 mL of phosphate buffered saline (PBS) was then added to the petri-dish to submerge the sample [**Fig. 6.1(B)**].

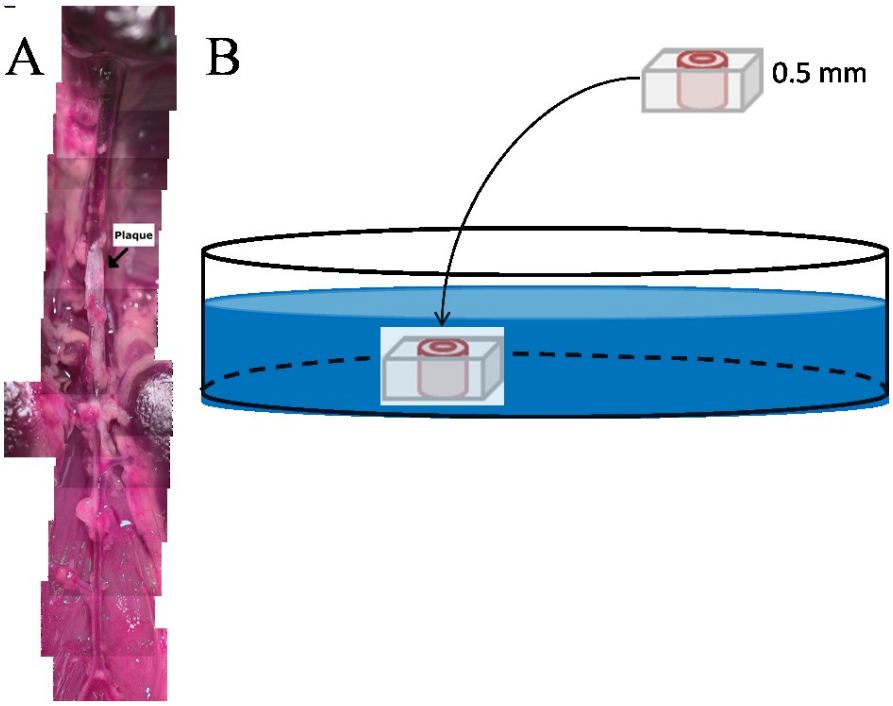

FIGURE 6.1. (**A**) Plaque was detected by gross examination in the suprarenal aorta from ApoE-/- mice aged 42 to 56 weeks. (**B)** The desired aortic section was embedded in 2% agarose gel, sectioned with a vibratome at a thickness of 0.5 mm, mounted to a 35 mm diameter petridish, and mechanically tested through nano-indentations in the axial direction.

Aortic samples were prepared from the control mice in a similar fashion, with a few modifications. Following blunt dissection, the infrarenal aorta was either embedded in 2 % agarose gel while pressurized to approximately 100 mmHg (*n = 15 animals, n = 20 aortic walls; in 5 cases 2 aortic wall samples were obtained from one animal*) or embedded while unpressurized (*n = 30 animals, n = 30 aortic walls*). Pressurization was maintained by cannulating the proximal aorta (near the renals), injecting dyed agar antegrade through the aorta, ligating the distal aorta (near the iliacs), and bringing the pressure to 100 mmHg as determined by a connected pressure transducer (Living

Systems Instrumentation, Burlington, Vermont). After solidification of the agar by cooling to room temperature, the aortic segment was sectioned and affixed to the petri-dish, and immersed using PBS as described above.

AFM Testing. Force-indentation data were acquired using a Bioscope System AFM (Veeco Instruments, Santa Barbara, CA) equipped with a Nanoscope IIIa controller and mounted on a Zeiss Axiovert 100 TV inverted optical microscope (Carl Zeiss, Thornwood, NY). A 5-μm diameter spherical tip (borosilicate glass bead) attached to a silicon-nitride cantilever having a spring constant of either 60 or 120 pN/nm (Novascan, Ames, Iowa) was used to indent the samples. A spring constant of 60 pN/nm allows increased sensitivity in the approach curve for softer samples; in contrast, a cantilever with a spring constant of 120 pN/nm gives a more accurate response for stiffer samples. After laser diode positioning adjustments on the cantilever, deflection sensitivity (i.e. probe deflection versus piezo z-position) was determined by acquiring force curves on a 60 mm polystyrene petri-dish in PBS at 0.5 Hz. Afterward, the sample was located within the petri-dish and visualized in real-time using a Zeiss 32X objective and video camera (Pulnix, model TM 34KC, Yokohama, Japan). The AFM cantilever tip approached the sample at a frequency of 0.5 Hz with a z-scan size of 800 nm (speed of 0.8 μm/s). After recording at least 30 consecutive indentation force-depth curves at each location on the artery/plaque, the tip was retracted to its original position. Similarly, additional curves were recorded over regions 80 x 80 μm^2 at intervals of about 20 μm achieved using the x and y offset controller. To move to a different macroscopic region, the sample and petri-dish were moved together via the x-y stage controlled by the Nanoscope. The AFM tip

was then again brought into contact with the surface of the sample, and force curves were acquired over another 80 x 80 μm^2 region. This process was repeated until the entire region of interest was mapped. After mechanical testing, a live/dead viability / cytotoxicity kit for mammalian cells (Invitrogen, Carlsbad, CA) was used to determine the viability of the tissue.

Histology and Immunofluorescence. A 0.5 to 1.0 mm long aortic section adjacent to that tested with the AFM was fixed with 4% paraformaldehyde for 1 hour at room temperature, then placed in 30% sucrose overnight at 4° C for cryoprotection. The sample was then embedded in "optimum cutting temperature" compound (OCT), flash-frozen with liquid nitrogen, and cut into 5-μm thick sections for standard histology and immunofluorescence. Serial sections were stained with hematoxylin and eosin (H&E) for general morphology, Verhoeff-van Gieson (VVG) for elastin (Verhoeff) and collagen (van Gieson), Masson's trichrome for collagen, oil red O (ORO) for lipids, von Kossa for calcium, alpha smooth muscle actin (αSMA) for contractile cells, and von Willebrand factor (vWF) for endothelial cells. Optimal conditions for αSMA stain were 1:100 dilution of primary antibody (ab5694, Abcam) for 1 hour at room temperature in PBS followed by heat induced (pressure cooker) sodium citrate antigen retrieval, then exposure to a 1:500 dilution of Alexa Fluor® 594 secondary antibody (Invitrogen, A11012) for 30 minutes. Optimal conditions for vWF stain were 1:100 dilution of the primary antibody (Abcam, ab6994) for 1 hour at room temperature in PBS, with heat induced (pressure cooker) sodium citrate antigen retrieval and then exposure to a 1:500 dilution of Alexa Fluor® 594 secondary antibody (Invitrogen, A11012) for 30 minutes.

Pointwise Elasticity Measurement. AFM force curves were analyzed as described in Costa et al. (2006). Prior to sample testing, we recorded the deflection sensitivity in PBS using the bottom of an otherwise bare petri-dish. Sensitivity calibration allows calculation of the applied force f_{sphere} (nN) derived from the measured cantilever deflection *d* (V) via

$$f^{sphere} = kd_s d, \tag{6.1}$$

where k is the specified spring constant (nN/nm) for the cantilever and d_s is the deflection sensitivity (nm/V); the cantilever deflection was determined in volts from the laser position on the photodetector.

Cantilever deflection resulting from the approach/retraction cycle was monitored as a function of piezo movement, namely

$$\delta = z - d_s d \tag{6.2}$$

where, δ is the indentation depth (nm), or deformation of the aortic wall or plaque, and z is the piezo displacement (nm) during testing. One can calculate the Young's modulus (E), a measure of material stiffness, using the Hertzian relationship for the indentation of a flat, homogeneous, semi-infinite elastic material by a rigid spherical probe [187]. In this case,

$$f^{sphere} = (4/3)(E/(1-v^2))\sqrt{R\delta^3} \tag{6.3}$$

where v is the Poisson's ratio, often assumed to be 0.5, and R the radius of the sphere. The associated simplifying assumptions to use the Hertzian equation generally do not apply for cells or biological soft tissues, however. Therefore, to accommodate for any

nonlinearities we calculated the apparent pointwise ($\widetilde{E}_i$) modulus at each point (i) of the approach curve (i.e. for all 512 points along the 800 nm approach curve), that is,

$$\widetilde{E}_i = (3/8)\left(f_i^{sphere}/\sqrt{R\delta_i^3}\right) \tag{6.4}$$

where f_i^{sphere} is the force, in nN, at each data point and $\sqrt{\delta_i^3}$ is the indentation depth, in nm, at each data point.

The initial point of contact was first determined by fitting a bi-domain polynomial algorithm to the AFM force curve (see [188] for more details). By using a linear least squares regression, error was minimized between a line fitted through the pre-contact region and a cubic polynomial fitted to the post-contact region of the indentation, $\sqrt{\delta^3}$, versus approach force, kd_sd, curve. If the goodness of fit (i.e., R^2 value) fell below 0.9, it was typically due to premature convergence on a local contact point caused by a sharp change in deflection during contact. To accommodate these cases, and to ensure we found the global contact point, we included a loop to the algorithm to change the initial contact point incrementally, within 30 points out of the 512 in the indentation curve, until the R^2 value leveled out, typically at around 0.999. A local apparent pointwise elastic modulus was calculated from each curve. The mean pointwise modulus and mean force ± SEM at each point, for all curves acquired at each location, were then plotted versus the mean indentation. All pointwise moduli converged to an asymptotic value after the probe attained a certain indentation depth, typically less than 30 nm.

Statistical Analysis. To minimize noise, we removed pointwise moduli corresponding to indentations ≤ 10 nm of the approach curve. A total of approximately

750 curves per wall and 1,650 curves per plaque sample were analyzed (i.e., ~30 curves per location, ~25 locations per aortic wall sample, and ~55 locations per plaque sample). All asymptotic stiffness values for each condition (unloaded aortic wall, pressurized aortic wall, or plaque) were examined graphically using histograms [**Fig. 6.3**]. The data were transformed from a right-skewed to a distribution more Gaussian in appearance using the natural logarithm. The median was calculated for original data and the median, mean, and standard deviation were calculated for original data and data transformed using the natural logarithm. Differences in the transformed populations were evaluated using an unpaired two-sample t-test.

Histomorphometry. To correlate the real-time AFM images, obtained during the experiment that detailed the tested locations, with the histology/immunofluorescence of the adjacent sample, we scaled the histological images using GIMPshop 2.2.8. After obtaining the best match, stiffness values were overlaid on the histological images. Due to extra handling and occasional loss of sample between the histological sample and mechanically tested samples, there were slight geometrical differences.

Results

Plaques were grossly noticeable in the suprarenal aorta in all ApoE-/- animals (*n = 12*, 42 to 56 weeks). Plaques were rarely seen in the proximal thoracic aorta and infrarenal aorta, however. **Figure 6.1** shows the ventral view of a 45.6 week old male ApoE-/- aorta as well as a schematic of the subsequent preparation for testing. Interestingly, large flat plaques seemed to form eccentrically on the ventral side, whereas smaller plaques taking on the shape of blisters protruded into the lumen on the dorsal

side. In order to obtain a smooth surface, as is required for accurate AFM indentation testing, the soft vessels with inlayed plaque(s) were reinforced with 2% agarose gel and sectioned prior to testing.

After calibration of the AFM probe, the plaque was detected and tested. **Figure 6.2** shows all stiffness curves collected from 52 locations on a representative plaque plus the associated histology / immunofluoresence. Most of the pointwise moduli curves are only depth dependent for the first 10 nm. This early decrease in stiffness may be due to noise as the probe transitions from fluid to a sample surface with slight irregularities (Elkin et al., 2007). The plaque material shown here appears very soft and almost linearly elastic. Therefore, the asymptotic pointwise moduli were used to evaluate the correlation between mechanical properties and plaque structure. By superimposing the histological images onto the asymptotic stiffness representation, localized increased stiffness near the shoulders of a pure lipid region (ORO) were seen. In addition, stiffness values near 9 kPa corresponded approximately with the few contractile cells (SMA). Positive vWF was found in the endothelial layer lining the lumen. Some positive intraplaque staining for vWF was present in acellular areas, as indicated by DAPI counter-staining. A fairly intact internal elastic lamina may suggest the primary cell types are circulating monocytes and proliferating endothelial cells and not smooth muscle cells.

Variation in stiffness can be accurately mapped onto the mosaic of AFM images of the tested plaque surface [**Fig. 6.2(B)**, **Fig. 6.3**]. The plaque sample adjacent to the tested surface was used for histology and immunofluorescence. Histological processing

requires a loss of approximately 100 microns from the sample. Therefore slight geometrical differences arise due to the physical gap between the tested plaque surface and the stained plaque surface. After resizing, however, the histological sample generally aligned with the AFM image [**Fig. 6.3**]. **Figure 6.3** shows a representative plaque from a 45.6 week old male ApoE-/- mouse. All the asymptotic pointwise moduli were below 10 kPa, except at 2 locations near the plaque cap on the right, where the values were 15 and 27 kPa.

Stiffness values were also found for the aortic wall in wild-type and heterozygous mice of the same background as the ApoE-/- mice. **Figure 6.4** shows the natural log transformation of all the asymptotic stiffness values acquired over the normal aortic wall (unloaded and loaded). The actual asymptotic stiffness values display as a left skewed distribution [**Fig. 6.4 (A), (C)**]. The median stiffness value of the actual data corresponds to the back transformed value of the natural log mean. Comparing all of the stiffness values from the unloaded and loaded walls shows that the unloaded group is significantly stiffer (axially in compression) with median values of 18.7 and 11.4 kPa, respectively ($p = 0.0015$). Stiffness of the unpressurized walls exhibits a predominately right-skewed distribution with a long tail. Stiffness distribution of the pressured wall is more bimodal, with median values of 9.8 and 76.7 kPa.

FIGURE 6.2. (**A**) Point-wise modulus versus indentation depth (symbols) and the calculated asymptotic stiffness (solid line) are shown on the same scale (0-15 kPa for the modulus and 0-200 nm for depth). (**B**) Overlaid topographical images, acquired via the inverted optical microscope and CCD camera, detail the outline of the opaque ApoE-/- plaque, arterial wall, mechanically tested locations, and asymptotic pointwise modulus value at these locations. (**C**) Histological examination of the face adjacent to the one tested reveals a lipid laden (ORO) cellular plaque with no calcifications (Von Kossa). This plaque appears fairly collagenous (TRI) with fragmentation and straightening of the elastic lamina (VVG). Cells in the plaque and adjacent wall take on a less contractile phenotype (SMA). Endothelial cells line the luminal surface (vWF) as well as regional intraplaque expression.

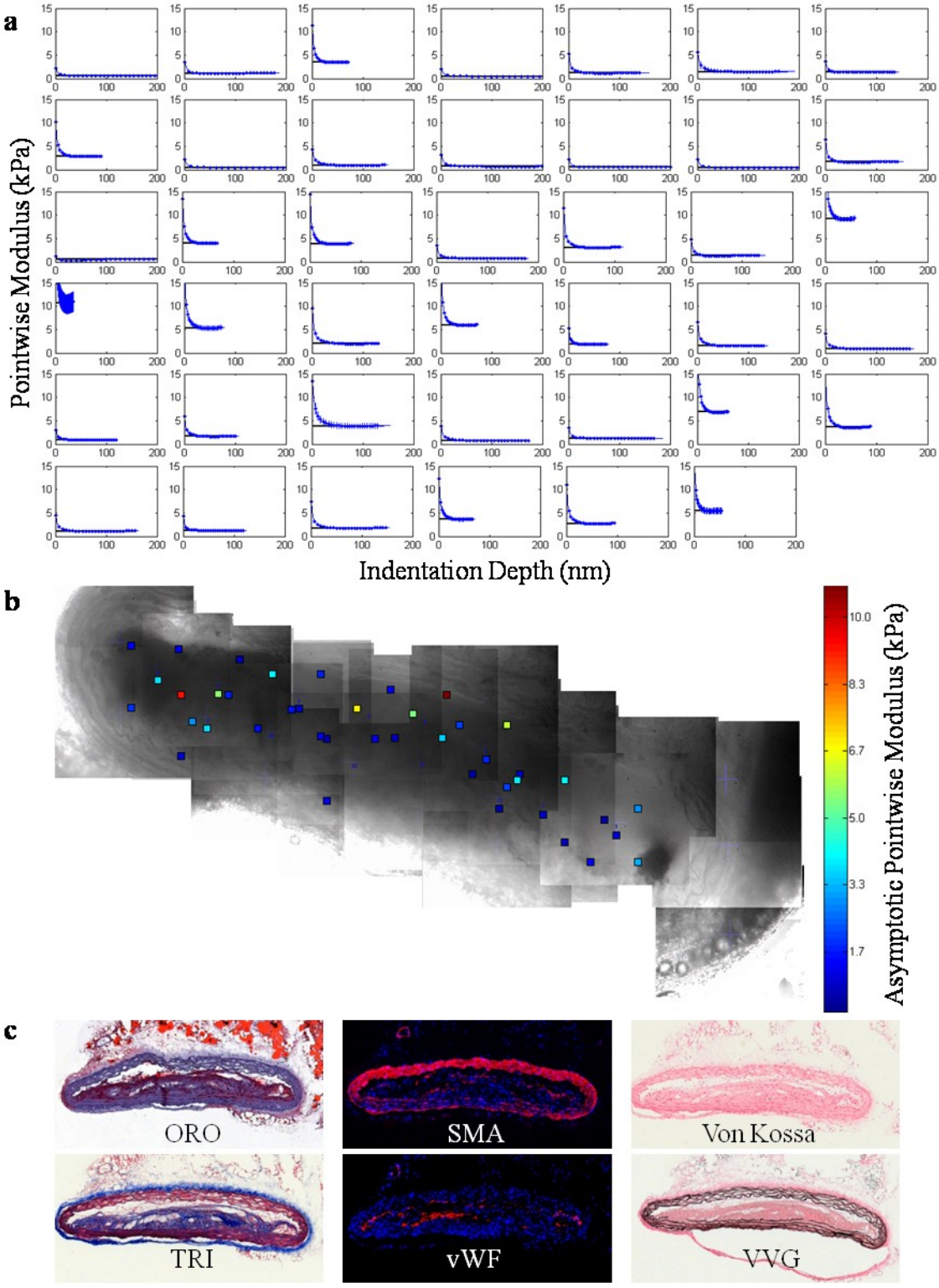

FIGURE 6.2. continued.

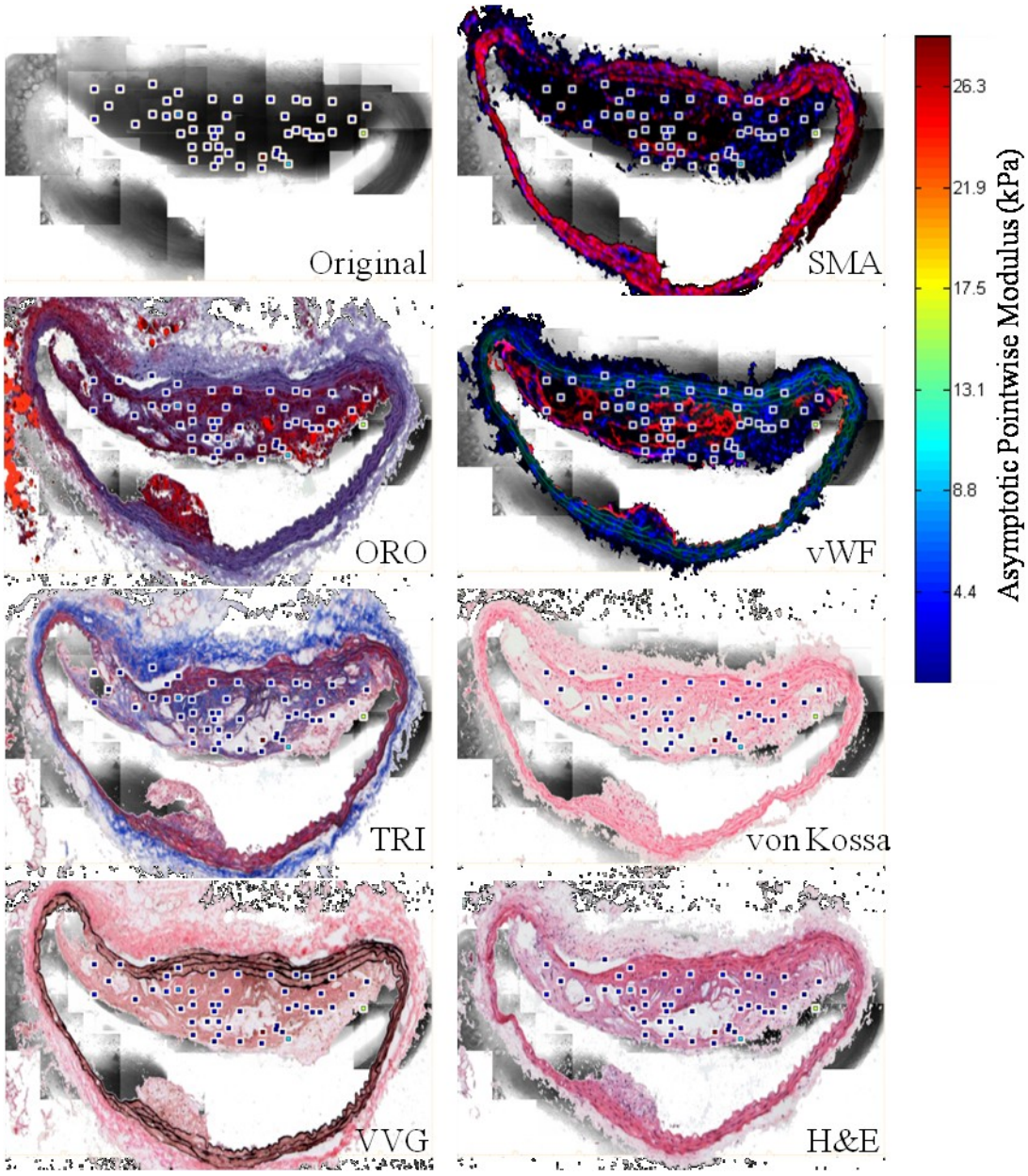

FIGURE 6.3. Representative plaque overlay showing the mechanically tested locations and there stiffness values mapped over the histology samples and the original AFM image. The original AFM image is displayed in the upper left corner followed by the various histological stains overlaid (i.e. Oil Red O (ORO), alpha smooth muscle actin (SMA), von Kossa, hemotoxylin and eosin (H&E), von Willebrand Factor (vWF), Verhoeff-van Gieson (VVG), and Massons trichrome (TRI).

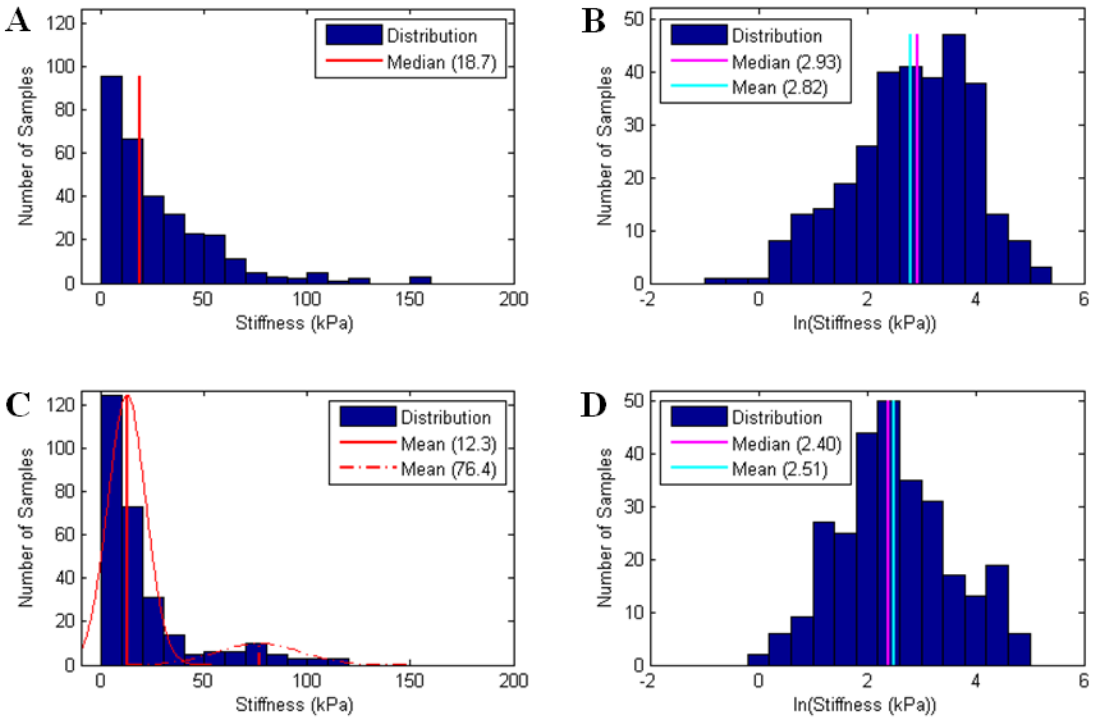

FIGURE 6.4. Histograms of the asymptotic axial compressive stiffness over the wall of (**A, B**) unloaded (n = 25 animals) and (**C, D**) pressurized to ~100 mmHg (n = 16 animals) normal arteries. (**A, C**) Distributions of stiffness were originally right-skewed (bin size of 20 kPa, skewness of 8.6 and 3.2 for unloaded and loaded respectively); (**B, D**) after a natural log transformation, the distributions are Gaussian (bin size of 0.4, skewness of -0.3 and 0.3 for unloaded and loaded respectively). (**C**) The normal distribution constructed from the mean and standard deviations is outlined in red for the softer and stiffer populations of the pressurized aortas, respectively. Compressive axial stiffness of the unloaded wall is statistically different from the pressurized wall (unpaired two-sample t-test, $p = 0.00042$).

For all plaques, 85.6% of the asymptotic stiffness values were below 5 kPa. **Figure 6.5** shows the stiffness of the plaque compared to the normal wall. The maximum stiffness value from all plaques is 37.2 kPa; the small cluster near this value, with median stiffness of 24.3 kPa, is attributable to a calcified region from a single 56 week female plaque out of the 18 plaques examined. Collagen is present in these

plaques; however, collagen does not seem to have a significant effect on the axial compressive stiffness. Lack of increased stiffness may be due to the altered organization, cross-linking, or lower density of collagen fibrils present in these plaques. Moreover, the plaque materials from the 18 plaques studied herein appeared more mixed or homogeneous with the predominate one being lipid-ladened.

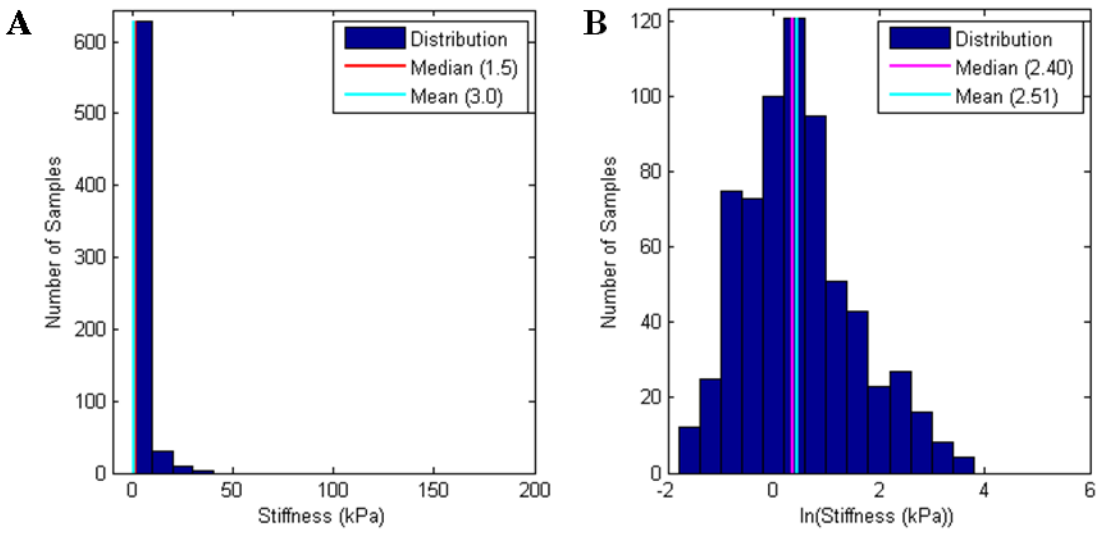

FIGURE 6.5. Histograms of the asymptotic axial stiffness values of plaques (n = 18 plaques, n = 12 animals). (**A**) Originally the distributions were right-skewed (inlay) (bin size 5 kPa, skewness of 5.36); (**B**) after a natural log transformation the distribution is Gaussian (bin size 0.2, skewness of 0.58). Axial stiffness of plaques are statistically different than normal wall (unloaded, unpaired two-sample t-test, $p < 0.0001$; pressurized, unpaired two-sample t-test, $p < 0.0001$).

In the wall of the pressurized artery of the control mice there appeared to be at least two mechanically different materials. **Figure 6.6** shows the two populations of material stiffness observed in pressurized arteries. Through a cumulative distribution display of the empirical pressurized stiffness we see there is a population that deviates

from normality [**Fig. 6.6**]. Likewise, computing the probability density estimate based on a normal kernel function with a bandwidth of 0.25 illustrates a second stiffness population. Separating these populations at 43 kPa and plotting Gaussian distributions based on their standard mean errors, 12.3 ± 0.59 kPa and 76.4 ± 3.22 kPa for the softer and stiffer populations, respectively is shown in **Figure 6.3(C)**.

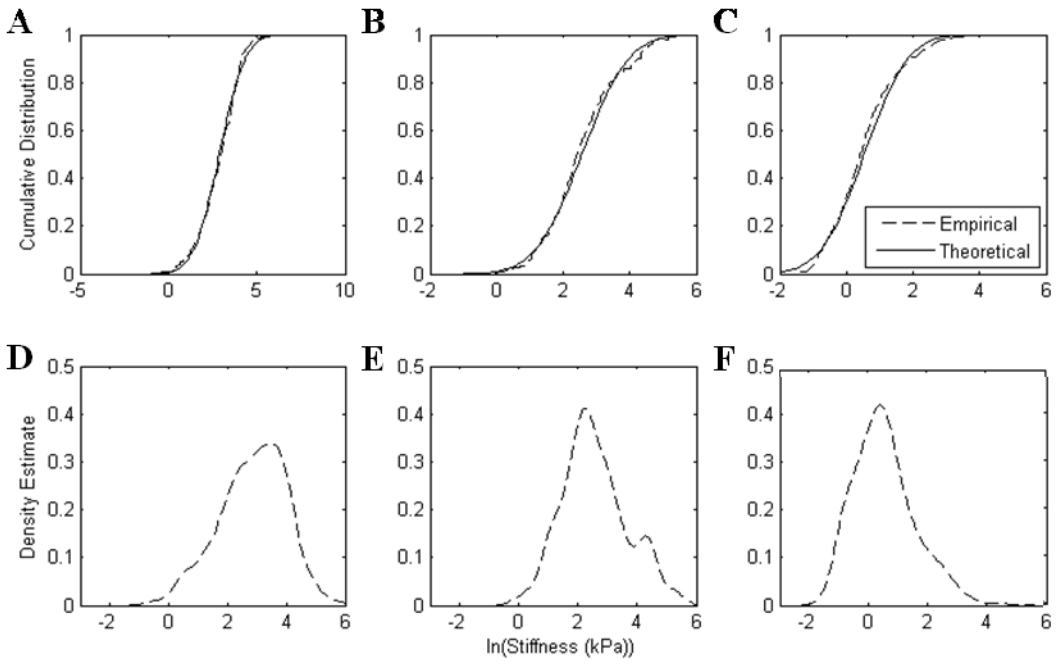

FIGURE 6.6. The empirical cumulative distribution of the natural log transformed asymptotic stiffness of (**A**) unloaded arteries, (**B**) loaded arteries and, (**C**) plaques are shown by dashed curves. (**A, B, C**) The normal cumulative distributions for each case are shown by solid curves. (**D, E, F**) The kernel smoothed density estimate based on a normal kernel function further suggests a second stiffness population in (**E**), the loaded case. For the loaded wall, the disparate stiffnesses are between approximately 43 and 150 kPa. The peaks of the density estimates are thus 34.5 kPa for the unloaded wall, 9.1 and 71.0 kPa for the loaded wall and, 1.4 kPa for the plaque.

Figure 6.7 shows that plaques from males and females are not statistically different. Both genders range from 42 to 56 weeks with slightly more plaques tested from females than males, $n = 11$ and $n = 7$, respectively. Males and females both had fairly large lipid laden plaques with median stiffness of around 1.45 kPa.

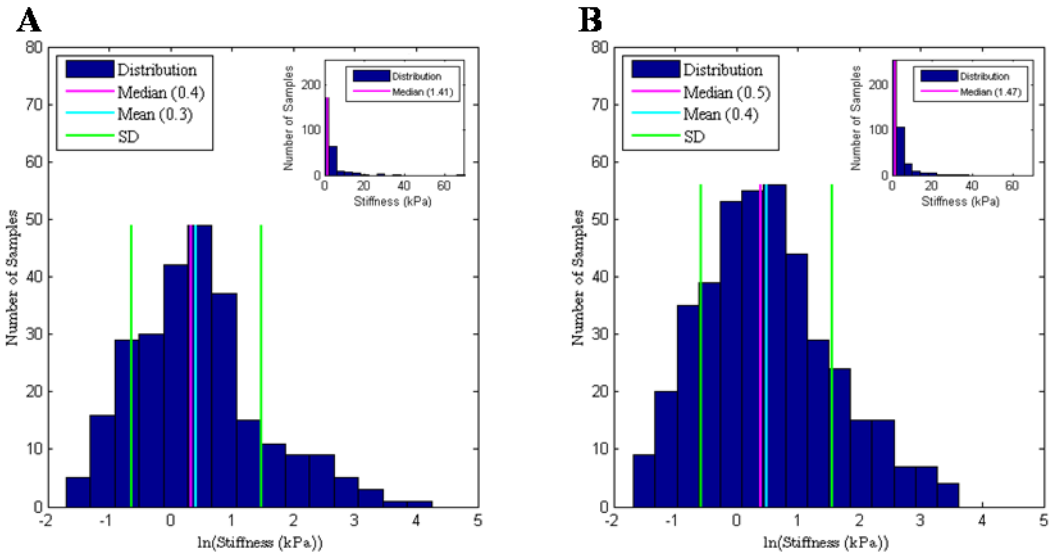

FIGURE 6.7. Stiffness from all (**A**) male and (**B**) female plaques. The median value was (**A, right inlay**) 1.41 kPa for male plaques and (**B, right inlay**) 1.47 kPa for female plaques. Using the log transformation to compare these distributions revealed they were not statistically different ($p = 0.33$, unpaired two-sample t-test).

Discussion

Using a 5-µm diameter spherical AFM tip, we were able to quantify regional material properties within cross-sections of atherosclerotic plaques from the suprarenal aorta of ApoE-/- mice. The size of the tip was chosen to allow an averaged response of the mechanical properties without compromising the specificity of individual structural components within the atherosclerotic plaque. Previous techniques used to characterize

plaque components include uniaxial testing of 31.7 x 1.2 mm^2 human aortic intimal plaques lumped into 3 categories (i.e. cellular, hypocellular, and calcified; [189]), cyclic compression and stress-relaxation testing on 5 x 5 mm^2 plaque samples [190], and torsional rheometer testing on synthesized lipid pools 0.3 to 1 mm thick [189]. Each of these techniques required either synthesizing plaque material or removing the plaque from its natural configuration and treating it as a homogenized (lumped) material. Yet, the complexity in geometry and composition (fibrous tissue, fatty substances, smooth muscle cells, elastin fragments, and calcium deposits) demands methods that can discriminate better the individual contributions of the different constituents. Indeed, stress analyses reveal that perhaps the most important aspect of plaque properties may be material discontinuities – that is, the close proximity of stiff and compliant materials, which lead to stress concentrations [176].

The plaques from ApoE-/- mice studied here consisted primarily of large lipid laden pools having an associated median stiffness of 1.5 kPa and thin cap. Moreover these plaques were not ruptured before testing. Plaque rupture is a complex mechanical process dictated by plaque composition and morphology as well as the applied loads. Using computational models, Finet et al. (2007) [191] show that a slight increase in stiffness in a lipid core (from 1 kPa to 2-30 kPa) results in mechanically stable plaques (where the peak cap stress is brought below the 300 kPa threshold assumed for rupture of collagen). Using computational stress analyses, Vengrenyuk et al. (2010) [186] calculated peak circumferential stress in non-ruptured ApoE-/- plaques to be higher than the estimated rupture threshold of humans (minimum 300 kPa, average 545 kPa).

Therefore, despite having a thin cap and large lipid pool, the lack of rigid inclusions (calcification) was suggested to render the plaques relatively stable.

Despite a lack of information on exact mechanisms and signaling pathways for force sensing and transduction, it is now evident that cells sense the stiffness and geometric features of their substrates and respond accordingly [4, 192-195]. It has been proposed, nonetheless, that a cell can sense its mechano-environment through local adhesions (e.g., cadherins or integrins) by measuring either the strength or displacement of these adhesions by a given force [4, 192]. Cells respond to their environment through integrin clustering, strengthening of integrin-cytoskeleton linkages, biochemical signaling, and even remodeling of the extracellular matrix [4, 192, 193]. Moreover, cells can change their morphology (e.g., round for soft and spread out for stiff substrates), cytoskeletal organization (around the perimeter for soft and at focal adhesions for stiff), and stiffness (within a range) based on that of the substrate [2, 192, 193, 195]. Matrix stiffness also aids in proper differentiation of mesenchymal stem cells [196]. Because cells control the properties of evolving atherosclerotic plaques, it is thus important to know regional plaque mechanical properties which influence the associated adherent cell responses.

The main structural components of a normal aorta are collagen, elastin, and SMCs, in order of decreasing stiffness. For example, using a scanning micro-indentation tester, Masumoto et al. (2004) [197] found the radial stiffness of the elastic lamina and smooth muscle layer of an unloaded porcine aorta to be 180 and 50 kPa, respectively. Oie et al. (2009) [198] used a tactile mapping system and found the axial stiffness of the

media (comprised of SMCs and collagen fibrils) to be 17.0 ± 9.0 (mean ± SD) kPa and that of elastin to be 69.0 ± 12.8 kPa. In contrast, Young's moduli of water-swelled collagen sheets having collagen concentrations of 12% or 41% were found to be 137.6 ± 32.2 and 426.8 ± 136.4 kPa, respectively. Moreover, other groups report collagen to be ~1000 times stiffer than elastin [199]. Oie et al. (2009) [198] thus suggest that the medial stiffness 17.0 ± 9.0 kPa results from a low density of collagen. Recalling that one possible function of collagen in a pressurized artery is to limit over-distension during transient over-loading, thus protecting elastin and SMCs from damage, collagen probably contributes little to the overall stress-strain response of the aorta at low pressures. Indeed, previous studies suggest that collagen fibers contribute minimally to residual stresses (or strains) [200]. At high pressures, however, collagen fibers straighten and carry much of the intramural load [83, 199].

The bimodal distribution of axial stiffness revealed by **Figures 6.4** and **6.6**, with medians of 9.7 and 76.7 kPa, may similarly suggest two material populations within the modestly pressurized normal aortic wall. Albeit not statistically significant, a plot of stiffness versus location reveals most stiff values lie within the inner two-thirds of the aortic wall. This observation suggests the stiffer population may be due to elastin, since collagen primarily resides in the adventitia and elastin in the media. Costa et al. (2006) [188] also reported a bimodal distribution of stiffness for individual cells. Whereas they used nanometer-diameter tips, able to distinguish cytoskeletal filaments (5.6 ± 3.5 kPa) and cytoplasm (1.5 ± 0.76 kPa), we used a micron-diameter tips and were able to distinguish material within the smooth muscle layer (thickness 10.1 ± 4.7 μm, mean ±

SD) from the elastic laminae (thickness 6.2 ± 2.1 μm) in an unloaded wall section (total thickness 136.6 ± 22.9 μm). Excluding the upper 5 % due to a small cluster of stiffness values at ~175 kPa, stiffness ranged from 0.5 to 90 kPa with a median of 18.9 kPa for the unloaded aorta. In agreement with previously reported material properties, we suggest that the upper range is due to elastin, the middle range due to a mixture of SMC and unloaded collagen, and the lower range may reflect cytoplasmic material. In the samples with a fixed pressure of 100 mmHg, analyses indicated two significantly different populations of material with moduli of 12.3 ± 0.59 and 76.4 ± 3.22 kPa. Yet similar to the unloaded case, excluding the upper 5 %, stiffness ranged from 0.8 to 94 kPa with a median of 11 kPa for the pressurized aorta. We suggest the dichotomy in material populations that arose when the vessels were pressurized may have been due to an increase of lamina stiffening resulting from elastin straightening. Of course, circumferentially oriented fibers (e.g., collagen and elastin) may not be load-bearing in the unpressurized samples.

In plaques, cell contractility appeared to be absent in soft regions as indicated by the lack of αSMA staining. Rather, these plaques appeared to be dominated by lipids, with over 90% of the asymptotic values of stiffness less than 10 kPa [**Fig. 6.5**]. The correlation between the cell function (i.e., contractility) modulated by environmental stiffness has been previously observed. For instance, minimal stress fibers form in cells grown on soft surfaces (Young's modulus of 10 kPa) whereas many stress fibers form on stiff surfaces (Young's modulus of 100 kPa) [201, 202]. We also found, at the tissue level, the mixture of collagen, elastin, and SMCs in the wall of a normal aorta had a

compressive axial stiffness around 18.9 kPa, which is well above that of the lipid laden plaques. Histology confirmed high lipid content in the plaques as well as straightening and fragmentation of the elastic lamina, a low collagen content, a faint layer of contractile cells on the luminal face, with expression of vWF lining the lumen [**Fig. 6.2**]. Thus without cell contractility and much of the structural matrix proteins that reside in the wall of normal arteries, stiffness values appeared to be dominated by lipids abundant in the plaques.

Interestingly, calcification in the intimal space is typical of advanced lesions in humans. In the ApoE -/- mice tested, only one of the 18 lesions exhibited even minimal calcification. Therefore, to better represent the heterogeneity of lesions seen in human plaques in aortic lesions within the ApoE-/- mouse population (fed a western diet) additional measures could be taken. For example, dietary supplements of vitamin D, calcium, or warfarin have been shown to increase vascular calcification (Atkinson, 2008). In addition, SMC apoptosis as well as matrix Gla protein (MGP) and osteoprotegerin (OPG) deficient models have also been shown to increase vascular calcification ([203-205], respectively).

CHAPTER VII

CONCLUSIONS

In Chapter III we introduce a novel Agent Based Model (ABM) of which was designed to be coupled with the Constrained Mixture Model (CMM). A semi-objective scoring regime is introduced as a means to gain confidence in the ABM rules derived from the literature. A parameter sensitivity analysis was performed on the ABM parameters in order to determine proper bounds. Lastly we showed the ABM and CMM are stable in homeostatic conditions amongst transient blips in blood pressure. Chapter IV applies the CMM and ABM to predict arterial changes in biochemical concentration as well as salient features such as geometry, mass of elastin, smooth muscle, and collagen, and circumferential stress, in response to hypertension. These predictions seem to be within the range of experimental finding. Thus we established the foundation of these models, which can be extended through model coupling to create a fully multi-scale model.

In Chapter V we used an aortic coarctation model of hypertension to quantify the arterial responses to hypertension. We found the changes in artery structure as a response to sustained elevated blood pressure differs in the aorta, coronary and cerebral arteries. Overall tissue maintenance seems to occur first in the aorta, thickening in the coronary, and little change in the cerebral. In summary, over the 8 week time course, the aorta thickens, loses contractility, and recruits hematopoietic progenitor cells and monocytes at week 2. At week 4 the relative collagen content in the aorta goes up. By

week 8 the collagen content and thickness are still up, however the contractility is back to normal. In the aorta there was little change of the inner radius, cell density or elastin throughout the 8 weeks. In the coronary, by 2 weeks not only had the thickness increased but the inner radius had also increased. At week 4 the density of hematopoietic progenitor cells and monoctyes, in the coronary, had increased. By 8 weeks the thickness, inner radius and contractile fibers are still up. In the coronary there was little change in the relative cell density, collagen and elastin content. Unlike the aorta and coronary arteries there was little significant change in the cerebral artery. The contractility slightly decreased at weeks 6 and 8, and the cell density decreased at week 6, but these metrics returned to normal by 8 weeks. It is worthwhile to note that common to all the arteries the packing density (or nuclei/area) and elastin remained nearly the same at all time points.

In conclusion, the onset and progression of arterial remodeling is artery and location dependent. That is, the remodeling may also depend on the variations within the artery type (e.g. the coronary and cerebral are both “muscular” arteries but even at normalcy the structure and ratio of elastin, collagen and muscle are different) as well as variation between arteries types. In addition, depending on the location the environment, loads, tethering, etc. may be vastly different. Therefore, the work presented in Chapter V brings us one step closer to understanding sources of mass accumulation and the time progression of arterial remodeling to elevated blood pressure.

In Chapter VI, we proposed a novel technique for testing and quantifying the material behavior of plaques ex-vivo. Out of the 18 plaques examined, 15 were highly

lipid laden, 2 were more fibrotic, and only one of the fibrotic plaques showed slight calcification. The results suggest a median axial compressive stiffness value of 1.5 kPa for the lipid regions in plaques. Regional mechano-morphological information of plaques is essential for computational analysis. However, for the most part ApoE-/- plaques appear to lack distinct material heterogeneity. Microcalcified fibrotic plaques need to be induced for aortic ApoE-/- plaques to be considered a representative model for human plaques. The work presented here narrows the knowledge gap on the connection between the structure and mechanical properties of plaques and the normal aortic wall.

REFERENCES

[1] Bershadsky A, Kozlov M, Geiger B. Adhesion-mediated mechanosensitivity: A time to experiment, and a time to theorize. Curr Opin Cell Biol 2006;18:472-481.

[2] Engler AJ, Griffin MA, Sen S, Bonnemann CG, Sweeney HL, Discher DE. Myotubes differentiate optimally on substrates with tissue-like stiffness: Pathological implications for soft or stiff microenvironments. J Cell Biol 2004;166:877-887.

[3] Georges PC, Janmey PA. Cell type-specific response to growth on soft materials. J Appl Physiol 2005;98:1547-1553.

[4] Vogel V, Sheetz M. Local force and geometry sensing regulate cell functions. Nat Rev Mol Cell Biol 2006;7:265-275.

[5] Holzapfel G, Gasser T, Ogden R. A new constitutive framework for arterial wall mechanics and a comparative study of material models. J Elast 2000;61:1-48.

[6] Clark JM, Glagov S. Transmural organization of the arterial media. The lamellar unit revisited. Arteriosclerosis 1985;5:19-34.

[7] Leung DY, Glagov S, Mathews MB. Elastin and collagen accumulation in rabbit ascending aorta and pulmonary trunk during postnatal growth. Correlation of cellular synthetic response with medial tension. Circ Res 1977;41:316-323.

[8] Wolinsky H, Glagov S. A lamellar unit of aortic medial structure and function in mammals. Circ Res 1967;20:99-111.

[9] Hu JJ, Fossum TW, Miller MW, Xu H, Liu JC, Humphrey JD. Biomechanics of the porcine basilar artery in hypertension. Ann Biomed Eng 2006;35:19-29.

[10] Fernandez D, Crane WA. New cell formation in rats with accelerated hypertension due to partial aortic constriction. J Pathol 1970;100:307-316.

[11] Ross R. The pathogenesis of atherosclerosis: A perspective for the 1990s. Nature 1993;362:801-809.

[12] Ueno H, Kanellakis P, Agrotis A, Bobik A. Blood flow regulates the development of vascular hypertrophy, smooth muscle cell proliferation, and endothelial cell nitric oxide synthase in hypertension. Hypertension 2000;36:89-96.

[13] Zhou X, Beck C, Boren J, Akyurek LM. Diverse origin of vascular smooth muscle cells in the neointima. Anadolu Kardiyol Derg 2005;5:216-220.

[14] Arciniegas E, Sutton AB, Allen TD, Schor AM. Transforming growth factor beta 1 promotes the differentiation of endothelial cells into smooth muscle-like cells in vitro. J Cell Sci 1992;103 (Pt 2):521-529.

[15] Frid MG. Mature vascular endothelium can give rise to smooth muscle cells via endothelial-mesenchymal transdifferentiation: In vitro analysis. Circ Res 2002;90:1189-1196.

[16] Capers Qt, Alexander RW, Lou P, De Leon H, Wilcox JN, Ishizaka N, Howard AB, Taylor WR. Monocyte chemoattractant protein-1 expression in aortic tissues of hypertensive rats. Hypertension 1997;30:1397-1402.

[17] Fossum TW, Baltzer WI, Miller MW, Aguirre M, Whitlock D, Solter P, Makarski LA, McDonald MM, An M-Y, Humphrey JD. A novel aortic coarctation model for studying hypertension in the pig. J Invest Surg 2003;16:35-44.

[18] Connolly HM, Huston J, 3rd, Brown RD, Jr., Warnes CA, Ammash NM, Tajik AJ. Intracranial aneurysms in patients with coarctation of the aorta: A prospective magnetic resonance angiographic study of 100 patients. Mayo Clin Proc 2003;78:1491-1499.

[19] Campbell M. Natural history of coarctation of the aorta. Heart 1970;32:633-640.

[20] Dedivitiis M, Rubba P, Calabro R. Arterial hypertension and cardiovascular prognosis after successful repair of aortic coarctation: A clinical model for the study of vascular function. Nutr Metab Cardiovasc Dis 2005;15:382-394.

[21] Eerola A, Jokinen E, Boldt T, Mattila IP, Pihkala JI. Left ventricular hypertrophy persists after successful treatment for coarctation of the aorta. Scand Cardiovasc J 2007;41:370-377.

[22] Reifenstein GH, Levine SA, Gross RE. Coarctation of the aorta; a review of 104 autopsied cases of the adult type, 2 years of age or older. Am Heart J 1947;33:146-168.

[23] Sloop GD. Insights into the relationship of fatty streaks to raised atherosclerotic lesions provided by the hemorheologic-hemodynamic theory of atherosclerotic lesions provided by the hemorheologic-hemodynamic theory of atherogenesis. Med Hypotheses 1998;51:385-388.

[24] Nakashima Y, Plump AS, Raines EW, Breslow JL, Ross R. Apoe-deficient mice develop lesions of all phases of atherosclerosis throughout the arterial tree. Arterioscler Thromb 1994;14:133-140.

[25] Zhang SH, Reddick RL, Burkey B, Maeda N. Diet-induced atherosclerosis in mice heterozygous and homozygous for apolipoprotein e gene disruption. J Clin Invest 1994;94:937-945.

[26] Choudhury RP, Fayad ZA, Aguinaldo JG, Itskovich VV, Rong JX, Fallon JT, Fisher EA. Serial, noninvasive, in vivo magnetic resonance microscopy detects the development of atherosclerosis in apolipoprotein e-deficient mice and its progression by arterial wall remodeling. J Magn Reson Imaging 2003;17:184-189.

[27] Zhao X, Pratt R, Wansapura J. Quantification of aortic compliance in mice using radial phase contrast mri. J Magn Reson Imaging 2009;30:286-291.

[28] O'Rourke MF, Staessen JA, Vlachopoulos C, Duprez D, Plante GéE. Clinical applications of arterial stiffness; definitions and reference values. Am J Hypertens 2002;15:426-444.

[29] Leung DY, Glagov S, Mathews MB. Cyclic stretching stimulates synthesis of matrix components by arterial smooth muscle cells in vitro. Science 1976;191:475-477.

[30] Boutouyrie P, Bussy C, Lacolley P, Girerd X, Laloux B, Laurent S. Association between local pulse pressure, mean blood pressure, and large-artery remodeling. Circulation 1999;100:1387-1393.

[31] Eberth JF, Gresham VC, Reddy AK, Popovic N, Wilson E, Humphrey JD. Importance of pulsatility in hypertensive carotid artery growth and remodeling. J Hypertens 2009;27:2010-2021.

[32] Davies PF, Mundel T, Barbee KA. A mechanism for heterogeneous endothelial responses to flow in vivo and in vitro. J Biomech 1995;28:1553-1560.

[33] Passerini A. Shear stress magnitude and directionality modulate growth factor gene expression in preconditioned vascular endothelial cells. J Vasc Surg 2003;37:182-190.

[34] Frangos JA, Eskin SG, McIntire LV, Ives CL. Flow effects on prostacyclin production by cultured human endothelial cells. Science 1985;227:1477-1479.

[35] Himburg HA, Dowd SE, Friedman MH. Frequency-dependent response of the vascular endothelium to pulsatile shear stress. Am J Physiol Heart Circ Physiol 2007;293:H645-653.

[36] Humphrey JD. Mechanisms of arterial remodeling in hypertension: Coupled roles of wall shear and intramural stress. Hypertension 2008;52:195-200.

[37] Humphrey JD, Rajagopal KR. A constrained mixture model for arterial adaptations to a sustained step change in blood flow. Biomech Model Mechanobiol 2003;2:109-126.

[38] Baek S, Rajagopal KR, Humphrey JD. A theoretical model of enlarging intracranial fusiform aneurysms. J Biomech Eng 2006;128:142-149.

[39] Baek S, Valentin A, Humphrey JD. Biochemomechanics of cerebral vasospasm and its resolution: Ii. Constitutive relations and model simulations. Ann Biomed Eng 2007;35:1498-1509.

[40] Gleason RL, Humphrey JD. A mixture model of arterial growth and remodeling in hypertension: Altered muscle tone and tissue turnover. J Vasc Res 2004;41:352-363.

[41] Gleason RL, Jr., Humphrey JD. A 2d constrained mixture model for arterial adaptations to large changes in flow, pressure and axial stretch. Math Med Biol 2005;22:347-369.

[42] Valentin A, Cardamone L, Baek S, Humphrey JD. Complementary vasoactivity and matrix remodelling in arterial adaptations to altered flow and pressure. J R Soc Interface 2009;6:293-306.

[43] Li Q, Muragaki Y, Hatamura I, Ueno H, Ooshima A. Stretch-induced collagen synthesis in cultured smooth muscle cells from rabbit aortic media and a possible involvement of angiotensin ii and transforming growth factor-beta. J Vasc Res 1998;35:93-103.

[44] Peirce SM, Price RJ, Skalak TC. Spatial and temporal control of angiogenesis and arterialization using focal applications of vegf164 and ang-1. Am J Physiol Heart Circ Physiol 2004;286:H918-925.

[45] Zhang L, Athale CA, Deisboeck TS. Development of a three-dimensional multiscale agent-based tumor model: Simulating gene-protein interaction profiles, cell phenotypes and multicellular patterns in brain cancer. J Theor Biol 2007;244:96-107.

[46] Bentley K, Mariggi G, Gerhardt H, Bates PA. Tipping the balance: Robustness of tip cell selection, migration and fusion in angiogenesis. PLoS Comput Biol 2009;5:e1000549.

[47] Lanir Y. Constitutive equations for fibrous connective tissues. J Biomech 1983;16:1-12.

[48] Wagenseil JE, Mecham RP. New insights into elastic fiber assembly. Birth Defects Res C Embryo Today 2007;81:229-240.

[49] Wolinsky H. Effects of hypertension and its reversal on the thoracic aorta of male and female rats. Morphological and chemical studies. Circ Res 1971;28:622-637.

[50] Rizvi MA, Katwa L, Spadone DP, Myers PR. The effects of endothelin-1 on collagen type i and type iii synthesis in cultured porcine coronary artery vascular smooth muscle cells. J Mol Cell Cardiol 1996;28:243-252.

[51] Rizvi MA, Myers PR. Nitric oxide modulates basal and endothelin-induced coronary artery vascular smooth muscle cell proliferation and collagen levels. J Mol Cell Cardiol 1997;29:1779-1789.

[52] Valentin A, Humphrey JD. Parameter sensitivity study of a constrained mixture model of arterial growth and remodeling. J Biomech Eng 2009;131:101006.

[53] Valentin A, Humphrey JD. Evaluation of fundamental hypotheses underlying constrained mixture models of arterial growth and remodelling. Philos Transact A Math Phys Eng Sci 2009;367:3585-3606.

[54] Battistini B, Chailler P, D'Orleans-Juste P, Briere N, Sirois P. Growth regulatory properties of endothelins. Peptides 1993;14:385-399.

[55] Yoshizumi M, Kurihara H, Sugiyama T, Takaku F, Yanagisawa M, Masaki T, Yazaki Y. Hemodynamic shear stress stimulates endothelin production by cultured endothelial cells. Biochem Biophys Res Commun 1989;161:859-864.

[56] Reidy MA. Growth factors and arterial smooth muscle cell proliferation. Ann N Y Acad Sci 1994;714:225-230.

[57] Stegemann JP, Nerem RM. Altered response of vascular smooth muscle cells to exogenous biochemical stimulation in two- and three-dimensional culture. Exp Cell Res 2003;283:146-155.

[58] Chapman GB, Durante W, Hellums JD, Schafer AI. Physiological cyclic stretch causes cell cycle arrest in cultured vascular smooth muscle cells. Am J Physiol Heart Circ Physiol 2000;278:H748-754.

[59] Li Z, Moore S, Alavi MZ. Mitogenic factors released from smooth muscle cells are responsible for neointimal cell proliferation after balloon catheter deendothelialization. Exp Mol Pathol 1995;63:77-86.

[60] Ma YH, Ling S, Ives HE. Mechanical strain increases pdgf-b and pdgf beta receptor expression in vascular smooth muscle cells. Biochem Biophys Res Commun 1999;265:606-610.

[61] Mata-Greenwood E, Grobe A, Kumar S, Noskina Y, Black SM. Cyclic stretch increases vegf expression in pulmonary arterial smooth muscle cells via tgf-beta1 and reactive oxygen species: A requirement for nad(p)h oxidase. Am J Physiol Lung Cell Mol Physiol 2005;289:L288-289.

[62] Morishita R, Gibbons GH, Horiuchi M, Kaneda Y, Ogihara T, Dzau VJ. Role of ap-1 complex in angiotensin ii-mediated transforming growth factor-beta expression and growth of smooth muscle cells: Using decoy approach against ap-1 binding site. Biochem Biophys Res Commun 1998;243:361-367.

[63] Karakiulakis G, Papakonstantinou E, Aletras AJ, Tamm M, Roth M. Cell type-specific effect of hypoxia and platelet-derived growth factor-bb on extracellular matrix turnover and its consequences for lung remodeling. J Biol Chem 2007;282:908-915.

[64] Owens GK, Rabinovitch PS, Schwartz SM. Smooth muscle cell hypertrophy versus hyperplasia in hypertension. Proc Natl Acad Sci U S A 1981;78:7759-7763.

[65] Kim YS, Galis ZS, Rachev A, Han HC, Vito RP. Matrix metalloproteinase-2 and -9 are associated with high stresses predicted using a nonlinear heterogeneous model of arteries. J Biomech Eng 2009;131:011009.

[66] Okuno T, Andoh A, Bamba S, Araki Y, Fujiyama Y, Fujiyama M, Bamba T. Interleukin-1beta and tumor necrosis factor-alpha induce chemokine and matrix metalloproteinase gene expression in human colonic subepithelial myofibroblasts. Scand J Gastroenterol 2002;37:317-324.

[67] Garcia-Lopez G, Vadillo-Ortega F, Merchant-Larios H, Maida-Claros R, Osorio M, Soriano-Becerril D, Flores-Herrera H, Beltran-Montoya J, Garfias-Becerra Y, Zaga-Clavellina V. Evidence of in vitro differential secretion of 72 and 92 kda

type iv collagenases after selective exposure to lipopolysaccharide in human fetal membranes. Mol Hum Reprod 2007;13:409-418.

[68] Kim YJ, Sah RL, Doong JY, Grodzinsky AJ. Fluorometric assay of DNA in cartilage explants using hoechst 33258. Anal Biochem 1988;174:168-176.

[69] Schlumberger W, Thie M, Rauterberg J, Robenek H. Collagen synthesis in cultured aortic smooth muscle cells. Modulation by collagen lattice culture, transforming growth factor-beta 1, and epidermal growth factor. Arterioscler Thromb 1991;11:1660-1666.

[70] Absood A, Furutani A, Kawamura T, Graham LM. A comparison of oxidized ldl-induced collagen secretion by graft and aortic smcs: Role of pdgf. Am J Physiol Heart Circ Physiol 2004;287:H1200-1206.

[71] Kanai AJ, Strauss HC, Truskey GA, Crews AL, Grunfeld S, Malinski T. Shear stress induces atp-independent transient nitric oxide release from vascular endothelial cells, measured directly with a porphyrinic microsensor. Circ Res 1995;77:284-293.

[72] Hsieh HJ, Li NQ, Frangos JA. Shear stress increases endothelial platelet-derived growth factor mrna levels. Am J Physiol 1991;260:H642-646.

[73] Aromatario C, Sterpetti AV, Palumbo R, Patrizi AL, Di Carlo A, Proietti P, Guglielmi MB, Cavallaro A, Santoro-D'Angelo L, Cucina A. Fluid shear stress increases the release of platelet derived growth factor bb (pdgf bb) by aortic endothelial cells. Minerva Cardioangiol 1997;45:1-7.

[74] Ziegler T, Bouzourene K, Harrison VJ, Brunner HR, Hayoz D. Influence of oscillatory and unidirectional flow environments on the expression of endothelin and nitric oxide synthase in cultured endothelial cells. Arterioscler Thromb Vasc Biol 1998;18:686-692.

[75] Dancu MB, Berardi DE, Vanden Heuvel JP, Tarbell JM. Asynchronous shear stress and circumferential strain reduces endothelial no synthase and cyclooxygenase-2 but induces endothelin-1 gene expression in endothelial cells. Arterioscler Thromb Vasc Biol 2004;24:2088-2094.

[76] Welgus HG, Jeffrey JJ, Stricklin GP, Roswit WT, Eisen AZ. Characteristics of the action of human skin fibroblast collagenase on fibrillar collagen. J Biol Chem 1980;255:6806-6813.

[77] Welgus HG, Jeffrey JJ, Eisen AZ. The collagen substrate specificity of human skin fibroblast collagenase. J Biol Chem 1981;256:9511-9515.

[78] Xia T, Akers K, Eisen AZ, Seltzer JL. Comparison of cleavage site specificity of gelatinases a and b using collagenous peptides. Biochim Biophys Acta 1996;1293:259-266.

[79] Le J, Dauchot P, Perrot JL, Cambazard F, Frey J, Chamson A. Quantitative zymography of matrix metalloproteinases by measuring hydroxyproline: Application to gelatinases a and b. Electrophoresis 1999;20:2824-2829.

[80] Murphy G, McAlpine CG, Poll CT, Reynolds JJ. Purification and characterization of a bone metalloproteinase that degrades gelatin and types iv and v collagen. Biochim Biophys Acta 1985;831:49-58.

[81] Strauss BH, Robinson R, Batchelor WB, Chisholm RJ, Ravi G, Natarajan MK, Logan RA, Mehta SR, Levy DE, Ezrin AM, Keeley FW. In vivo collagen turnover following experimental balloon angioplasty injury and the role of matrix metalloproteinases. Circ Res 1996;79:541-550.

[82] Faury G, Pezet M, Knutsen RH, Boyle WA, Heximer SP, McLean SE, Minkes RK, Blumer KJ, Kovacs A, Kelly DP, Li DY, Starcher B, Mecham RP. Developmental adaptation of the mouse cardiovascular system to elastin haploinsufficiency. J Clin Invest 2003;112:1419-1428.

[83] Humphrey JD. Cardiovascular solid mechanics: Cells tissues and organs. New York: Springer, 2002.

[84] Maiellaro K, Taylor WR. The role of the adventitia in vascular inflammation. Cardiovasc Res 2007;75:640-648.

[85] Guo X, Kassab GS. Variation of mechanical properties along the length of the aorta in c57bl/6 mice. Am J Physiol Heart Circ Physiol 2003;285:H2614-2622.

[86] Hu Y, Bock G, Wick G, Xu Q. Activation of pdgf receptor alpha in vascular smooth muscle cells by mechanical stress. FASEB J 1998;12:1135-1142.

[87] Reusch P, Wagdy H, Reusch R, Wilson E, Ives HE. Mechanical strain increases smooth muscle and decreases nonmuscle myosin expression in rat vascular smooth muscle cells. Circ Res 1996;79:1046-1053.

[88] Shimizu N, Yamamoto K, Obi S, Kumagaya S, Masumura T, Shimano Y, Naruse K, Yamashita JK, Igarashi T, Ando J. Cyclic strain induces mouse embryonic stem cell differentiation into vascular smooth muscle cells by activating pdgf receptor beta. J Appl Physiol 2008;104:766-772.

[89] Wilson E, Sudhir K, Ives HE. Mechanical strain of rat vascular smooth muscle cells is sensed by specific extracellular matrix/integrin interactions. J Clin Invest 1995;96:2364-2372.

[90] Robertson SH, Smith CK, Langhans AL, McLinden SE, Oberhardt MA, Jakab KR, Dzamba B, DeSimone DW, Papin JA, Peirce SM. Multiscale computational analysis of xenopus laevis morphogenesis reveals key insights of systems-level behavior. BMC Syst Biol 2007;1:46.

[91] Humphrey JD, Taylor CA. Intracranial and abdominal aortic aneurysms: Similarities, differences, and need for a new class of computational models. Annu Rev Biomed Eng 2008;10:221-246.

[92] Langille BL. Remodeling of developing and mature arteries: Endothelium, smooth muscle, and matrix. J Cardiovasc Pharmacol 1993;21 Suppl 1:S11-17.

[93] Lehoux S, Levy BI. Collateral artery growth: Making the most of what you have. Circ Res 2006;99:567-569.

[94] Li S, Huang NF, Hsu S. Mechanotransduction in endothelial cell migration. J Cell Biochem 2005;96:1110-1126.

[95] Greve JM, Les AS, Tang BT, Draney Blomme MT, Wilson NM, Dalman RL, Pelc NJ, Taylor CA. Allometric scaling of wall shear stress from mice to humans: Quantification using cine phase-contrast mri and computational fluid dynamics. Am J Physiol Heart Circ Physiol 2006;291:H1700-1708.

[96] Hu JJ, Baek S, Humphrey JD. Stress-strain behavior of the passive basilar artery in normotension and hypertension. J Biomech 2007;40:2559-2563.

[97] Matsumoto T, Hayashi K. Mechanical and dimensional adaptation of rat aorta to hypertension. J Biomech Eng 1994;116:278-283.

[98] Chuong CJ, Fung YC. On residual stresses in arteries. J Biomech Eng 1986;108:189-192.

[99] Cardamone L, Valentin A, Eberth JF, Humphrey JD. Origin of axial prestretch and residual stress in arteries. Biomech Model Mechanobiol 2009;3:3.

[100] Skalak R. Biophysical approach. Theoretical models of deformability in blood flow. Scand J Clin Lab Invest Suppl 1981;156:55-58.

[101] Rachev A, Stergiopulos N, Meister JJ. Theoretical study of dynamics of arterial wall remodeling in response to changes in blood pressure. J Biomech 1996;29:635-642.

[102] Taber LA. A model for aortic growth based on fluid shear and fiber stresses. J Biomech Eng 1998;120:348-354.

[103] Kuhl E, Maas R, Himpel G, Menzel A. Computational modeling of arterial wall growth. Attempts towards patient-specific simulations based on computer tomography. Biomech Model Mechanobiol 2007;6:321-331.

[104] Hu JJ, Humphrey JD, Yeh AT. Characterization of engineered tissue development under biaxial stretch using nonlinear optical microscopy. Tissue Eng Part A 2009;15:1553-1564.

[105] Humphrey JD. Vascular adaptation and mechanical homeostasis at tissue, cellular, and sub-cellular levels. Cell Biochem Biophys 2008;50:53-78.

[106] Thorne BC, Bailey AM, DeSimone DW, Peirce SM. Agent-based modeling of multicell morphogenic processes during development. Birth Defects Research Part C: Embryo Today: Reviews 2007;81:344-353.

[107] Bailey AM, Thorne BC, Peirce SM. Multi-cell agent-based simulation of the microvasculature to study the dynamics of circulating inflammatory cell trafficking. Ann Biomed Eng 2007;35:916-936.

[108] Gleason RL, Hu JJ, Humphrey JD. Building a functional artery: Issues from the perspective of mechanics. Front Biosci 2004;9:2045-2055.

[109] Na S, Meininger GA, Humphrey JD. A theoretical model for f-actin remodeling in vascular smooth muscle cells subjected to cyclic stretch. J Theor Biol 2007;246:87-99.

[110] Na S, Sun Z, Meininger GA, Humphrey JD. On atomic force microscopy and the constitutive behavior of living cells. Biomech Model Mechanobiol 2004;3:75-84.

[111] Valentin A, Humphrey JD. Modeling effects of axial extension on arterial growth and remodeling. Med Biol Eng Comput 2009;47:979-987.

[112] Sharefkin JB, Diamond SL, Eskin SG, McIntire LV, Dieffenbach CW. Fluid flow decreases preproendothelin mrna levels and suppresses endothelin-1 peptide release in cultured human endothelial cells. J Vasc Surg 1991;14:1-9.

[113] Rodriguez-Vita J, Ruiz-Ortega M, Ruperez M, Esteban V, Sanchez-Lopez E, Plaza JJ, Egido J. Endothelin-1, via eta receptor and independently of transforming growth factor-beta, increases the connective tissue growth factor in vascular smooth muscle cells. Circ Res 2005;97:125-134.

[114] Horstmeyer A, Licht C, Scherr G, Eckes B, Krieg T. Signalling and regulation of collagen i synthesis by et-1 and tgf-beta1. FEBS J 2005;272:6297-6309.

[115] Takuwa Y, Yanagisawa M, Takuwa N, Masaki T. Endothelin, its diverse biological activities and mechanisms of action. Prog Growth Factor Res 1989;1:195-206.

[116] Langille BL. Arterial remodeling: Relation to hemodynamics. Can J Physiol Pharmacol 1996;74:834-841.

[117] Shapiro SD, Endicott SK, Province MA, Pierce JA, Campbell EJ. Marked longevity of human lung parenchymal elastic fibers deduced from prevalence of d-aspartate and nuclear weapons-related radiocarbon. J Clin Invest 1991;87:1828-1834.

[118] Davis EC. Stability of elastin in the developing mouse aorta: A quantitative radioautographic study. Histochemistry 1993;100:17-26.

[119] Stenmark KR, Mecham RP. Cellular and molecular mechanisms of pulmonary vascular remodeling. Annu Rev Physiol 1997;59:89-144.

[120] Jackson ZS. Wall tissue remodeling regulates longitudinal tension in arteries. Circ Res 2002;90:918-925.

[121] Jackson ZS. Partial off-loading of longitudinal tension induces arterial tortuosity. Arterioscler Thromb Vasc Biol 2005;25:957-962.

[122] Ruberti JW, Hallab NJ. Strain-controlled enzymatic cleavage of collagen in loaded matrix. Biochem Biophys Res Commun 2005;336:483-489.

[123] Ruddy JM, Jones JA, Stroud RE, Mukherjee R, Spinale FG, Ikonomidis JS. Differential effect of wall tension on matrix metalloproteinase promoter activation in the thoracic aorta. J Surg Res 2010;160:333-339.

[124] Wolinsky H. Long-term effects of hypertension on the rat aortic wall and their relation to concurrent aging changes. Morphological and chemical studies. Circ Res 1972;30:301-309.

[125] Fridez P, Zulliger M, Bobard F, Montorzi G, Miyazaki H, Hayashi K, Stergiopulos N. Geometrical, functional, and histomorphometric adaptation of rat carotid artery in induced hypertension. J Biomech 2003;36:671-680.

[126] Matsumoto T, Hayashi K. Stress and strain distribution in hypertensive and normotensive rat aorta considering residual strain. J Biomech Eng 1996;118:62-73.

[127] Stacy DL, Prewitt RL. Effects of chronic hypertension and its reversal on arteries and arterioles. Circ Res 1989;65:869-879.

[128] Xu C. Molecular mechanisms of aortic wall remodeling in response to hypertension. J Vasc Surg 2001;33:570-578.

[129] Kockx MM, Knaapen MW. The role of apoptosis in vascular disease. J Pathol 2000;190:267-280.

[130] Olivetti G, Anversa P, Melissari M, Loud AV. Morphometry of medial hypertrophy in the rat thoracic aorta. Lab Invest 1980;42:559-565.

[131] Liu SQ, Fung YC. Relationship between hypertension, hypertrophy, and opening angle of zero-stress state of arteries following aortic constriction. J Biomech Eng 1989;111:325-335.

[132] Hu JJ, Ambrus A, Fossum TW, Miller MW, Humphrey JD, Wilson E. Time courses of growth and remodeling of porcine aortic media during hypertension: A quantitative immunohistochemical examination. J Histochem Cytochem 2008;56:359-370.

[133] Kanzaki T, Tamura K, Takahashi K, Saito Y, Akikusa B, Oohashi H, Kasayuki N, Ueda M, Morisaki N. In vivo effect of tgf- beta 1. Enhanced intimal thickening by administration of tgf- beta 1 in rabbit arteries injured with a balloon catheter. Arterioscler Thromb Vasc Biol 1995;15:1951-1957.

[134] Kubota T, Kubota N, Moroi M, Terauchi Y, Kobayashi T, Kamata K, Suzuki R, Tobe K, Namiki A, Aizawa S, Nagai R, Kadowaki T, Yamaguchi T. Lack of insulin receptor substrate-2 causes progressive neointima formation in response to vessel injury. Circulation 2003;107:3073-3080.

[135] Schulick AH, Taylor AJ, Zuo W, Qiu CB, Dong G, Woodward RN, Agah R, Roberts AB, Virmani R, Dichek DA. Overexpression of transforming growth factor beta1 in arterial endothelium causes hyperplasia, apoptosis, and cartilaginous metaplasia. Proc Natl Acad Sci U S A 1998;95:6983-6988.

[136] Smith JD, Bryant SR, Couper LL, Vary CP, Gotwals PJ, Koteliansky VE, Lindner V. Soluble transforming growth factor-beta type ii receptor inhibits negative remodeling, fibroblast transdifferentiation, and intimal lesion formation but not endothelial growth. Circ Res 1999;84:1212-1222.

[137] Wolf YG, Rasmussen LM, Ruoslahti E. Antibodies against transforming growth factor-beta 1 suppress intimal hyperplasia in a rat model. J Clin Invest 1994;93:1172-1178.

[138] Glasser SP, Arnett DK. Vascular stiffness and the "chicken-or-the-egg" question. Hypertension 2008;51:177-178.

[139] Greenwald SE. Ageing of the conduit arteries. J Pathol 2007;211:157-172.

[140] Narkiewicz K, Kjeldsen SE, Oparil S, Hedner T. Hypertension and cardiovascular disease: Is arterial stiffness the heart of the matter? Blood Press 2007;16:236-237.

[141] O'Rourke MF, Nichols WW. Aortic diameter, aortic stiffness, and wave reflection increase with age and isolated systolic hypertension. Hypertension 2005;45:652-658.

[142] Payne RA, Webb DJ. Arterial blood pressure and stiffness in hypertension: Is arterial structure important? Hypertension 2006;48:366-367.

[143] Garcia M, Kassab GS. Right coronary artery becomes stiffer with increase in elastin and collagen in right ventricular hypertrophy. J Appl Physiol 2009;106:1338-1346.

[144] Humphrey JD, Na S. Elastodynamics and arterial wall stress. Ann Biomed Eng 2002;30:509-523.

[145] Davidson JM, Hill KE, Mason ML, Giro MG. Longitudinal gradients of collagen and elastin gene expression in the porcine aorta. J Biol Chem 1985;260:1901-1908.

[146] Monici M. Cell and tissue autofluorescence research and diagnostic applications. Biotechnol Annu Rev 2005;11:227-256.

[147] Kingsley K, Carroll K, Huff JL, Plopper GE. Photobleaching of arterial autofluorescence for immunofluorescence applications. Biotechniques 2001;30:794-797.

[148] Abcam, 2010, "Ihc paraffin staining protocol," http://www.abcam.com/ps/pdf/protocols/ihc_p.pdf.

[149] Hu Y, Zhang Z, Torsney E, Afzal AR, Davison F, Metzler B, Xu Q. Abundant progenitor cells in the adventitia contribute to atherosclerosis of vein grafts in apoe-deficient mice. J Clin Invest 2004;113:1258-1265.

[150] Passman JN, Dong XR, Wu SP, Maguire CT, Hogan KA, Bautch VL, Majesky MW. A sonic hedgehog signaling domain in the arterial adventitia supports resident sca1+ smooth muscle progenitor cells. Proc Natl Acad Sci U S A 2008;105:9349-9354.

[151] Torsney E, Hu Y, Xu Q. Adventitial progenitor cells contribute to arteriosclerosis. Trends Cardiovasc Med 2005;15:64-68.

[152] Fina L, Molgaard HV, Robertson D, Bradley NJ, Monaghan P, Delia D, Sutherland DR, Baker MA, Greaves MF. Expression of the cd34 gene in vascular endothelial cells. Blood 1990;75:2417-2426.

[153] Jian-Jun L, Ji-Lin C. Inflammation may be a bridge connecting hypertension and atherosclerosis. Med Hypotheses 2005;64:925-929.

[154] Yamamoto K, Ikeda U, Shimada K. Role of mechanical stress in monocytes/macrophages: Implications for atherosclerosis. Curr Vasc Pharmacol 2003;1:315-319.

[155] Carnell PH, Vito RP, Taylor WR. Characterizing intramural stress and inflammation in hypertensive arterial bifurcations. Biomech Model Mechanobiol 2007;6:409-421.

[156] Clozel M, Kuhn H, Hefti F, Baumgartner HR. Endothelial dysfunction and subendothelial monocyte macrophages in hypertension. Effect of angiotensin converting enzyme inhibition. Hypertension 1991;18:132-141.

[157] Hayashida K, Fujita J, Miyake Y, Kawada H, Ando K, Ogawa S, Fukuda K. Bone marrow-derived cells contribute to pulmonary vascular remodeling in hypoxia-induced pulmonary hypertension. Chest 2005;127:1793-1798.

[158] Davie NJ, Crossno JT, Jr., Frid MG, Hofmeister SE, Reeves JT, Hyde DM, Carpenter TC, Brunetti JA, McNiece IK, Stenmark KR. Hypoxia-induced pulmonary artery adventitial remodeling and neovascularization: Contribution of progenitor cells. Am J Physiol Lung Cell Mol Physiol 2004;286:L668-678.

[159] Spees JL, Whitney MJ, Sullivan DE, Lasky JA, Laboy M, Ylostalo J, Prockop DJ. Bone marrow progenitor cells contribute to repair and remodeling of the lung and heart in a rat model of progressive pulmonary hypertension. FASEB J 2008;22:1226-1236.

[160] Bailey AS, Willenbring H, Jiang S, Anderson DA, Schroeder DA, Wong MH, Grompe M, Fleming WH. Myeloid lineage progenitors give rise to vascular endothelium. Proc Natl Acad Sci U S A 2006;103:13156-13161.

[161] Wagers AJ, Weissman IL. Plasticity of adult stem cells. Cell 2004;116:639-648.

[162] Kobayashi N, Yasu T, Ueba H, Sata M, Hashimoto S, Kuroki M, Saito M, Kawakami M. Mechanical stress promotes the expression of smooth muscle-like properties in marrow stromal cells. Exp Hematol 2004;32:1238-1245.

[163] Dickhout JG, Lee RM. Increased medial smooth muscle cell length is responsible for vascular hypertrophy in young hypertensive rats. Am J Physiol Heart Circ Physiol 2000;279:H2085-2094.

[164] Hayashi K, Naiki T. Adaptation and remodeling of vascular wall; biomechanical response to hypertension. J Mech Behav Biomed Mater 2009;2:3-19.

[165] Amann K, Gharehbaghi H, Stephen S, Mall G. Hypertrophy and hyperplasia of smooth muscle cells of small intramyocardial arteries in spontaneously hypertensive rats. Hypertension 1995;25:124-131.

[166] Warshaw DM, Mulvany MJ, Halpern W. Mechanical and morphological properties of arterial resistance vessels in young and old spontaneously hypertensive rats. Circ Res 1979;45:250-259.

[167] Stegemann JP, Nerem RM. Phenotype modulation in vascular tissue engineering using biochemical and mechanical stimulation. Ann Biomed Eng 2003;31:391-402.

[168] Zhang C, Hein TW, Wang W, Miller MW, Fossum TW, McDonald MM, Humphrey JD, Kuo L. Upregulation of vascular arginase in hypertension decreases nitric oxide-mediated dilation of coronary arterioles. Hypertension 2004;44:935-943.

[169] Glagov S, Weisenberg E, Zarins CK, Stankunavicius R, Kolettis GJ. Compensatory enlargement of human atherosclerotic coronary arteries. N Engl J Med 1987;316:1371-1375.

[170] Lee RT, Grodzinsky AJ, Frank EH, Kamm RD, Schoen FJ. Structure-dependent dynamic mechanical behavior of fibrous caps from human atherosclerotic plaques. Circulation 1991;83:1764-1770.

[171] Lessner SM, Martinson DE, Galis ZS. Compensatory vascular remodeling during atherosclerotic lesion growth depends on matrix metalloproteinase-9 activity. Arterioscler Thromb Vasc Biol 2004;24:2123-2129.

[172] Lutgens E, de Muinck ED, Heeneman S, Daemen MJ. Compensatory enlargement and stenosis develop in apoe(-/-) and apoe*3-leiden transgenic mice. Arterioscler Thromb Vasc Biol 2001;21:1359-1365.

[173] Virmani R, Kolodgie FD, Burke AP, Farb A, Schwartz SM. Lessons from sudden coronary death: A comprehensive morphological classification scheme for atherosclerotic lesions. Arterioscler Thromb Vasc Biol 2000;20:1262-1275.

[174] Richardson PD, Davies MJ, Born GV. Influence of plaque configuration and stress distribution on fissuring of coronary atherosclerotic plaques. Lancet 1989;2:941-944.

[175] Huang H, Virmani R, Younis H, Burke AP, Kamm RD, Lee RT. The impact of calcification on the biomechanical stability of atherosclerotic plaques. Circulation 2001;103:1051-1056.

[176] Vengrenyuk Y, Carlier S, Xanthos S, Cardoso L, Ganatos P, Virmani R, Einav S, Gilchrist L, Weinbaum S. A hypothesis for vulnerable plaque rupture due to stress-induced debonding around cellular microcalcifications in thin fibrous caps. Proc Natl Acad Sci U S A 2006;103:14678-14683.

[177] Salunke NV, Topoleski LD. Biomechanics of atherosclerotic plaque. Crit Rev Biomed Eng 1997;25:243-285.

[178] Stary HC, Chandler AB, Dinsmore RE, Fuster V, Glagov S, Insull W, Jr., Rosenfeld ME, Schwartz CJ, Wagner WD, Wissler RW. A definition of advanced types of atherosclerotic lesions and a histological classification of atherosclerosis. A report from the committee on vascular lesions of the council on arteriosclerosis, american heart association. Circulation 1995;92:1355-1374.

[179] Plasschaert H, Heeneman S, Daemen MJ. Progression in atherosclerosis: Histological features and pathophysiology of atherosclerotic lesions. Top Magn Reson Imaging 2009;20:227-237.

[180] Stary HC. Atlas of atherosclerosis - progression and regression. New York: Pantheon Publishing, 1999.

[181] Groen HC, van Walsum T, Rozie S, Klein S, van Gaalen K, Gijsen FJ, Wielopolski PA, van Beusekom HM, de Crom R, Verhagen HJ, van der Steen AF, van der Lugt A, Wentzel JJ, Niessen WJ. Three-dimensional registration of histology of human atherosclerotic carotid plaques to in-vivo imaging. J Biomech43:2087-2092.

[182] Riou LM, Broisat A, Dimastromatteo J, Pons G, Fagret D, Ghezzi C. Pre-clinical and clinical evaluation of nuclear tracers for the molecular imaging of vulnerable atherosclerosis: An overview. Curr Med Chem 2009;16:1499-1511.

[183] Schaar JA, De Korte CL, Mastik F, Strijder C, Pasterkamp G, Boersma E, Serruys PW, Van Der Steen AF. Characterizing vulnerable plaque features with intravascular elastography. Circulation 2003;108:2636-2641.

[184] Le Floc'h S, Ohayon J, Tracqui P, Finet G, Gharib AM, Maurice RL, Cloutier G, Pettigrew RI. Vulnerable atherosclerotic plaque elasticity reconstruction based on a segmentation-driven optimization procedure using strain measurements: Theoretical framework. IEEE Trans Med Imaging 2009;28:1126-1137.

[185] Ali ZA, Alp NJ, Lupton H, Arnold N, Bannister T, Hu Y, Mussa S, Wheatcroft M, Greaves DR, Gunn J, Channon KM. Increased in-stent stenosis in apoe knockout mice: Insights from a novel mouse model of balloon angioplasty and stenting. Arterioscler Thromb Vasc Biol 2007;27:833-840.

[186] Vengrenyuk Y, Kaplan TJ, Cardoso L, Randolph GJ, Weinbaum S. Computational stress analysis of atherosclerotic plaques in apoe knockout mice. Ann Biomed Eng 2010;38:738-747.

[187] Johnson K. Contact mechanics. Cambridge: Cambridge University Press, 1985.

[188] Costa KD, Sim AJ, Yin FCP. Non-hertzian approach to analyzing mechanical properties of endothelial cells probed by atomic force microscopy. J Biomech Eng 2006;128:176.

[189] Loree HM, Grodzinsky AJ, Park SY, Gibson LJ, Lee RT. Static circumferential tangential modulus of human atherosclerotic tissue. J Biomech 1994;27:195-204.

[190] Topoleski LD, Salunke NV. Mechanical behavior of calcified plaques: A summary of compression and stress-relaxation experiments. Z Kardiol 2000;89 Suppl 2:85-91.

[191] Finet G, Ohayon J, Rioufol G, Lefloch S, Tracqui P, Dubreuil O, Tabib A. Morphological and biomechanical aspects of vulnerable coronary plaque. Arch Mal Coeur Vaiss 2007;100:547-553.

[192] Discher DE, Janmey P, Wang YL. Tissue cells feel and respond to the stiffness of their substrate. Science 2005;310:1139-1143.

[193] Janmey PA, McCulloch CA. Cell mechanics: Integrating cell responses to mechanical stimuli. Ann Rev Biomed Eng 2007;9:1-34.

[194] Nemir S, Hayenga HN, West JL. Pegda hydrogels with patterned elasticity: Novel tools for the study of cell response to substrate rigidity. Biotechnol Bioeng 2010;105:636-644.

[195] Solon J, Levental I, Sengupta K, Georges P, Janmey P. Fibroblast adaptation and stiffness matching to soft elastic substrates. Biophys J 2007;93:4453-4461.

[196] Engler A, Sen S, Sweeney H, Discher D. Matrix elasticity directs stem cell lineage specification. Cell 2006;126:677-689.

[197] Matsumoto T. Residual stress and strain in the lamellar unit of the porcine aorta: Experiment and analysis. J Biomech 2004;37:807-815.

[198] Oie T, Murayama Y, Fukuda T, Nagai C, Omata S, Kanda K, Yaku H, Nakayama Y. Local elasticity imaging of vascular tissues using a tactile mapping system. J Artif Organs 2009;12:40-46.

[199] Gosline J, Lillie M, Carrington E, Guerette P, Ortlepp C, Savage K. Elastic proteins: Biological roles and mechanical properties. Philos Trans R Soc Lond B Biol Sci 2002;357:121-132.

[200] Greenwald SE, Moore JE, Jr., Rachev A, Kane TP, Meister JJ. Experimental investigation of the distribution of residual strains in the artery wall. J Biomech Eng 1997;119:438-444.

[201] Geiger B, Spatz JP, Bershadsky AD. Environmental sensing through focal adhesions. Nat Rev Mol Cell Biol 2009;10:21-33.

[202] Walcott S, Sun SX. A mechanical model of actin stress fiber formation and substrate elasticity sensing in adherent cells. Proc Natl Acad Sci U S A 2010;107:7757-7762.

[203] Clarke MCH, Littlewood TD, Figg N, Maguire JJ, Davenport AP, Goddard M, Bennett MR. Chronic apoptosis of vascular smooth muscle cells accelerates

atherosclerosis and promotes calcification and medial degeneration. Circ Res 2008;102:1529-1538.

[204] Atkinson J. Age-related medial elastocalcinosis in arteries: Mechanisms, animal models, and physiological consequences. J Appl Physiol 2008;105:1643-1651.

[205] Price PA, Faus SA, Williamson MK. Warfarin causes rapid calcification of the elastic lamellae in rat arteries and heart valves. Arterioscler Thromb Vasc Biol 1998;18:1400-1407.

VITA

Name:	Heather Naomi Hayenga
Address:	c/o Biomedical Engineering Department, Texas A&M University, College Station, TX 77843-3120
Email Address:	hnhayenga@gmail.com
Education:	B.S., Biomedical Engineering, University of California, Davis, June 2006
	Ph.D., Biomedical Engineering, Texas A&M University, May 2011